UC San Diego

UC San Diego Electronic Theses and Dissertations

Title

Multiscale circuit analysis of visual information processing

Permalink

https://escholarship.org/uc/item/58x67629

Author

Marshel, James Henry

Publication Date

2011

Supplemental Material

https://escholarship.org/uc/item/58x67629#supplemental

Peer reviewed|Thesis/dissertation

eScholarship.org Powered by the California Digital Library
University of California

UNIVERSITY OF CALIFORNIA, SAN DIEGO

Multiscale circuit analysis of visual information processing

A dissertation submitted in partial satisfaction of the

requirements for the degree of Doctor of Philosophy

in

Neurosciences

by

James Henry Marshel, IV

Committee in Charge:

Professor Edward Callaway, Chair
Professor Jeffry Isaacson, Co-Chair
Professor Mark Ellisman
Professor Massimo Scanziani
Professor Terrence Sejnowski

2011

©

James Henry Marshel, IV 2011

All rights reserved.

The Dissertation of James Henry Marshel, IV is approved, and it is acceptable in quality and form for publication on microfilm:

Co-Chair

Chair

University of California, San Diego

2011

DEDICATION

I dedicate this dissertation to my parents.
You have taught me how to overcome any obstacle in life,
and to value education above all else.
I would not be where I am today without your support.

TABLE OF CONTENTS

LIST OF FIGURES

ACKNOWLEDGMENTS

I would like to thank the members of my dissertation committee: Jeff Isaacson, Mark Ellisman, Massimo Scanziani, and Terry Sejnowski. Their guidance has been invaluable.

I would also like to thank the members of the Callaway lab for their friendship and collaboration. I especially would like to thank Marina Garrett and Alfred Kaye for being excellent collaborative partners.

Finally, I would like to thank my advisor, Ed Callaway, for his daring approach to neuroscience, and his thoughtful, patient guidance. I thank him for his optimism, clear foresight, and for having faith in me.

Chapter 2, in full, has been submitted for publication of the material as it may appear in publication, Marshel, James H.; Kaye, Alfred P.; Nauhaus, Ian; Callaway, Edward M.. The dissertation author was co-primary investigator and author of this paper.

Chapter 3, in full, is a reprint of the material as it appears in Neuron, 2010, Marshel, James H.; Mori, Takuma; Nielsen, Kristina; Callaway, Edward M., Cell Press, 2010. The dissertation author is the primary investigator and author of this material.

Chapter 4, in full, is being prepared for submission for publication of the material. Marshel, J.H., Garrett, M.E., Nauhaus, I., & Callaway, E.M. (In Preparation). Retinotopic and receptive field characterization of mouse striate and extrastriate visual

cortex. The dissertation author was the co-primary investigator and co-author of this paper.

The Appendix, in part, is a reprint of the material as it appears in Neuron, 2011, Osakada, Fumitaka; Mori, Takuma; Cetin, Ali H.; Marshel, James H.; Virgen, Beatriz; Callaway, Edward M., Cell Press, 2011 (in press). The dissertation author is the co-investigator and co-author of this material.

VITA

2001-2005 University of California, Berkeley
B.A. in Molecular and Cell Biology
B.A. in Psychology

2005-2011 University of California, San Diego
Ph.D. in Neurosciences

PUBLICATIONS

Marshel JH*, Garrett ME*, Nauhaus I, Callaway EM. Retinotopic and receptive field characterization of mouse striate and extrastriate cortex. (*In preparation*)

Marshel JH*, Kaye AP*, Nauhaus I, Callaway EM. Functional organization of direction selectivity in the mouse lateral geniculate nucleus. (*Submitted*).

Osakada, F, Mori, T, Cetin, AH, Marshel, JH, Virgen, B, Callaway, EM. (2011). New rabies variants for monitoring and manipulating activity and gene expression in defined neural circuits. Neuron (*in press*).

Marshel JH, Mori T, Nielsen KJ, Callaway EM (2010). Targeting single neuronal networks for gene expression and cell labeling *in vivo.* Neuron *67*, 562-574.

CONFERENCE ABSTRACTS

Marshel JH, Mori T, Nielsen K, Callaway EM. Mapping the monosynaptic inputs to a single visual cortical neuron *in vivo*. Talk presented at: Society for Neuroscience Annual Meeting. 2010 Nov 13-17; San Diego, CA.

Kaye AP*, Marshel JH*, Nauhaus I, Callaway EM. Functional organization of the mouse LGN examined with *in vivo* two-photon calcium imaging. Presented at: Society for Neuroscience Annual Meeting. 2010 Nov 13-17; San Diego, CA.

Garrett ME*, Marshel JH*, Nauhaus I, Callaway EM. Functional characterization of neuronal populations in striate and extrastriate regions of the mouse visual cortex. Presented at: Society for Neuroscience Annual Meeting. 2010 Nov 13-17; San Diego, CA.

Marshel JH. Relating specific neuronal network structure and function to perceptual experience *in vivo*. Invited talk presented at: The Cognitive Neuroscience and Kavli Institute for Brain and Mind Annual Symposium. 2010 May 1; San Diego, CA.

Marshel JH, Callaway EM. Targeting single neuronal networks for functional analysis *in vivo*. Presented at: Neuronal Circuits. 2010 Mar 10-13; Cold Spring Harbor, NY.

Marshel JH. Linking connectivity to function of neurons in visual cortex. Invited talk presented at the Cognitive Neuroscience and Kavli Institute for Brain and Mind Annual Symposium. 2009 May 2; San Diego, CA.

Marshel JH, Mori T, Nielsen KJ, Callaway EM. Targeting single neuronal networks for gene expression and cell labeling *in vivo*. Presented at: Society for Neuroscience Annual Meeting. 2008 Nov 15-20; Washington, D.C.

Marshel JH, Mori T, Nielsen KJ, Callaway EM. Targeting single neuronal networks for gene expression and cell labeling *in vivo*. Presented at: Computation in Cortical Circuits. 2008 Sept 20-25; Ascona, Switzerland.

Marshel JH. Targeting single neuronal networks *in vivo*. Invited talk presented at the Cognitive Neuroscience and Kavli Institute for Brain and Mind Annual Symposium. 2008 May 3; San Diego, CA.

Marshel JH, Mori T, Nielsen KJ, Callaway EM. Targeting single neuronal networks for gene expression and cell labeling. Presented at: Neuronal Circuits: From Structure to Function. 2008 Mar 13-16; Cold Spring Harbor, NY.

Marshel, J.H., Brooks, J.L., Hillyard, S.A., & Robertson, L.C. (2005). Attention, not objects reflected in posterior gamma band activity. Presented at: Society for Neuroscience Annual Meeting; 2005 Nov, Washington, D.C.

Brooks, J.L., Marshel, J.H., List, A., Knight, R.T., & Robertson, L.C. (2004). Gamma band activity related to spatial attention in visual search. Presented at: Society for Neuroscience Annual Meeting. 2004 Nov 2004; San Diego, CA.

*Equal contributions

ABSTRACT OF THE DISSERTATION

Multiscale circuit analysis of visual information processing

by

James Henry Marshel, IV

Doctor of Philosophy in Neurosciences

University of California, San Diego, 2011

Professor Edward Callaway, Chair
Professor Jeffry Isaacson, Co-Chair

The brain organizes information across multiple scales, from molecules to circuits to systems. Information is processed in stages, becoming increasingly refined and specialized at each level. We developed technologies to analyze information processing across multiple scales simultaneously. We answer several previously inaccessible questions about the structure and function of the mouse visual system (**summarized in Chapter 1**).

Direction of motion is first encoded by retinal ganglion cells (RGCs). We developed a method to image the responses of anatomically-identified neurons in the LGN. We found that LGN organizes direction information in a laminar pattern partially predicted by RGC inputs; only posterior and anterior directions are encoded

in the superficial layer. This information is refined; direction-selective LGN neurons are more sharply tuned than RGCs. The superficial LGN integrates direction information, forming axis-of-motion selectivity for anterior-posterior motion (**Chapter 2**).

Understanding information integration by microcircuits requires novel technologies to study the structure and function of microcircuits in the intact brain. In **Chapter 3**, we developed a technology to target monosynaptic inputs to a single visual cortical neuron for gene manipulation and fine-scale cell labeling *in vivo*. We labeled inputs across the intact brain.

Single circuits in V1 and higher visual areas process signals from the LGN and other areas to compute increasingly specialized visual information. We developed methods to define visual cortical areas across the entire visual cortex down to single cell resolution in the same animal, within the same day (**Chapter 4**). We compared the response properties of populations of neurons from 7 visual areas. Extrastriate cortex processes motion information up to 3 times the temporal frequency than V1. A subset of areas maintains high spatial frequency tuning of V1, while another group prefers approximately half the spatial frequency. Extrastriate visual areas are more orientation selective and some are more direction selective.

We apply a novel rabies virus to measure the fine-scale structure and function of neurons in V1 providing monosynaptic input to an extrastriate visual area (**Appendix**). This technology may help integrate across the scales investigated in each chapter to understand how information is transformed at each processing stage by specialized microcircuits.

CHAPTER I

INTRODUCTION

The brain organizes information across several scales (Churchland and Sejnowski, 1988). At the molecular level, information is stored via protein-protein and protein-chemical interactions, and gene regulation. These mechanisms shape the identity of brain cells, and alter the response properties of neurons. Each neuron maintains up to thousands of input synapses, and integrates combinations of activity from these inputs in time, transforming incoming information using mechanisms dependent upon its current molecular makeup, and anatomical features such as its unique morphology and the precise locations of each input synapse. Through this process, each neuron generates its own information code—its characteristic temporal pattern of action potentials. It sends this information to up to thousands of other neurons, which in turn process this input through the same mechanisms. Amazingly, these networks lead to neurons which respond to specific types of information, whether it be a sensory feature detected in the world, or an abstract executive function. Neurons encoding similar types of information often organize together in space within the brain, forming distinct brain areas comprised of millions of neurons. In several cases, information is further organized within these areas in terms of laminar organization and orderly maps of information, often relating to the physical organization of this information in the world. These brain areas make selective and dense connections with other brain areas, with a flow of information often occurring in both directions, and with encoded information becoming increasingly complex as connections between areas build upon each other and information processed in parallel is integrated (Nassi and Callaway, 2009). These interactions form a complete brain system specialized to process certain information about the outside world, or the

internal state of the organism. Finally, these systems interact with one another to coordinate bodily functions, generate behavior and form a complete, coherent sensory, perceptual and cognitive experience.

Given this multiscale organization of the brain, our analyses of its functional organization should similarly be multiscale. Certainly, the wealth of information that humans have gathered to date has resulted from studying the brain at each of these many levels. But, the sheer size of the brain combined with the absence of techniques which appreciate each of these levels simultaneously, especially at the level of understanding how neuronal network connectivity relates to neuronal functional properties, has obstructed an integrative, mechanistic understanding of brain function.

Ideally, we could relate real time gene expression and molecular interactions with ongoing neuronal activity measured within populations of single neurons in identified neuronal networks, recorded simultaneously across local and large scale neuronal networks, across brain regions and brain systems, in relation to ongoing sensory information, internal brain state and behavior. This approach may yield greater amounts of information more efficiently, and help reveal complex interactions across scales otherwise missed by analyzing each brain level in isolation.

As farfetched as this experimental strategy may sound, it is closer to reality than ever before, and is effectively in progress in the analysis of invertebrate systems (Luo et al., 2008). Applying this strategy in the mammalian brain faces several challenges. Namely, the number of neurons to investigate is prohibitive, and the area to cover is too large, especially in large mammals such as primates. Furthermore, neuronal circuits are sufficiently complex and intertangled that determining

connectivity between single neurons is virtually impossible in the intact brain beyond painstakingly probing pairs of closely neighboring neurons. Furthermore, measuring this information at single cell resolution across multiple brain areas simultaneously is not possible with current electrophysiological techniques.

The goal of this dissertation is to move us closer to realizing this goal of multiscale circuit analysis for the mammalian brain. As such, several technologies are developed here, and in their application several previously inaccessible scientific questions are answered. All work described here was performed in the mouse model system, and all technologies and scientific questions are developed and aimed within the visual system.

The mouse system was chosen for several reasons. It is currently the most experimentally accessible mammalian system. Its genetic tractability is sophisticated and expanding rapidly, making it possible to study brain processes at the molecular level, including genetically targeting specific neuronal cell types, and manipulating and probing gene expression in time (Luo et al., 2008). Imaging technologies have also been best developed in this mammalian system permitting high resolution *in vivo* imaging of the functional properties of anatomically identified populations of neurons (Kerlin et al., 2010; Briggman et al., 2011). The relatively small size of the mouse puts multiscale analysis closer within reach since high resolution imaging techniques are limited by the amount of space they can cover at one time. Finally, for these reasons, and the fact that the mouse is the most readily available model mammalian system, high-throughput studies are possible in the mouse, making it possible to quickly

develop novel technologies and to generate large amounts of data across several animals.

The visual system was chosen for several reasons as well. Studying information processing is arguably most powerful when it is possible to systematically manipulate the information processed by the system. Hence, studying sensory information processing is most straightforward given the ability to carefully control for the information input to the system. This is especially true of vision, in which light input to the system can be carefully manipulated along continuous, quantifiable and controllable dimensions. Sensory systems also offer the advantage that it is possible to define an order to processing levels within the brain, at least at lower levels of processing, beginning with sensory receptors, almost always passing through thalamic structures and processed further by specialized cortical brain areas. At all of these levels, local processing by local neuronal circuitry as well as interactions between brain areas and processing levels can be studied, permitting multilevel circuit analysis of information processing. More is known about the visual system than any other sensory system, and it exhibits all of the multiscale features described above, and thus may serve as a model for multiscale information in other systems.

In vision, light is detected by photoreceptors; basic statistics of an image are extracted by local circuitry and encoded in the action potentials of retinal ganglion cells. Several types of retinal ganglion cells (RGCs) exist; each specialized to encode specific types of information about an image. This information is projected in parallel to the brain via ganglion cell axons targeting several subcortical structures serving reflexive behaviors, as well as the lateral geniculate nucleus (LGN). These axons

target specific layers within the LGN, and the LGN thus maintains segregation of information channels in space. Little is known about how local circuitry manipulates information within the LGN. Furthermore, the LGN maintains a map of visual space organized in terms of its retinal inputs (retinotopy). The main projection of the LGN is to primary visual cortex (V1), where information again is targeted to specific layers. Here, more complex information is encoded about the structure of local regions within an image, for example how edges of light are arranged in space (Hubel and Wiesel, 1962). V1 again maintains the retinotopic map. V1 projects to several other visual cortical areas, which each contain near complete and orderly representations of retinotopic visual space. Receptive field sizes increase as this information is passed through the hierarchy of connections between visual areas. Several of these extrastriate visual areas are known to process unique types of complex information, including motion and specific object recognition relying on high-order feature integration (Nassi and Callaway, 2009). Also, areas higher in the visocortical hierarchy are more likely to combine information across brain modalities (including other senses), and top-down attentional effects are more pronounced in some of these areas. Along the full hierarchy, selective connections propagate information up in the hierarchy, and feedback connections from higher areas modulate information processing in lower areas. This structure results in an extraordinarily complex system; one theoretically optimized to efficiently handle ecologically relevant visual information, and designed to dynamically shift computational resources to processing specific types of information depending on behavioral demand in time.

Dissertation Summary

This dissertation describes three studies, each comprising its own chapter, which together bridge across almost all but the highest levels of brain organization described above. An appendix section shows a proof-of-principle experiment demonstrating the ability to directly bridge across the levels studied in isolation in each independent study. The chapters are organized in order of level within the visual system hierarchy.

Chapter 2 describes a study of the motion-related response properties of neurons within the dorsal lateral geniculate nucleus (dLGN) as they relate to retinal ganglion cell inputs. It develops and applies a novel technique to measure the response properties of anatomically identified neurons within the dLGN *in vivo*: two-photon calcium imaging of the thalamus. It tests predictions based on known RGC projections to layers within the dLGN (Huberman et al., 2009; Kim et al., 2010). This study finds that the superficial layer of the dLGN contains a small population of direction-selective neurons that encode posterior motion, agreeing with projections of posterior direction-selective retinal ganglion cells (pDSRGCs) to the superficial dLGN. Surprisingly, this study also finds that the superficial dLGN also contains neurons which encode anterior direction of motion, and contains neurons encoding motion along both directions of the anterior-posterior axis. This result was not predicted previously. Neurons encoding the orthogonal axis of motion were rare or non-existent in this layer. These results, together with anatomical data, suggest that the dLGN of the mouse contains a laminar organization of direction selectivity. Furthermore, it suggests that direction information is integrated within these layers to form neuron

receptive fields which integrate across directions to form axis selectivity. We also found evidence for sharpening of direction tuning between the retina and thalamus. These results suggest two roles of local dLGN and retinogeniculate circuitry: integration of RGC response types and local sharpening of tuning. This is contrary to the notion that the dLGN merely relays sensory information downstream, and instead implies that the dLGN manipulates information. Furthermore, controversy exists over the extent to which visual cortex computes direction of motion information *de novo*. Given that the dLGN is the primary input to V1, it is highly likely that V1 receives the motion information encoded within the dLGN. How V1 uses this information and the extent to which it builds upon these computations is not known.

Chapter 3 describes a study which develops and applies a novel technique to genetically target and label the monosynaptic inputs to a single visual cortical neuron *in vivo,* targeting a single neuronal network for gene expression in the intact brain. A single neuron is labeled with one colored fluorescent marker and its monosynaptic inputs are labeled with another. Input neurons to single V1 neurons were found locally within V1, as well as in secondary visual areas, the dLGN, and distant cortical and subcortical structures. All neurons were labeled in great detail, revealing their full morphologies. The method used to label connections between neurons—a modified rabies virus (Wickersham et al., 2007)—targets infected neurons for expression of the genes within the virus genome. The genome of the virus is modifiable, and recent studies have modified the virus to carry genes to manipulate gene expression in time and manipulate and probe neuronal activity in vivo. The **appendix** shows the application of one of these modified rabies viruses used to measure the response

properties of neurons which supply input to a known visual area. The ability to interchange the virus used in the single cell tracing strategy described in **Chapter 3** may make it possible to manipulate gene expression and probe and manipulate neuronal activity in identified neuronal networks *in vivo*.

Little is known about the function of extrastriate cortex of the mouse. A recent study predicted that up to 10 visual areas exist in the mouse, including V1 (Wang and Burkhalter, 2007). In **Chapter 4**, we develop and apply a strategy for mapping the nearly complete retinotopic structure of mouse visual cortex, and targeting the majority of mouse visual areas for population analysis of neuronal response properties. We develop a method for stimulating the entire visual hemifield of the mouse while simultaneously imaging the activity of the brain. In stage one of the experiment, we use intrinsic imaging to map the retinotopic structure of visual cortex (Kalatsky and Stryker, 2003). Using this map, we target each retinotopically identified visual area for calcium dye loading (Ohki et al., 2005; Stosiek et al., 2003). Then, under two-photon microscopy, we measure the activity of populations of anatomically identified neurons in layer 2/3 of each of 7 visual areas including V1, LM, LI, AL, RL, AM and PM. We find that extrastriate areas can be distinguished from V1 depending on their tuning properties for temporal frequency, spatial frequency, orientation selectivity and direction selectivity. Furthermore, we find differences between extrastriate areas. These results demonstrate that the mouse visual system organizes information in specialized cortical visual areas.

In the **Appendix**, we apply a novel rabies virus encoding a genetic calcium indicator (GCaMP3; Tian et al., 2009) and a fluorescent marker to measure the fine-

scale structure and function of neurons in V1 providing monosynaptic input to an extrastriate visual area (area AL). We find that inputs to area AL are highly tuned for direction and orientation. We were able to image the neurons up to over 1 mm below the pial surface, well into the deep layers of cortex. We measured the activity of neurons and dendrites at up to over 500 μm deep, suggesting that we were imaging the activity of neurons in deep layer 4 and potentially in layer 5. The anatomical structure revealed by the viral labeling provides additional information about the type of neurons encoding specific information, including laminar and areal location, as well as cell type information. This technology may help integrate across the scales investigated in each chapter to understand how information is transformed at each processing stage by specialized microcircuits. In the case of cortical areas, this method can be used to reveal the types of information sent between areas. Applied to single cell tracing, this virus could help determine the types of information a single neuron integrates. The imaging technology developed to study the LGN could be combined with GCaMP3-rabies tracing to explore whether direction of motion information is relayed to visual cortex and how that information is integrated by cortical circuits. Finally, the virus could be injected in LGN to study the information encoded in the retina which provides input to known LGN populations.

The studies described in this dissertation have the common goal of understanding how neuronal networks give rise to brain function. Each chapter provides insight into how this occurs at a different level within the visual system and develops and applies novel, broadly applicable methods for probing circuit function. The appendix is intended to show how these approaches come together, and provides a

glimpse of what is to come. To understand information processing by the brain, we must integrate across scales to grasp how specific genes, individual neurons, single circuits, and large scale neuronal networks work together to encode and process information. Hopefully, the technologies and insights developed here will help move this process forward if only one small step, and inspire the next set of experiments to bring us closer to these far reaching goals.

References

Briggman, K. L., Helmstaedter, M., and Denk, W. (2011). Wiring specificity in the direction-selectivity circuit of the retina. Nature *471*, 183-188.

Churchland, P. S., and Sejnowski, T. J. (1988). Perspectives on cognitive neuroscience. Science *242*, 741-745.

Hubel, D. H., and Wiesel, T. N. (1962). Receptive fields, binocular interaction and functional architecture in the cat's visual cortex. J. Physiol. (Lond.) *160*, 106-154.

Huberman, A. D., Wei, W., Elstrott, J., Stafford, B. K., Feller, M. B., and Barres, B. A. (2009). Genetic Identification of an On-Off Direction- Selective Retinal Ganglion Cell Subtype Reveals a Layer-Specific Subcortical Map of Posterior Motion. Neuron *62*, 327-334.

Kalatsky, V. A., and Stryker, M. P. (2003). New paradigm for optical imaging: temporally encoded maps of intrinsic signal. Neuron *38*, 529-545.

Kerlin, A. M., Andermann, M. L., Berezovskii, V. K., and Reid, R. C. (2010). Broadly tuned response properties of diverse inhibitory neuron subtypes in mouse visual cortex. Neuron *67*, 858-871.

Kim, I.-J., Zhang, Y., Meister, M., and Sanes, J. R. (2010). Laminar restriction of retinal ganglion cell dendrites and axons: subtype-specific developmental patterns revealed with transgenic markers. J. Neurosci *30*, 1452-1462.

Luo, L., Callaway, E. M., and Svoboda, K. (2008). Genetic dissection of neural circuits. Neuron *57*, 634-660.

Nassi, J. J., and Callaway, E. M. (2009). Parallel processing strategies of the primate visual system. Nat. Rev. Neurosci *10*, 360-372.

Ohki, K., Chung, S., Ch'ng, Y. H., Kara, P., and Reid, R. C. (2005). Functional imaging with cellular resolution reveals precise micro-architecture in visual cortex. Nature *433*, 597-603.

Stosiek, C., Garaschuk, O., Holthoff, K., and Konnerth, A. (2003). In vivo two-photon calcium imaging of neuronal networks. Proc. Natl. Acad. Sci. U.S.A *100*, 7319-7324.

Tian, L., Hires, S. A., Mao, T., Huber, D., Chiappe, M. E., Chalasani, S. H., Petreanu, L., Akerboom, J., McKinney, S. A., Schreiter, E. R., et al. (2009). Imaging

neural activity in worms, flies and mice with improved GCaMP calcium indicators. Nat. Methods *6*, 875-881.

Wang, Q., and Burkhalter, A. (2007). Area map of mouse visual cortex. J. Comp. Neurol *502*, 339-357.

Wickersham, I. R., Lyon, D. C., Barnard, R. J. O., Mori, T., Finke, S., Conzelmann, K.-K., Young, J. A. T., and Callaway, E. M. (2007). Monosynaptic restriction of transsynaptic tracing from single, genetically targeted neurons. Neuron *53*, 639-647.

CHAPTER II

FUNCTIONAL ORGANIZATION OF DIRECTION SELECTIVITY IN THE MOUSE LATERAL GENICULATE NUCLEUS

Summary

Visual motion is computed in the primary visual cortex and also by a separate pathway in the retina of many species. Retinal ganglion cells (RGCs) that respond selectively to a single direction of a moving stimulus were recently shown to project to the dorsal lateral geniculate nucleus (dLGN; Oyster and Barlow, 1967; Huberman et al., 2009; Kim et al., 2008, 2010; Yonehara et al., 2009), which provides the driving input to primary visual cortex, suggesting a potential link between these two pathways. Recently, circuit mechanisms in the retina to compute and encode direction information in RGCs have been revealed (Briggman et al., 2011; Wei et al., 2010; Euler et al., 2002; Fried et al., 2002; Yonehara et al., 2011). However, little is known about how this information is organized and manipulated at subsequent processing stages in the thalamus and cortex, despite the potential relevance of this pathway in perceptual experience and complex behaviors. Here, we developed and applied a novel method for *in vivo* two-photon calcium imaging in the dLGN, yielding the first characterization of neuronal response properties of anatomically identified populations of thalamic neurons. We report that in mice, selectivity for visual motion in the superficial layer of the dLGN is strongly biased for the horizontal axis in the visual field, such that cells are selective for anterior motion direction, posterior motion direction, or both (anterior-posterior axis selective). Neurons selective for the orthogonal axis of motion were extremely rare in this layer. These results confirm a functional laminar organization of mouse dLGN, in contrast to the previously held notion that the mouse dLGN does not contain cell-type specific lamination (Jaubert-

Miazza et al., 2005). The results also corroborate recently discovered projection patterns of direction-selective retinal ganglion cells (DSRGCs) to specific dLGN layers (Huberman et al., 2009; Kim et al., 2010; Kay et al., 2011), and make distinct predictions about unknown DSRGC projections. Moreover, the laminar arrangement of direction-selective opponency and axis selectivity observed here is unprecedented, and may confer computational advantages for higher-order motion processing within the dLGN and in the projection to visual cortex.

Introduction

To guide behavior in a dynamic environment, the visual system must detect and process motion in the world. A fundamental component of this computation is to determine the direction of movement in each region of visual space. This information is first computed in the retina and encoded in the firing rate of DSRGCs (Briggman et al., 2011; Wei et al., 2010; Euler et al., 2002; Fried et al., 2002), which respond vigorously to a light stimulus moving in a specific direction and are inhibited by stimuli moving in the opposite (null) direction (Oyster and Barlow, 1967; Huberman et al., 2009; Kim et al., 2008, 2010; Yonehara et al., 2009; Briggman et al., 2011; Wei et al., 2010; Euler et al., 2002; Fried et al., 2002; Weng et al., 2005; Elstrott et al., 2008). In the case of On-Off DSRGCs, which respond to both light-dark and dark-light transitions, there are four known functional subtypes of cells, each corresponding to motion in one of four cardinal directions (anterior, posterior, upward or downward) (Oyster and Barlow, 1967). It has long been assumed that these neurons exist to aid

reflexive visual behaviors, mediated by purely subcortical pathways (Oyster and Barlow, 1967). However, the direction information encoded in these neurons may serve other systems related to motion perception and complex behavior, although the pathway by which that information passes through the dLGN to cortex is not known.

It is widely believed that direction information arises in visual cortex, independently of thalamic direction-selective inputs (Peterson et al., 2004; Hubel and Wiesel, 1961). However, recent studies in the mouse found that at least three DSRGC functional subtypes project axons to the dLGN. Furthermore, these axons appear to arborize in distinct layers within the dLGN: posterior DSRGCs project to superficial dLGN and downward and upward DSRGCs project to deeper dLGN (Huberman et al., 2009; Kim et al., 2010; Kay et al., 2011). Surprisingly, direction-selective neurons have not been observed in the mouse dLGN (Grubb and Thompson, 2003), unlike other species (Levick et al., 1969; Sumitomo and Iwama, 1977; Montero and Brugge, 1969). Thus, it remains unclear whether the dLGN directly inherits direction tuning projected from the retina, and if DSRGC afferents form layer-specific connections with dLGN neurons leading to laminar organization of preferred direction tuning among dLGN neurons. Currently available electrophysiological methods may not be able to detect rare neuron types in anatomically localized regions of dLGN, raising the possibility that laminar organization of direction-selective neurons may have been missed by previous studies in other species, and that direction-selective neurons may have been missed altogether in the mouse dLGN.

In order to test whether the dLGN maintains direction selectivity from the retina, following the laminar pattern of direction preference predicted from

retinogeniculate circuitry, we developed a method for *in vivo* two-photon calcium imaging of neuronal visual responses in the superficial layer (≤ 75 μm deep from the surface) of mouse dLGN. We also asked how local dLGN circuitry and laminar organization might transform or integrate this direction information before relaying it to visual cortex.

Results and Discussion

To our knowledge, these studies yield the first simultaneous physiological measurements of populations of anatomically identified thalamic neurons (Fig. 2.1). For calcium dye loading, Oregon Green Bapta-1 AM was injected into the dLGN of C57/Bl6 mice (Fig. 2.1a). To test for direction selectivity in the dLGN, we presented drifting square-wave gratings of 12 equally-spaced directions at a speed and spatial frequency known to stimulate DSRGCs (Huberman et al., 2009; Kim et al., 2010, 2008; Wei et al., 2010; Weng et al., 2005; Yonehara et al., 2009; i.e., 25 deg/s, 0.01 cpd). Five repeats of each stimulus and one blank stimulus were presented in random order to the animal while visually-evoked calcium responses were recorded in up to dozens of neurons simultaneously at a known depth in the dLGN, reflecting the underlying changes in firing rate of each neuron (Kerlin et al., 2010; Kerr et al., 2005; Fig. 2.1c-e and 1.2). This method allows even rare neuron subtypes to be detected, and each neuron's precise location to be mapped anatomically within the dLGN. We compared response characteristics and anatomical locations of neurons in the dLGN with RGC properties and projection patterns to confirm and make new predictions about specific retinogeniculate wiring. In the superficial dLGN, we expected to find a

small population of neurons selective for posterior motion, given that posterior DSRGCs sparsely tile the retina and are the only known DSRGC subtype to project axons to that layer (Huberman et al., 2009).

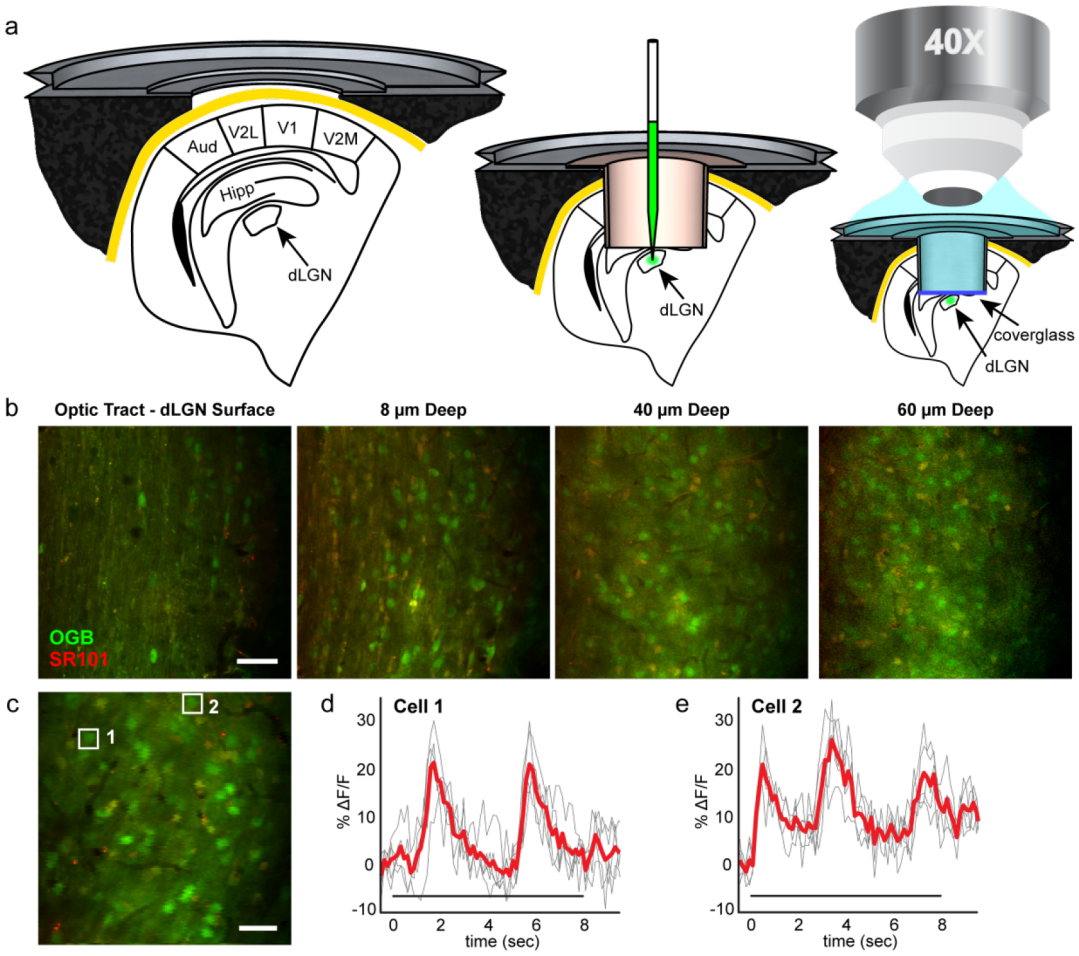

Figure 2.1 | **Two-photon calcium imaging of visual responses in the mouse dLGN.** **a**, Surgery and calcium dye loading procedure as described in Methods. Metal frame and probe cross sections, as well as anatomy (Paxinos, G. and Franklin, K. B. J., 2001) are drawn to scale. **b**, Images at multiple depths in the dLGN (Supplemental Movie 1). Lateral is up. **c**, Example field of view used for imaging visual responses. **d and e**, Change in fluorescence over time (ΔF/F) for neurons indicated by white boxes in (**c**). Cell 1 ($\mathbf{F_1}$ = 7.6 ± 0.4% ΔF/F) responds after Cell 2 ($\mathbf{F_1}$ = 5.9 ± 0.7% ΔF/F) indicating slightly shifted positions of their receptive fields relative to the same grating stimulus. Fourier magnitude is unaffected by these shifts in phase. Red line indicates mean over five trials; each trial is a gray line. Stimulus time indicated by bar under waveforms. Scale bars: (**b**), 50 µm (**c**), 25 µm.

Many neurons responded robustly and reliably to at least one direction of the drifting grating, characterized by a time-locked increase in fluorescence to the period of the drifting grating (n = 354, $\Delta\mathbf{F/F}$ amplitude at $\mathbf{F_1}$ or $\mathbf{F_2}$ > 2.5% and circular T^2 test $p < 0.05$; Supplemental Fig. 2.1). We used the modulation of the fluorescence signal at the temporal frequency of the grating (0.25 Hz, $\mathbf{F_1}$) or at twice the temporal frequency of the grating (0.5 Hz, $\mathbf{F_2}$) as the measure of neuronal responsiveness. The $\mathbf{F_1}$ modulation corresponds to either the onset (On) or offset (Off) of each bar of light passing through a cell's receptive field, while the $\mathbf{F_2}$ modulation corresponds to both the onset and offset (On-Off) of each bar of light. We computed the direction-selectivity index (**DSI**) and axis-selectivity index (**ASI**) of each responsive neuron in our sample. Neurons with high **DSI** values (**DSI** > 0.5) responded preferentially to a single direction of the grating. Neurons with high **ASI** values (**ASI** > 0.5) responded preferentially to gratings drifting along a single axis of motion, responding selectively to gratings drifting in either opposing direction along a motion axis at a single orientation. The majority of neurons were not selective for motion in a particular direction or along a particular axis (n = 320/354, Fig. 2.2b, **DSI** < 0.5 and **ASI** < 0.5). These responses are consistent with the approximately circularly-symmetric receptive fields typical of dLGN neurons (Grubb and Thompson, 2003; Hubel and Wiesel, 1961; Wang et al., 2011).

Conversely, 18 of the visually responsive cells in the dataset were strongly (**DSI** > 0.5) and consistently direction selective (example cells Fig. 2.2c,d and Fig. 2.3a, Hotelling T^2 test $p < 0.05$). The majority of these cells responded to both the onset and offset of each bar of light moving through their receptive field (n = 10/18,

$\mathbf{F_2}$ modulation), defining their receptive fields as On-Off and suggesting that they receive driving input from On-Off RGCs. We next tested for functional organization of preferred direction in the superficial dLGN population, based on our predictions from DSRGC projections. Unexpectedly, the majority of direction-selective lateral geniculate neurons (DSLGNs) were strongly selective for the anterior direction (n = 11/18, including one near the anterior-downward border, Fig. 2.2c and Fig. 2.3a), and the majority of these neurons were On-Off direction selective (n = 8/11). These results strongly predict a previously unknown retinogeniculate projection of On-Off anterior DSRGCs to the superficial dLGN layer. We found a smaller population of DSLGNs selective for the posterior direction (n = 5/18, including one near the posterior-downward border), and we were able to detect On-Off responses in one of these neurons (Fig. 2.2d), corroborating known pDSRGC projections to the superficial layer and perhaps reflecting the variety of On-Off response types inherent to that population (Huberman et al., 2009). Only one neuron was selective for upward motion, and one for downward motion (Fig. 2.3a), consistent with rare arborization of On-Off downward and Off upward DSRGCs axons in the superficial dLGN layer (Kim et al., 2010). These results predict that On-Off upward DSRGCs project to deeper dLGN. On DSRGCs have been shown to not send projections to the dLGN (Yonehara et al., 2009).

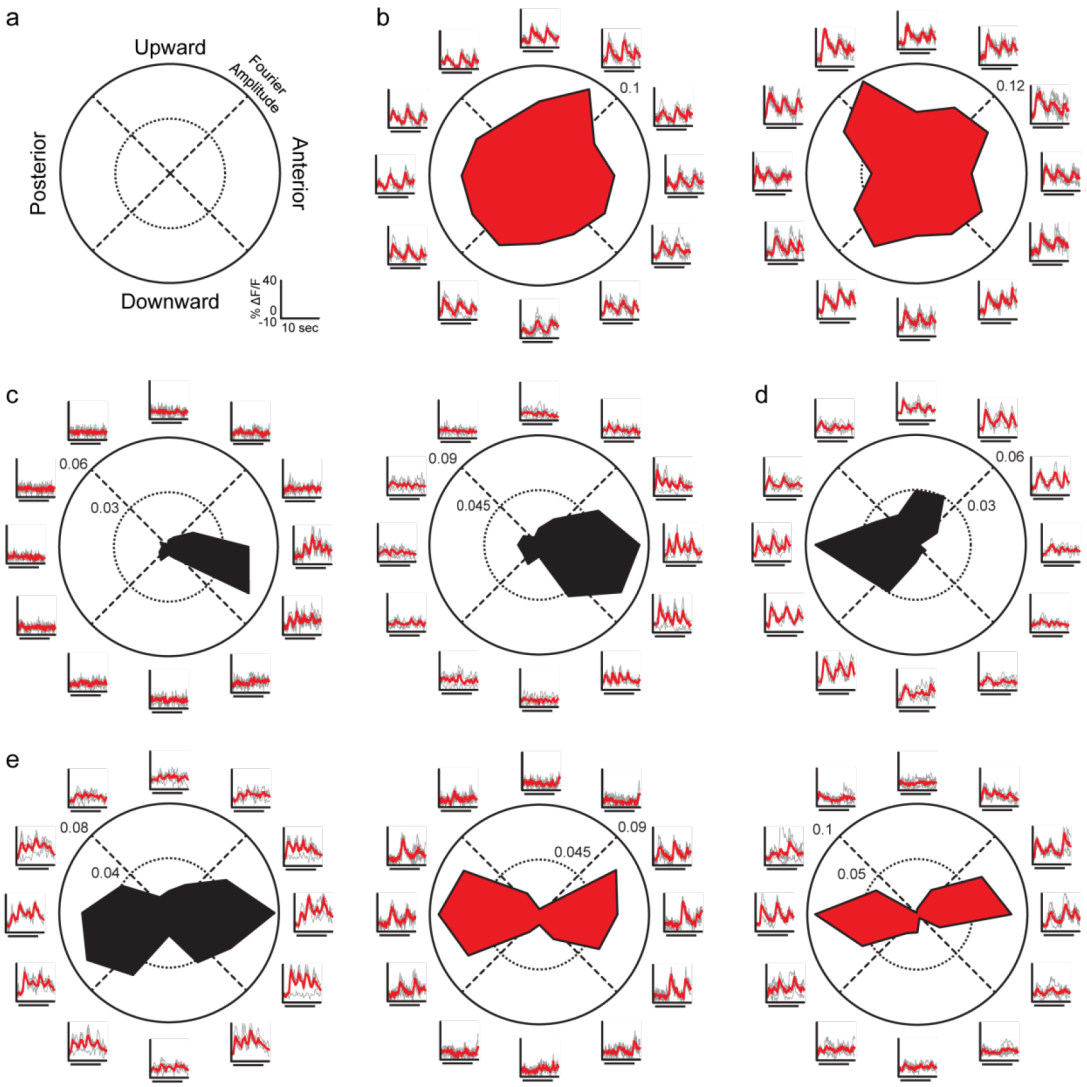

Figure 2.2 | **Direction and axis selectivity in the dLGN. a**, Polar plot legend for **b-e**, with directions in visual coordinates. Scale bars for fluorescence change (ΔF/F) and time in **b-e** are shown in lower right. Examples of non-direction-selective dLGN neurons (**b),** anterior direction-selective neurons (**c**), posterior direction-selective neuron (**d**), axis-selective neurons (**e**) are shown in **b-e**. Polar plots represent the magnitude of $\mathbf{F_1}$ (red) or $\mathbf{F_2}$ (black) response to each grating direction. Axes outside of the circle show the fluorescence time series, in units of percent change in fluorescence, in response to each direction of the grating. Individual trials (gray) are overlaid with the mean time series (red), where stimulus time (8 seconds) is indicated by bar under waveforms as in Fig. 2.1 (**d**,**e**).

Overall, the preferred directions of DSLGNs in the superficial 75 μm of the dLGN were distributed along a single axis (Fig. 2.3c, axial Rayleigh test, $p < 0.05$, unimodal Rayleigh test n.s.) corresponding to horizontal motion (fitted distribution < 2° from horizontal axis). Interestingly, anterior DSLGNs (aDSLGNs) were intermingled in depth with posterior DSLGNs (pDSLGNs) within the superficial 75 μm of the dLGN (Fig. 2.3d). The distributions of tuning width between pDSLGNs and aDSLGNs were indistinguishable from each other (t-test n.s.), and were far more sharply tuned for direction than reported for DSRGCs (mean width at half-maximum = 76 ± 7° (SE) for DSLGNs compared to 115° reported for DSRGCs (Elstrott et al., 2008), t-test $p < 0.05$). These results suggest that the dLGN both maintains and sharpens direction tuning in a subset of neurons and contains a preferred direction-biased superficial layer. Intriguingly, the direction-selective neurons in this layer overwhelmingly encode opposite directions along a single axis of motion.

Given the precedence set by these findings, and the general agreement of the receptive field dLGN data with known DSRGC projection patterns, anterior DSRGCs may avoid projections to deep layers, and upward and downward DSRGCs may overlap projections in a deep layer, giving rise to a similar layer of direction opponency in deep dLGN representing vertical motion. Taken together, these results suggest a striking model of functional organization in which the cardinal axes of visual motion are separated in the dLGN.

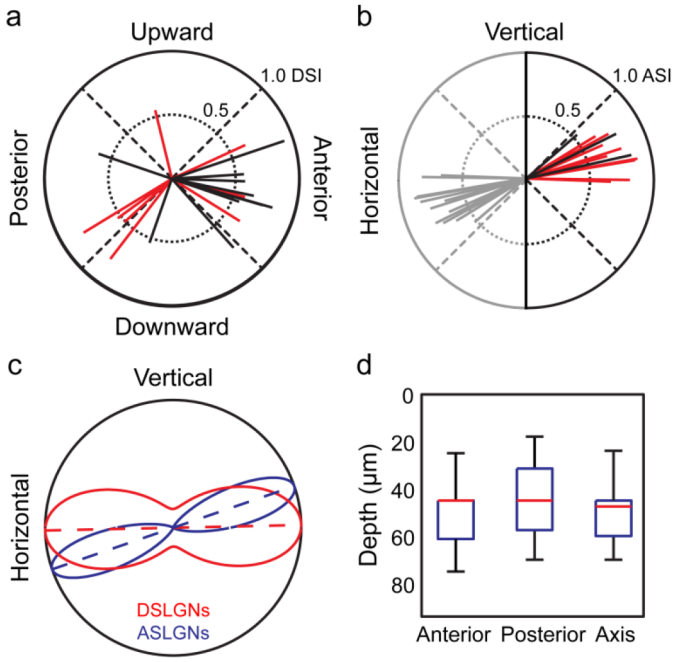

Figure 2.3 | **The superficial dLGN is selective for horizontal motion. a**, Each vector on polar plot indicates a direction-selective neuron. Direction of vector indicates direction preference. **b**, Each vector indicates an axis-selective neuron. Direction of vector indicates axis preference. Vectors are reflected (gray) for display purposes, and represent the same data as black and red vectors. **a and b**, Length of vectors indicates level of direction selectivity (DSI) or axis selectivity (ASI). Black lines indicate On-Off response ($\mathbf{F_2}$ modulation) and red lines indicate $\mathbf{F_1}$ modulation. **c**, Maximum likelihood fit of axial circular Gaussian distributions to the observed populations of direction- and axis-selective neurons from (**a)** and (**b)**. Curves represent the axial Gaussian model's probability of observing a direction- (red) or axis-selective (blue) neuron with a given preferred direction or preferred axis. Dotted lines indicate preferred axis for each population, and curves are normalized to equalize the maximum probability density for visualization. Both populations prefer axes representing horizontal motion. **d**, Depth of neuron populations in dLGN dataset depending on stimulus selectivity. Whiskers are complete depth range, boxes are 25th to 75th percentile, and the red line is the median depth. Anterior-, posterior- and axis-selective neurons overlap locations in depth.

This prompted us to next investigate whether the dLGN integrates across opposing directions of motion to form axis-of-motion-selective neurons within the same layer. We found evidence for this effect: 15 of the visually responsive neurons

were highly selective for a particular axis of motion, at a single orientation of the grating (Fig. 2.2e, **ASI** > 0.5). The preferred axis of motion of these neurons was also biased towards a single axis (Axial Rayleigh test, $p < 0.05$, unimodal Rayleigh test n.s.), corresponding to horizontal motion (Fig. 2.3c). The preferred motion axis for axis-selective neurons was not significantly different than the axis for direction-selective neurons (Watson-Williams test; fitted distribution < 20° from horizontal axis). Furthermore, axis-selective lateral geniculate neurons (ASLGNs), pDSLGNs and aDSLGNs were intermingled in depth within the superficial 75 μm of the dLGN (one-way ANOVA n.s.). ASLGNs, like DSLGNs, were more sharply tuned than DSRGCs (mean width at half-maximum = 61 ± 2° (SE) for ASLGNs compared to 115° reported for DSRGCs (Elstrott et al., 2008), t-test $p < 0.05$). At least one axis-selective neuron showed On-Off responses (Fig. 2.2e, cell 1, $\mathbf{F_2/F_1} > 1$).

To our knowledge, neurons selective for a particular axis of motion have not been observed in the mammalian retina, nor have highly orientation-selective On-Off RGCs (Venkataramani and Taylor, 2010). We observed neurons that responded to opposing directions of a drifting grating that matched the preferences of the direction-selective neurons in the same dLGN layer. It is possible that these responses could be explained by an elongated linear receptive field (orientation selectivity). However, the fact that the preferred axis of these neurons matched the direction preferences of the DSLGNs may imply that the axis-selective neurons we observe here generate motion-selective receptive fields *de novo*, perhaps relying on precise integration of opposing direction-selective inputs which overlap axonal arbors within the same layer. In the adult mouse and other species, only ~1-3 RGC axons form strong functional synapses

onto a thalamic relay cell (Chen and Regehr, 2000; Cleland et al., 1971). While the number of retinal input neurons is sparse, each input RGC strongly drives the membrane potential of the postsynaptic neuron (Chen and Regehr, 2000), leading to highly correlated receptive fields of RGCs and their target relay neurons in the dLGN (Cleland et al., 1971; Usrey et al., 1999). In this scheme, it would be highly improbable for the large proportion of axis-selective neurons relative to direction-selective neurons we observed in our sample population to be based on purely random retinogeniculate wiring of 2 or more opposing DSRGCs to a given relay cell, especially since our results suggest that the great majority of input to the superficial dLGN is not direction selective. Instead, this may imply a developmental mechanism favoring specific retinogeniculate wiring to integrate direction information from 2 or more DSRGC inputs to form axis-of-motion selectivity in the dLGN.

The direction-selective and axis-selective responses we observed in the mouse dLGN were far more sharply tuned for direction than reported for mouse On-Off DSGCs (Huberman et al., 2009; Kim et al., 2010; Weng et al., 2005; Elstrott et al., 2008). Given the absence of cortical feedback in our preparation (most of the visual cortex was removed during surgery to gain access to the dLGN for imaging), the observed sharpening of directional tuning likely occurs via local circuit mechanisms within the dLGN. General sharpening of visual stimulus selectivity in the dLGN compared with the retina has been previously explained as arising from either nonlinear postsynaptic summation (Carandini et al., 2007) or precisely targeted feedforward inhibition mediated by local circuit interneurons (Levick et al., 1969; Wang et al., 2011). Levick, Oyster and Takahashi 1969 proposed that sharpening of

direction tuning in the rabbit dLGN emerges from direction-selective inhibitory input onto a principal dLGN neuron selective for the opposite direction. Along these lines, intracellular recordings of relay neurons have revealed inhibitory inputs with precisely opposing spatial receptive fields (Wang et al., 2011). Laminar organization of opposing direction information may help facilitate a similar local circuit for motion processing. To further sharpen direction tuning, inhibitory dLGN neurons could integrate motion information along one axis (i.e., vertical) in one layer and suppress activity along this axis in postsynaptic neurons preferring a direction along the orthogonal axis in another layer (i.e., anterior). Furthermore, the functional-anatomical organization of opposing direction information in the dLGN creates a local population of highly anti-correlated (and therefore redundant) neurons, perhaps leading to a form of error reduction in the motion-selective pathway.

By both sharpening and integrating direction information within a laminar functional organization, the dLGN appears to not merely relay direction information from the retina to cortex, but instead organizes and manipulates that information before projecting it downstream. Future studies examining the direction sensitivity of inhibitory neurons and the connectivity between direction-selective principal neurons and inhibitory neurons within the dLGN, as well as direct functional connectivity analyzed from the retina to thalamus to cortex, may shed light on the mechanisms underlying these computations. The methods developed and demonstrated here are likely to aid functional studies of the inhibitory circuitry of the dLGN (Wang et al., 2011). Furthermore, the influence of these computations and the functional-anatomical

organization of direction information in the dLGN on visual cortical processing and behavior remain open questions.

Methods

In vivo preparation

All experiments involving living animals were approved by the Salk Institute's Institutional Animal Care and Use Committee. C57Bl/6 mice (n = 7 animals) were anesthetized with isoflurane (1-1.5%). A custom metal frame was mounted to the skull centered over dLGN stereotaxic coordinates (Fig. 1a). The frame was a thin round plate, 1 cm diameter and 1 mm thick. A triangular notch in the side of the frame fit into a holding mount that formed a large well around the frame, aided in light shielding, and secured the frame (and mouse) to the optics table. A counterbore in the frame with ~8 mm diameter formed a small well in the frame and allowed clearance for the objective. A second counterbore with 5 mm diameter served as a notched locator for the custom probes described below. A 3 mm aperture was centered in the frame. A craniotomy was made within the aperture, and the exposed cortex and underlying hippocampus were aspirated, exposing the thalamus. The brain was rinsed with artificial cerebral spinal fluid (ACSF; in mM: 150 NaCl, 2.5 KCl, 2 $CaCl_2$, 1 $MgCl_2$, 10 HEPES) and a temporary ~3 mm long cylindrical probe was inserted for stability. A glass pipette was lowered through the cylinder into the dLGN. Oregon Green Bapta-1 AM (OGB) and sulforhodamine 101 (SR101) were injected with 150 ms pulses every 15 sec for 15 min at 200 μm below the dLGN surface and again at

400 µm. The temporary probe was replaced with a permanent probe with a glass coverslip sealed to the bottom. This probe was glued in place forming a chamber, which was filled with ACSF. Each of these probes were shaped as a combination of a cylinder, which was lowered into the brain, and a flat round rim with 5 mm diameter that fit into the frame's counterbore, holding it properly in place. OGB-loaded neurons were imaged through the probe using 925 nm excitation with a conventional water-immersion objective (Zeiss 40X, 3.6 mm working distance), attached to the end of a custom-built, light-shielded version of the moveable objective two-photon microscope (Sutter). Images were acquired at 4-8 Hz. This strategy for deep-brain, two-photon imaging was adapted from similar protocols for imaging in the hippocampus (Mizrahi et al., 2004; Dombeck et al., 2010). For visual stimulation, chlorprothixene (1 mg/kg, IM) was administered every 4 hours and isoflurane was lowered to 0.3-0.5%.

Visual stimulation

Drifting square wave gratings were presented on a calibrated LCD monitor (60 Hz, 34 x 27.5 cm) placed 15 cm from the mouse's eye, along an axis parallel to the mouse's retina. Gratings were 8 sec duration, 0.01 cpd, and drifted at 25 deg/sec (0.25 Hz) in 12 directions spaced 30 deg apart including: nasal, temporal, superior and inferior, corresponding to anterior, posterior, upward and downward. A blank stimulus was a uniform gray screen. For each field of view containing a unique population of neurons, each stimulus was presented 5 times to the animal, in random order, while movies of OGB fluorescence were recorded using the microscope and ScanImage software (Pologruto et al., 2003) running on Matlab (Mathworks).

Data Analysis

Each image frame was cross-correlated with a template image to correct for movement. Most trials had only subpixel movements during stimulus presentation. Regions of interest (ROI) were drawn around each cell in each field of view, excluding glia using sulforhodamine 101 labeling (Nimmerjahn et al., 2004), and pixels were averaged within each ROI. The measured fluorescence change relative to a prestimulus baseline ($\Delta \mathbf{F/F}$) was calculated and used in all subsequent analyses. Stimulus-evoked response was assessed by taking the Fourier transform of the fluorescence signal at the stimulus frequency ($\mathbf{F_1}$; 0.25 Hz in all experiments) and at twice the stimulus frequency ($\mathbf{F_2}$; 0.5 Hz). This method has been used to analyze electrophysiological recordings of neurons under periodic visual stimulation since, compared to the mean, it better distinguishes neuronal response classes to periodic stimuli (Hochstein and Shapley, 1976) and is insensitive to shifts in phase and suppression below baseline. We found this to be true for dLGN calcium responses, and frequency domain analysis provided information about the trial-to-trial reliability of responses used in subsequent analyses. Neurons were classified as visually responsive if they showed an $\mathbf{F_1}$ or $\mathbf{F_2}$ modulation greater than 2.5%, corresponding to a peak-to-trough height of at least 5%. The circular T^2 test (Victor and Mast, 1991) was used to further restrict our analysis to neurons for which the phase and magnitude of the corresponding Fourier amplitude ($\mathbf{F_1}$ or $\mathbf{F_2}$) was distinguishable from the blank condition (Supplemental Fig. 1, $p < 0.05$).

Five trials were performed at each direction of the grating, and the magnitude of the mean $\mathbf{F_1}$ or $\mathbf{F_2}$ amplitude was used as the measure of neural responsiveness.

Strict criteria for direction selectivity were used, by choosing only those cells which had a Direction Selectivity Index (DSI) > 0.5 by both max-null and circular variance metrics:

$$DSI_{max-null} = \frac{r_{max} - r_{null}}{r_{max} + r_{null}}$$

$$DSI_{circvar} = \frac{|\sum r_k exp(i\theta_k)|}{\sum r_k},$$

where r_k is the $\mathbf{F_1}$ or $\mathbf{F_2}$ magnitude at direction k. In order to test for reliability of direction selectivity, the Hotelling T^2 test was performed on five resampled resultants ($\sum r_k \exp(i\theta_k)$) to see whether they were distinguishable from the origin at the $p < 0.05$ level. We bootstrapped this p value by generating 1000 samples of five resultants where each resultant has one independent, randomly chosen trial at each direction, and taking the mean p value as the true value. Cells for which $\mathbf{F_2}$ or $\mathbf{F_1}$ modulation met these criteria were considered direction selective for further analysis, and $\mathbf{F_2}$ modulated neurons were defined as On-Off. Despite the low-pass filtering inherent in the spike to calcium transformation, most $\mathbf{F_2}$ modulated direction selective neurons had a greater $\mathbf{F_2}$ than $\mathbf{F_1}$ modulation (n = 6/10).

We then fit each set of responses to a circular Gaussian (von Mises) distribution, which is described as

$$r_{max}\frac{exp(\kappa \cos(x - \mu))}{exp(\kappa)},$$

and described the tuning width via the relation for the full width at half-maximum

$$FWHM = 2 * \arccos\left(\frac{\ln(\frac{1}{2}e^k + \frac{1}{2}e^{-k})}{k}\right),$$

as in Elstrott et al., 2008.

For population analysis of direction selectivity, the preferred direction of all direction-selective neurons (Fig. 2.3a) was transformed by multiplication by 2 in order to map opposing directions onto one another. The resulting distribution was tested for unimodality with a Rayleigh test ($p < 0.05$), and a maximum likelihood fit to a circular Gaussian (von Mises) distribution was used to demonstrate the angle and sharpness of axial tuning (Fig. 2.3c). The same procedure was performed for axis-selective neurons ($\mathbf{F_1}$ and $\mathbf{F_2}$; Fig. 2.3b,c).

Supplementary Materials

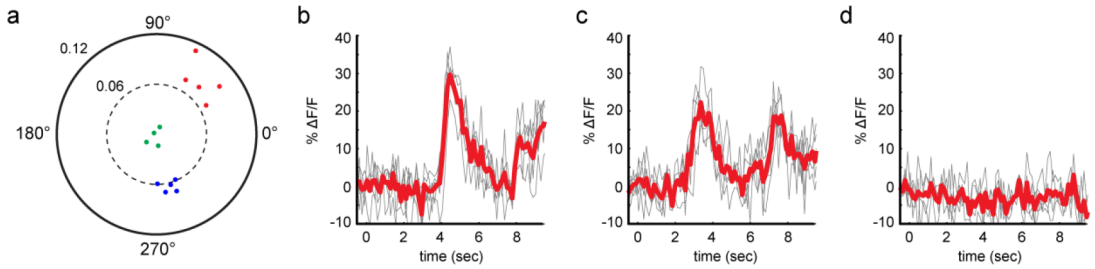

Supplementary Figure 2.1 | Reliability of F_1 responses of an individual neuron to drifting gratings. **a**, Polar plot shows phase (angle) and magnitude (radius, with inner circle 6% and outer circle 12% ΔF/F) of $\mathbf{F_1}$ modulation for individual trial responses to drifting gratings at 180 degrees (blue dots) and 0 degrees (red dots), and to a blank gray screen (green dots). The circular T^2 statistic[35] is used to determine the probability that a response at a given direction overlaps with the response to the blank, and is derived from the ratio of the variance within conditions (chosen direction or blank) to the variance between conditions (distance between chosen direction and blank). Note that the response magnitude used in defining direction selectivity is defined to be the distance between the origin and the center of a particular cloud of points. **b,c,d**, Fluorescence time series of individual trials (gray) and mean responses (red) to drifting gratings at 180 degrees (b), drifting gratings at 0 degrees (c) and gray screen (d).

Supplementary Movie 2.1 | Two-photon structural image stack of multiple depths in dLGN.

Movie of OGB-loaded neurons in superficial dLGN, showing the appearance of the optic tract fibers at the surface and cells at different depths (each image is normalized to maintain constant brightness across stack; 0.61 microns between images, field of view ~300 microns square). The progression from fibers with embedded cells to cells without fibers is apparent, as is the presence of small blood vessels with the characteristic appearance of the vasculature in this region. Thalamic glia labeled with sulforhodamine 101 (red cells) are visible in the movie, and were excluded in visual response analyses. Available for download online.

Acknowledgments

We thank the Callaway lab for helpful discussions and technical assistance. We also thank D. Kleinfeld for helpful discussions and D. Dombeck for imaging advice. We acknowledge support from NIH grants EY01742 (EMC), 1F30DC010541-01 (AK) and EY019821 (IN).

Publication Acknowledgments

Chapter 2, in full, has been submitted for publication of the material as it may appear in publication, Marshel, James H.; Kaye, Alfred P.; Nauhaus, Ian; Callaway, Edward M.. The dissertation author was co-primary investigator and author of this paper.

References

Briggman, K. L., Helmstaedter, M., and Denk, W. (2011). Wiring specificity in the direction-selectivity circuit of the retina. Nature *471*, 183-188.

Carandini, M., Horton, J. C., and Sincich, L. C. (2007). Thalamic filtering of retinal spike trains by postsynaptic summation. J Vis *7*, 20.1-11.

Chen, C., and Regehr, W. G. (2000). Developmental remodeling of the retinogeniculate synapse. Neuron *28*, 955-966.

Cleland, B. G., Dubin, M. W., and Levick, W. R. (1971). Simultaneous recording of input and output of lateral geniculate neurones. Nature New Biol *231*, 191-192.

Dombeck, D. A., Harvey, C. D., Tian, L., Looger, L. L., and Tank, D. W. (2010). Functional imaging of hippocampal place cells at cellular resolution during virtual navigation. Nat. Neurosci *13*, 1433-1440.

Elstrott, J., Anishchenko, A., Greschner, M., Sher, A., Litke, A. M., Chichilnisky, E. J., and Feller, M. B. (2008). Direction selectivity in the retina is established independent of visual experience and cholinergic retinal waves. Neuron *58*, 499-506.

Euler, T., Detwiler, P. B., and Denk, W. (2002). Directionally selective calcium signals in dendrites of starburst amacrine cells. Nature *418*, 845–852.

Fried, S. I., Münch, T. A., and Werblin, F. S. (2002). Mechanisms and circuitry underlying directional selectivity in the retina. Nature *420*, 411–414.

Grubb, M. S., and Thompson, I. D. (2003). Quantitative characterization of visual response properties in the mouse dorsal lateral geniculate nucleus. J. Neurophysiol *90*, 3594-3607.

Hochstein, S., and Shapley, R. M. (1976). Quantitative analysis of retinal ganglion cell classifications. J. Physiol. (Lond.) *262*, 237-264.

Hubel, D. H., and Wiesel, T. N. (1961). Integrative action in the cat's lateral geniculate body. J. Physiol. (Lond.) *155*, 385-398.

Huberman, A. D., Wei, W., Elstrott, J., Stafford, B. K., Feller, M. B., and Barres, B. A. (2009). Genetic Identification of an On-Off Direction- Selective Retinal Ganglion Cell Subtype Reveals a Layer-Specific Subcortical Map of Posterior Motion. Neuron *62*, 327-334.

Jaubert-Miazza, L., Green, E., Lo, F.-S., Bui, K., Mills, J., and Guido, W. (2005). Structural and functional composition of the developing retinogeniculate pathway in the mouse. Vis. Neurosci *22*, 661-676.

Kay, J. N., De la Huerta, I., Kim, I.-J., Zhang, Y., Yamagata, M., Chu, M. W., Meister, M., and Sanes, J. R. (2011). Retinal ganglion cells with distinct directional preferences differ in molecular identity, structure, and central projections. J. Neurosci *31*, 7753-7762.

Kerlin, A. M., Andermann, M. L., Berezovskii, V. K., and Reid, R. C. (2010). Broadly tuned response properties of diverse inhibitory neuron subtypes in mouse visual cortex. Neuron *67*, 858-871.

Kerr, J. N. D., Greenberg, D., and Helmchen, F. (2005). Imaging input and output of neocortical networks in vivo. Proc. Natl. Acad. Sci. U.S.A *102*, 14063-14068.

Kim, I.-J., Zhang, Y., Meister, M., and Sanes, J. R. (2010). Laminar restriction of retinal ganglion cell dendrites and axons: subtype-specific developmental patterns revealed with transgenic markers. J. Neurosci *30*, 1452-1462.

Kim, I.-J., Zhang, Y., Yamagata, M., Meister, M., and Sanes, J. R. (2008). Molecular identification of a retinal cell type that responds to upward motion. Nature *452*, 478-482.

Levick, W. R., Oyster, C. W., and Takahashi, E. (1969). Rabbit lateral geniculate nucleus: sharpener of directional information. Science *165*, 712-714.

Mizrahi, A., Crowley, J. C., Shtoyerman, E., and Katz, L. C. (2004). High-resolution in vivo imaging of hippocampal dendrites and spines. J. Neurosci *24*, 3147-3151.

Montero, V. M., and Brugge, J. F. (1969). Direction of movement as the significant stimulus parameter for some lateral geniculate cells in the rat. Vision Research *9*, 71–88.

Nimmerjahn, A., Kirchhoff, F., Kerr, J. N. D., and Helmchen, F. (2004). Sulforhodamine 101 as a specific marker of astroglia in the neocortex in vivo. Nat. Methods *1*, 31-37.

Oyster, C. W., and Barlow, H. B. (1967). Direction-selective units in rabbit retina: distribution of preferred directions. Science *155*, 841.

Paxinos, G., and Franklin, K. B. J. (2001). The mouse brain in stereotaxic coordinates 2nd ed. (Academic Press).

Peterson, M. R., Li, B., and Freeman, R. D. (2004). The derivation of direction selectivity in the striate cortex. J. Neurosci *24*, 3583-3591.

Pologruto, T. A., Sabatini, B. L., and Svoboda, K. (2003). ScanImage: flexible software for operating laser scanning microscopes. Biomed Eng Online *2*, 13.

Sumitomo, I., and Iwama, K. (1977). Some properties of intrinsic neurons of the dorsal lateral geniculate nucleus of the rat. Jpn. J. Physiol *27*, 717-730.

Usrey, W. M., Reppas, J. B., and Reid, R. C. (1999). Specificity and strength of retinogeniculate connections. J. Neurophysiol *82*, 3527-3540.

Venkataramani, S., and Taylor, W. R. (2010). Orientation selectivity in rabbit retinal ganglion cells is mediated by presynaptic inhibition. J. Neurosci *30*, 15664-15676.

Victor, J. D., and Mast, J. (1991). A new statistic for steady-state evoked potentials. Electroencephalogr Clin Neurophysiol *78*, 378-388.

Wang, X., Vaingankar, V., Sanchez, C. S., Sommer, F. T., and Hirsch, J. A. (2011). Thalamic interneurons and relay cells use complementary synaptic mechanisms for visual processing. Nat. Neurosci *14*, 224-231.

Wei, W., Hamby, A. M., Zhou, K., and Feller, M. B. (2010). Development of asymmetric inhibition underlying direction selectivity in the retina. Nature *469*, 402–406.

Weng, S., Sun, W., and He, S. (2005). Identification of ON-OFF direction-selective ganglion cells in the mouse retina. J. Physiol. (Lond.) *562*, 915-923.

Yonehara, K., Balint, K., Noda, M., Nagel, G., Bamberg, E., and Roska, B. (2011). Spatially asymmetric reorganization of inhibition establishes a motion-sensitive circuit. Nature *469*, 407-410.

Yonehara, K., Ishikane, H., Sakuta, H., Shintani, T., Nakamura-Yonehara, K., Kamiji, N. L., Usui, S., and Noda, M. (2009). Identification of retinal ganglion cells and their projections involved in central transmission of information about upward and downward image motion. PLoS ONE *4*, e4320.

CHAPTER III

TARGETING SINGLE NEURONAL NETWORKS FOR GENE EXPRESSION AND CELL LABELING *IN VIVO*

Summary

To understand fine-scale structure and function of single mammalian neuronal networks, we developed and validated a novel strategy to genetically target and trace monosynaptic inputs to a single neuron *in vitro* and *in vivo*. The strategy independently targets a neuron and its presynaptic network for specific gene expression and fine-scale labeling, using single-cell electroporation of DNA to target infection and monosynaptic retrograde spread of a genetically modifiable rabies virus. The technique is highly reliable, with transsynaptic labeling occurring in every electroporated neuron infected by the virus. Targeting single neocortical neuronal networks *in vivo*, we found clusters of both spiny and aspiny neurons surrounding the electroporated neuron in each case, in addition to intricately-labeled distal cortical and subcortical inputs. The broad applicability of this technique to probe and manipulate single neuronal networks with single-cell resolution *in vivo* may shed new light on fundamental mechanisms underlying circuit development and information processing by neuronal networks throughout the brain.

Introduction

A single mammalian neuron maintains as many as thousands of input synapses and integrates combinations of activity from these inputs in time to determine the probability that it will fire an action potential at any given moment. This input-

dependent computation occurs for every neuron continuously over time, and forms the basis for the diverse and complex computations performed by neuronal networks throughout the brain (Somogyi et al., 1998). Each single neuronal network exists in a tangled web of as many as trillions of connections between billions of neurons spanning the entire brain confounding attempts to identify detailed circuits and relate circuits to function *in vivo*. We sought to overcome this technological barrier and facilitate the direct analysis of the fine scale structure and function of single neuronal networks by developing and validating a robust and reliable technique to target a single neuron and its monosynaptic inputs for independent gene expression and detailed cell labeling both *in vitro* and *in vivo.* Identifying and genetically targeting single neuronal networks *in vivo* will hasten understanding the link between connectivity and function of neuronal networks with single cell resolution in the intact brain. Targeting a single neuron and its direct inputs for gene expression provides a means to probe and manipulate neuronal spiking behavior and draw cause-effect relationships between pre and postsynaptic activity. Furthermore, it can be used to determine the role of specific proteins in the input-dependent synaptic development and computation of single neurons. Here, we demonstrate a novel strategy for robust and efficient single microcircuit targeting. We exhibit the utility of the technique by mapping monosynaptic inputs to single layer 2/3 pyramidal neurons in mouse neocortex, *in vivo*. We identify a variety of cell types that directly connect to these neurons, including local inputs predicted by other methods, and more distant inputs described here for the first time.

To date, the most detailed studies of brain microcircuitry have relied on multiunit recordings in brain slice preparations. These studies have begun to forge a map of connectivity distributions between several distinct neuronal cell types in different brain areas, and described fundamental mechanisms of information processing by single neurons (Brown and Hestrin, 2009a; Thomson and Lamy, 2007). Moreover, these studies have revealed that even neighboring neurons connect to each other only in a minority of cases (Markram et al., 1997; Song et al., 2005; Thomson et al., 1993; Yoshimura and Callaway, 2005; Yoshimura et al., 2005). Nevertheless, the connections which are identified are not random; connections differ according to cell type and can form precise subnetworks (Brown and Hestrin, 2009b; Kampa et al., 2006; Kozloski et al., 2001; Lefort et al., 2009; Petreanu et al., 2007; Petreanu et al., 2009; Song et al., 2005; Thomson and Lamy, 2007; Thomson et al., 2002; Wang et al., 2006; Yoshimura and Callaway, 2005; Yoshimura et al., 2005). However, the conclusions that can be drawn from these studies are limited because they do not examine the relationship between connectivity and function in the intact, functioning brain. Furthermore, slicing the brain severs connections with distant structures and between a significant population of nearby neurons (Stepanyants et al., 2009). As a result, characterization of functional properties of synaptic connections or integration of inputs from multiple sources is limited to cell pairs that can be readily sampled, making it impractical to sample large populations of connected neurons, or connections that occur at low probabilities or originate from distant sources (Thomson and Lamy, 2007). Slicing the brain also correlates with a substantial, rapid increase in

synapse number compared to tissue fixed *in vivo* (Kirov et al., 1999), and the effects of this rapid synaptogenesis on single-cell connectivity distributions are unknown.

To overcome these limitations and provide a means for studying the connectivity and function of single neuronal networks in the intact brain, we developed and implemented a novel method for determining the monosynaptic inputs to a single neuron *in vivo*. The method labels the fine scale morphology of traced neurons permitting detailed anatomical characterization and also allows both a single neuron and its input neuron population to be manipulated genetically. Furthermore, the technique is applicable across neuronal cell types throughout the brain, and across species, and may be compatible with functional analyses of labeled cells. By tracing the inputs to single neurons within and across different neuronal cell classes and brain regions, it will be possible to answer many longstanding questions about fine scale connectivity throughout the nervous system. Genetically targeting a single neuron and its input population should make it possible to study the function of different cell types and specific genes as they relate to connectivity, synaptic development, and information processing. For example, it may provide a means to probe and manipulate the function of neurons within a targeted network in combination with existing genetic technologies in order to understand how single neurons integrate their specific inputs in time to generate their unique output firing pattern. Modulating gene expression patterns of specific proteins in either the postsynaptic neuron or the entire targeted microcircuit makes it possible to test the role of different proteins (e.g., specific ion channels or proteins related to synapse development and maintenance) on the input-specific computation performed by the postsynaptic neuron. Understanding how

distinct cell types, particular genes, intrinsic cellular properties, and patterns of synaptic input influence information processing by neurons within identified microcircuits will provide insights into the basic mechanisms employed by the brain to perform the diversity of computations necessary for its function.

Single Cell Tracing Strategy

The single cell tracing strategy we demonstrate here develops upon two foremost genetic technologies to target independent gene expression to a single neuron and its monosynaptic neuronal inputs: *in vivo* two-photon guided single cell electroporation (Kitamura et al., 2008), and a genetically engineered variant of rabies virus that restricts retrograde tracing to the monosynaptic inputs of a genetically targeted neuronal population (Wickersham et al., 2007b).

Single Cell Electroporation

Within the last decade, single cell electroporation has been developed as an efficient transfection method of single cells in primary cell culture, brain slice culture, and most recently, in the living rodent (Kitamura et al., 2008; Rae and Levis, 2002; Rathenberg et al., 2003). By balancing the parameters necessary to promote efficient gene delivery and optimize cell viability, these studies have demonstrated reliable and effective methods for transfecting single neurons with one or more genes across a variety of cell types, brain regions and species (Haas et al., 2001; Judkewitz et al.,

2009; Kitamura et al., 2008; Rathenberg et al., 2003). Using single cell electroporation, it has also been possible to knockdown gene expression via RNA interference in single neurons in neocortical and cerebellar cell cultures (Boudes et al 2008, Tanaka et al 2009), and deliver dyes, calcium indicators and activity modulators (e.g., channelrhodipsin-2 (ChR2)) to study neuronal function *in vivo* (Judkewitz et al., 2009; Kitamura et al., 2008; Nevian and Helmchen, 2007). The wide applicability of single cell electroporation to manipulate single neurons throughout the nervous system makes it a powerful tool for targeting and studying single neurons. Here, we applied single cell electroporation to transfect a single neuron with genes to target infection and transsynaptic spread of a monosynaptic, retrograde tracing rabies virus so as to isolate a single neuron and its direct presynaptic inputs for anatomical, functional and genetic analyses.

Monosynaptic Tracing Rabies Virus

Wild-type rabies is a neurotropic virus that specifically infects neurons via their axon terminals, and propagates exclusively in the retrograde direction—from a host neuron to its presynaptic inputs, making it a powerful, natural neuronal circuit tracer (Kelly and Strick, 2000; Ugolini, 1995). Wild-type rabies has been used to map connectivity between a variety of cortical and subcortical brain areas in several species (Astic et al., 1993; Kelly and Strick, 2003; Nassi and Callaway, 2006; Ugolini, 1995). In order to more precisely map neuronal connectivity at the microcircuit level, rabies virus has been modified in several ways to provide greater control over the infection

and transsynaptic spread of the virus. A genetically modified version of the virus has been produced, deleting the rabies glycoprotein gene (G) from the rabies negative-sense RNA genome and replacing it with the gene for a fluorescent marker protein to limit transsynaptic spread and intricately label infected neurons (Wickersham et al., 2007a). Expression of the glycoprotein gene on the surface of the virus is necessary for the rabies virus to infect other neurons, and confers the virus' characteristic transsynaptic infection (Mebatsion et al., 1996a; Wickersham et al., 2007a). To restrict initial infection of the virus to a genetically targeted population of neurons, the glycoprotein was replaced on the surface of the G-deleted virus with an envelope protein from an avian virus (Wickersham et al., 2007b). In this study, Wickersham et al., 2007b targeted a population of neurons *in vitro* for virus infection by biolistics transfection of the highly specific receptor TVA for the avian sarcoma and leukosis virus envelope protein EnvA (Lewis et al., 2001; Young et al., 1993), which had been coated on G-deleted rabies virus by a pseudotyping strategy. Since mammalian neurons do not naturally express the TVA receptor, and thus are not normally infected by EnvA coated virus, the EnvA pseudotyped G-deleted virus (SADΔG-EGFP(EnvA)) only infected the neurons expressing the TVA receptor from biolistics transfection. By co-transfecting the gene for the rabies glycoprotein in the same neurons, the G-deleted virus produced glycoprotein coated virus particles in these neurons that were able to transsynaptically infect presynaptic neurons. Since the G-deleted virus did not carry the glycoprotein gene itself, and the gene was not transfected in the presynaptic neurons by any other means, the virus was trapped in the monosynaptic inputs to the originally infected neuron population, and did not infect

further connections. Since the virus also expressed the gene for EGFP, all infected neurons were labeled in great detail. Co-transfecting a red fluorescent marker in the biolistics step labeled the postsynaptic neurons uniquely. Using this labeling to guide paired recordings between nearby pre and postsynaptic neurons proved that the labeled neurons were functionally and monosynaptically connected (Wickersham et al., 2007b).

Single Cell Tracing Strategy - Method Paradigm

Here, we established a method for limiting initial infection of the EnvA pseudotyped G-deleted rabies virus to a single neuron both *in vitro* and in the living rodent, so as to target a single neuron and its monosynaptic inputs for interrogation *in vitro* and *in vivo*. By adapting protocols for single cell electroporation and determining the parameters necessary for efficient *in vivo* expression of multiple electroporated genes and viral infection of a single neuron, we developed and validated a robust and reliable technique to genetically target and intricately label single neuronal networks *in vitro* and *in vivo.*

The single cell tracing strategy relies on three steps (Fig. 3.1). First, a single neuron is targeted for expression of three genes by single cell electroporation of plasmid DNA (Fig. 3.1A). The three genes encode for: 1) a marker fluorescent protein (XFP), 2) an avian virus receptor (TVA), and 3) the rabies glycoprotein (G). Second, one to three days later only the electroporated neuron is infected with a G-deleted rabies virus, pseudotyped with the avian sarcoma and leukosis virus (ASLV-A) glycoprotein, EnvA (Fig. 3.1B). This virus is termed SADΔG-XFP(EnvA), and can

be modified to encode a gene of interest in the glycoprotein locus (Wickersham et al., 2007a; Wickersham et al., 2007b; Mebatsion et al., 1996b; unpublished observations, T.M. and E.M.C.). The virus only infects the electroporated neuron and no other cells because the EnvA coated virus requires the TVA receptor to mediate infection, and the electroporated neuron is the only cell expressing this receptor (Wickersham et al., 2007b; Young et al., 1993). The virus replicates in the electroporated host neuron and uses the rabies glycoprotein expressed from the electroporated plasmids to retrogradely infect directly presynaptic neurons and label them with a unique fluorescent marker protein encoded in the rabies genome. The virus does not spread from these neurons to any further connections because these neurons lack the glycoprotein gene, which is necessary for transsynaptic infection. Lastly, after 3-6 days the tissue is fixed in paraformaldehyde and analyzed for fluorescent gene expression (Fig. 3.1C). Here, we developed parameters for single cell electroporation in brain slice culture and *in vivo* in the living rodent to introduce the three genes into single cortical neurons both *in vitro* and *in vivo*. We applied the EnvA pseudotyped G-deleted rabies virus (SADΔG-XFP(EnvA)) to infect these cells and to transsynaptically label their direct, presynaptic inputs. Furthermore, we tested the reliability of the experimental strategy and robustness of cell labeling of proximal and distal inputs of varying cell type.

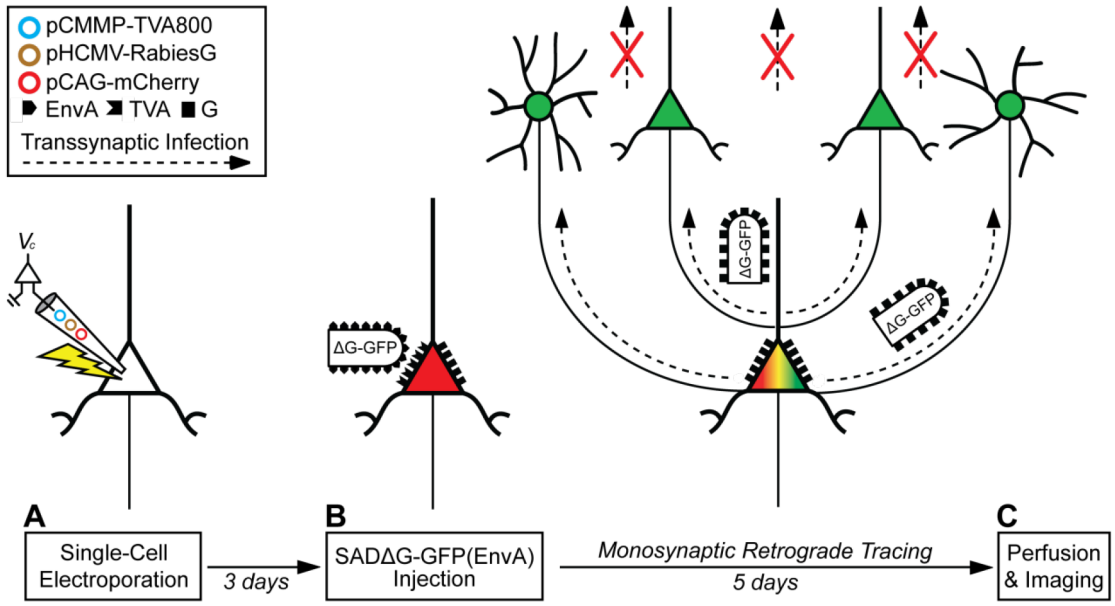

Figure 3.1 | Single Cell Tracing Strategy
(A) A single neuron is electroporated with plasmids (colored circles) coding for a fluorescent marker (e.g., pCAG-mCherry), the TVA receptor (pCMMP-TVA800), and the rabies glycoprotein (pHCMV-RabiesG).
(B) After 1-3 days, SADΔG-XFP(EnvA) virus is applied to the tissue, and infects only the electroporated neuron, since no other cells express the EnvA receptor, TVA (red indicates electroporated marker expression; black symbols, TVA and rabies glycoprotein (G)). As the virus replicates in the host neuron, it expresses XFP from the rabies genome, labeling the neuron (green in (C); merge yellow with electroporated marker).
(C) After 3-6 days, the tissue is fixed with paraformaldehyde after time has elapsed for transsynaptic infection (dotted arrow) and expression of the rabies virus and the tissue is visualized with fluorescence microscopy. The virus only transsynaptically infects and labels direct monosynaptic, presynaptic inputs (green) to the original host neuron, and not secondary connections (red crosses) because rabies glycoprotein, which is necessary for transsynaptic spread, is expressed only in the electroporated neuron. The schematic shows the timeline and gene constructs used for the experiment in Fig. 3.4.

Results

Tracing monosynaptic inputs to single neurons in cortical slice culture

We established the single cell tracing strategy *in vitro* by first targeting several

neurons for single cell electroporation in each cortical brain slice culture. A 10-12 MΩ patch pipette containing intracellular solution and plasmid DNA (pCMMP-TVA800 [75-150 ng/µl], pHCMV-RabiesG [50-100 ng/µl] and pCAG-venusYFP [50-100 ng/µl]) was advanced toward a cell body with a small amount of positive pressure applied until the resistance of the electrode increased by 20-30%. At this point, the pressure on the pipette was released and electroporation pulses were delivered with the following parameters: -10 to -12 V square 0.5-1 ms pulses at 100 Hz for 1 s. The single cell electroporation parameters used here were adapted from a combination of parameters used previously for single cell electroporation of plasmid DNA, using a novel set of plasmids (Kitamura et al., 2008; Rae and Levis, 2002; Rathenberg et al., 2003). The pipette was withdrawn and exchanged if necessary, and another cell was targeted for electroporation. Slices were incubated for 24-48 hours after electroporation in order to allow time for gene expression. Then, 200 µl/well of SADΔG-mCherry(EnvA) was applied to the brain slices. The slices were further incubated for 3 to 6 days to permit retrograde labeling by the virus, and then were fixed in 4% paraformaldehyde in phosphate buffer, antibody stained to increase fluorescent signal and mounted on glass slides (See Experimental Procedures).

Visualized under epifluorescence microscopy, several slices contained 1-13 neurons labeled with YFP from the electroporation transfection. In most of these cases, these neurons also expressed mCherry from the rabies genome, and a dense cluster of mCherry expressing neurons surrounded each electroporated neuron (Fig. 3.2A and 2B). The morphology of the traced neurons was labeled in great detail, as can

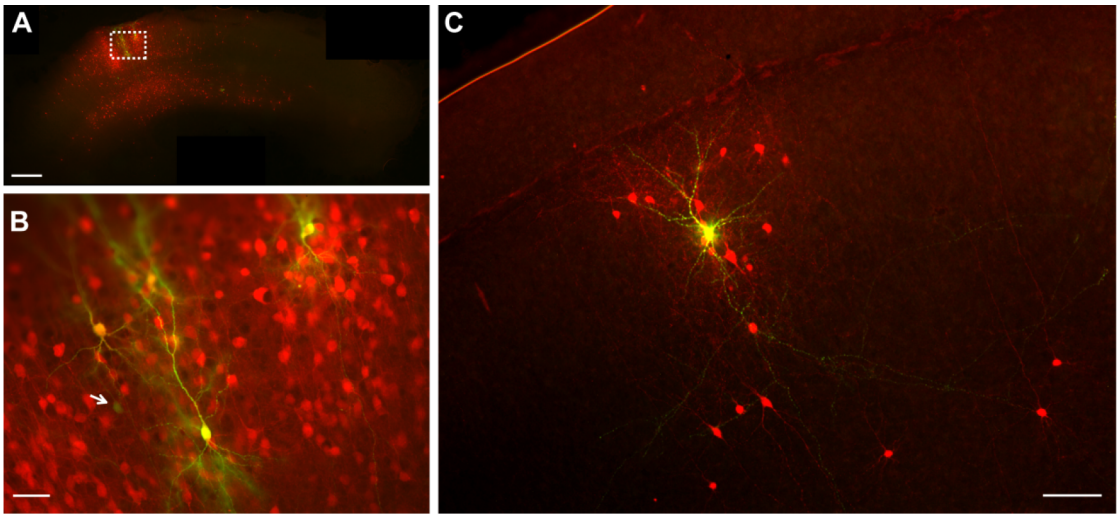

Figure 3.2 | Tracing the Monosynaptic Inputs to Single Neurons in Rat Cortical Slice Culture
(A) Twenty-one neurons were electroporated one by one with plasmids encoding venusYFP, TVA and rabies glycoprotein in a single slice. Two days later, SADΔG-mCherry(EnvA) was applied to the slice. After an additional six days, the slice was fixed in paraformaldehyde. Thirteen neurons expressed venusYFP from the electroporation transfection (green or yellow), and 8 neurons were confirmed to show co-expression of both the electroporated and rabies markers (yellow). Approximately 1000 neurons were infected transsynaptically by the virus and expressed mCherry (red).
(B) Higher magnification of box in (A) showing 5 out of the 13 transfected neurons (green or yellow) surrounded by a dense cluster of mCherry expressing neurons (red). Four of these five neurons also showed mCherry expression (yellow). One neuron (white arrow, green) showed low expression of venusYFP and did not show expression of mCherry.
(C) A different slice in which only one neuron (yellow) was electroporated with plasmids encoding venusYFP, TVA and rabies glycoprotein in a single slice. Two days later, SADΔG-mCherry(EnvA) was applied directly to the slice. After four additional days, the slice was fixed in paraformaldehyde. The electroporated neuron expressed both venusYFP (green) and mCherry (red) indicating successful transfection and virus infection (merged = yellow). Dozens of neurons were infected transsynaptically by the virus and expressed mCherry, displayed in red (n = 36; some not shown here, see supplementary Fig. 3.S1 which shows more transsynaptically labeled neurons and the extent of axonal labeling of the same electroporated neuron). Scale bars: 500 µm in (A), 50 µm in (B), 100 µm in (C).

be seen in the higher magnification image in Fig. 3.2B. These results are qualitatively similar to previous results demonstrating the monosynaptic tracing strategy in cortical

brain slice culture using biolistics transfection of a sparse population of neurons in each slice (Wickersham et al., 2007b). Unlike the previous report which could not reliably target just one neuron, using single cell electroporation made it possible to target a single neuron in a slice by electroporating only one cell per slice followed by applying the modified rabies virus 2 days later (Fig. 3.2C). The ability to target a single neuron for transsynaptic, retrograde labeling provides a way to unambiguously determine the direct inputs to a single neuron. This is in contrast to the previous report which required a second method to confirm connectivity between labeled neurons (e.g., paired recordings), since it was unclear which of the multiple biolistics transfected neurons was the postsynaptic partner for each transsynaptically labeled neuron. The labeling from electroporation was sufficient to follow the axons of electroporated neurons for several hundreds of microns across the slice, and the virus labeled presynaptic neurons up to several hundreds of microns away from the host neuron (Fig. 3.S1). Overall, the transfection rate of single cell electroporation for these experiments, determined by the expression of YFP in the fixed tissue was 18.5% (22/119). Of these successfully transfected 22 neurons, 14 also expressed mCherry (64%) indicating viral infection, and transsynaptic spread occurred in all slices that contained dual labeled neurons. The remaining neurons that expressed YFP but did not express mCherry tended to show dimmer YFP fluorescence than the dual labeled neurons (e.g. white arrow in Fig. 3.2B), suggesting that lower expression of the gene constructs, including TVA, might have reduced the probability of infection by SADΔG-mCherry(EnvA). Slices that showed no expression of the electroporation constructs had no expression of mCherry from the rabies genome in any cells (n = 16

slices, data not shown) further supporting previously published evidence that EnvA pseudotyped virus does not infect cells in the absence of TVA (Lewis et al., 2001; Wickersham et al., 2007b).

These results show that the infection and monosynaptic retrograde spread of the EnvA pseudotyped, G-deleted rabies virus can be targeted to a single neuron in a cultured brain slice. Tracing the inputs to a single neuron using single cell electroporation in a slice provides a standalone method to identify monosynaptic inputs to a single neuron, and removes the ambiguity present in other methods that transfect a population of neurons with TVA and thus cannot distinguish connectivity relationships at the single cell level. The optimal single cell tracing parameters determined in culture were used to help establish an efficient strategy for targeting the inputs to a single neuron *in vivo*, described below.

Tracing monosynaptic inputs to single neurons *in vivo*

To trace monosynaptic inputs to a single neuron *in vivo*, we used the 'shadow patching' technique visualized under two-photon microscopy (Kitamura et al., 2008), to target a single neuron for electroporation with a patch pipette in each anesthetized C57 BL/6 mouse (Fig. 3.3 and Movie S1; see Supplemental Experimental Procedures for animal care). Importantly, only one neuron was electroporated in each animal for tracing experiments. A 10-12 MΩ patch pipette was filled with intracellular solution, 50 μM of Alexa Fluor 488 or 594 dye, and 450 ng/μl of plasmid DNA (either 450 ng/μl of pCAG-YTB, a single plasmid expressing the 3 genes: venusYFP, TVA and RabiesG, or 150 ng/μl of each of the following plasmids: pCMMP-TVA800,

pHCMV-RabiesG, and either pCAG-mCherry or pCAG-venusYFP, see Experimental Procedures). The pipette was advanced in the brain until the tip reached layer 2/3 of primary visual cortex (V1), and positive pressure was applied to the back of the pipette to fill the extracellular space with dye. Given that the dye is not actively taken up by neurons and instead accumulates in the extracellular space, the cells appeared as dark shadows on a bright background in the thin optical slice (Fig. 3.3B and Movie S1) (Kitamura et al., 2008; Nevian and Helmchen, 2007). A cell with large round cell body morphology (i.e., likely pyramidal neuron) was selected near the location of the tip. The pipette was advanced toward the cell under visual control until the resistance of the electrode increased by 20-30% (e.g. a total resistance of 13 MΩ for a 10 MΩ pipette), the 20 mmHg of pressure maintained on the pipette was released and the electroporation pulses were delivered (-12 V square wave 500 μs pulses delivered at 50 or 100 Hz for 1 s (Judkewitz et al., 2009; Kitamura et al., 2008)). Electroporation success was verified by immediate filling of the soma with Alexa dye (Fig. 3.3B_3 and Movie S1). The pipette was withdrawn promptly with special care not to disturb the cell's membrane. The location of the cell was documented, in some cases the brain was covered with a silicone elastomer (Kwik-Cast), and the animal was recovered. One to three days later, the animal was re-anesthetized and 0.9-1 μl of concentrated SADΔG-EGFP(EnvA) or SADΔG-mCherry(EnvA) was injected at least 200 μm lateral to the location of the electroporated cell at a depth of approximately 250 μm below the dura to optimize infection probability and cell viability. The virus used in each experiment expressed a fluorescent marker that complemented the color of the marker expressed from electroporation in order to uniquely label the postsynaptic

neuron and its presynaptic inputs. The brain was covered with Kwik-Cast in some cases and the animal was recovered. Five days later, or 15 days later in one experiment, the animal was perfused with 4% paraformaldehyde in phosphate buffer, the brain sectioned at 40 µm sagittal sections and processed for histological analysis (See Experimental Procedures).

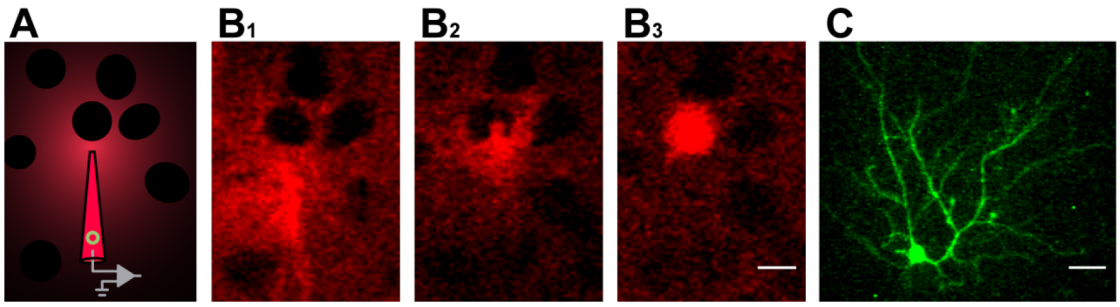

Figure 3.3 | *In Vivo* Single Cell Electroporation Visualized by Two-Photon Imaging
(A) Schematic of shadow imaging using a pipette containing Alexa dye and plasmid DNA (green circle) in intracellular solution. Positive pressure applied to the back of the pipette fills the extracellular space with fluorescent dye but does not fill neurons; they appear as dark shadows in the negative image.
(B_1) *In vivo* two-photon fluorescent images of a pipette containing pCAG-YTB and Alexa dye in intracellular solution approaching a neuron, and dimpling its membrane in (B_2).
(B_3) The neuron filled with Alexa 594 dye immediately after electroporation (See also Movie S1).
(C) An average z-projection of the same neuron imaged under two-photon microscopy *in vivo* five days later. The neuron is green due to expression of venusYFP from the electroporated pCAG-YTB plasmid. Scale bars are 15 µm in (B_1), (B_2), and (B_3) (same scale) and 25 µm in (C).

To assess the success of each experiment, the entire hemisphere in which the cell was electroporated was systematically scanned for fluorescent cells indicating viral infection or transfection by electroporation. In all cases in which a neuron was successfully electroporated and infected by the pseudotyped rabies virus (n = 6),

dozens to nearly 100 other neurons were transsynaptically labeled by the virus (mean = 48.7, range from 14 to 97), the majority of which formed a cluster surrounding the electroporated neuron (Fig. 3.4 and S2). The most neurons were labeled transsynaptically by the rabies virus when injections were made 3 days after electroporation (n = 3), and the least were observed with a 1 day time interval (n = 1). When electroporation was unsuccessful (n = 8), no neurons were found expressing the fluorescent protein from the rabies genome indicating that there was not any nonspecific infection of the EnvA pseudotyped virus in the absence of TVA. This provides further evidence for the specificity of the EnvA-TVA interaction, and suggests that all of the neurons expressing the fluorescent marker from the rabies genome in these experiments were either directly infected via the EnvA-TVA interaction (electroporated neurons) or infected transsynaptically via rabies glycoprotein complementation of the G-deleted rabies virus in the electroporated neurons. Overall, transsynaptic labeling of inputs to single neurons was achieved in just over one third of all electroporation attempts (6 successes and 11 failures in 17 attempts). When attempts were unsuccessful it was usually due to failure of electroporation transfection (8/17), and sometimes due to failure to infect the electroporated neuron (3/17).

The intricate morphology of labeled neurons was clearly visible in all cases, including details such as dendritic spines and axons (Fig. 3.4B, 4C, 4E, 4G and S2D). This labeling made it possible to classify the cell type of labeled neurons based on morphology, and to omit any labeled glial cells from the analysis (3/6 experiments contained glial cells labeled by the rabies virus near the injection site constituting

10.4% (34/326) of all rabies labeled cells). The mechanism of glial labeling in these experiments is unknown. Several transsynaptically labeled visual-cortical pyramidal neurons were found, locally in layer 2/3 (Fig. 3.4A, 4B and S2A), and in deeper cortical layers more distally (Fig. 3.4A, 4C, 4G, S2A and S2D). It was possible to characterize 22 neurons as putative excitatory neurons labeled transsynaptically by the virus from the host neuron in Fig. 3.4A, based purely on the obvious presence of spiny dendrites. The remaining 75 neurons labeled transsynaptically in this experiment did not clearly show spiny dendrites and the majority of these neurons are likely to represent a diverse interneuron population, including cells with multipolar (Fig. 3.4D) and bipolar (Fig. 3.S2C) morphologies. Many neurons were found at distances of over 200 μm lateral to the host neuron. For example, at least 18.6% (18/97) of all labeled neurons had cell bodies located greater than 200 μm lateral to the host neuron in Fig. 3.4A (white boxes in Fig. 3.4A and 4C-4G). This included connections that were detected and intricately labeled by the single cell tracing strategy at distances of up to over a centimeter away from the host neuron in subcortical structures such as the hypothalamus (Fig. 3.4F) and thalamus (Fig. 3.S2E). Given that a typical cortical brain slice used for electrophysiology experiments is 300-400 μm thick and does not typically include subcortical structures, these connections would have been entirely missed by *in vitro* analyses since they would be cut during preparation. The fact that neurons at great distances from the host neuron could be labeled by the rabies virus in such detail exemplifies the ability of the rabies virus to replicate and amplify gene expression in presynaptic neurons.

Figure 3.4 | Tracing the Monosynaptic Inputs to a Single Mammalian Neuron *In Vivo*

(A) A single layer 2/3 neuron (yellow neuron indicated by white arrow) in mouse visual cortex was targeted for the single cell tracing strategy using the parameters and reagents schematically represented in Fig. 3.1. Transfection of electroporated plasmids was confirmed by expression of mCherry in the neuron (inset) and by infection of the neuron by SADΔG-EGFP(EnvA), and glycoprotein mediated transsynaptic spread of rabies virus to presynaptic neurons, where the virus expressed EGFP (green). A cluster of a variety of interneuron cell types and pyramidal cells was found surrounding the electroporated neuron shown in (A) and extending onto adjacent 40 μm sections (for example (B), some sections not shown). Many other neurons were also found throughout the brain, located several hundred microns to over a centimeter away from the host neuron (C-G). Regardless of distance from the host neuron, the morphology of neurons was labeled in intricate detail, and it was possible to characterize the cell type of labeled neurons based on morphology. A total of 97 neurons were labeled transsynaptically by the virus in this experiment. All panels in this figure are from the same animal. Blue is NeuN staining of neuronal nuclei.

(B) Adjacent medial section to (A). Dendrites from the electroporated neuron (yellow) can be seen extending onto this section, as well as the neuron's descending axon (indicated by white arrow).

(C) Higher magnification image of the pyramidal neuron indicated by the lower white box in (A). This neuron was located over 400 μm caudal to the host neuron, in the same lateral-medial plane. The detailed morphology of the neuron is clearly visible, with complete filling of the neuron's dendritic spines and axon. This image only shows a small fraction of the elaboration of the neuron's processes. Some of these features are visible in (B, similar location to in (A)).

(D) Higher magnification image of the interneuron indicated by the upper white box in (A). This neuron was located over 200 μm caudal to the host neuron, in the same lateral-medial plane. The complete filling of the neuron's dendritic tree permitted characterization of the neuron as a layer 2/3 multipolar inhibitory neuron (more dendrites visible in (B)). Dozens of other interneurons were found in this experiment, representing a variety of cell types.

(E) A projection neuron found several hundred microns away from the host neuron in retrosplenial cortex.

(F) A neuron transsynaptically labeled in hypothalamus. Despite the over 1 cm distance from the host neuron, the brightness of label in this cell was comparable to the other neurons labeled throughout the brain.

(G) A visual cortical projection neuron labeled in complete detail, located over 200 μm lateral to the host neuron. Scale bars: 100 μm in (A), (B), 25 μm inset in (A) and (C)-(G).

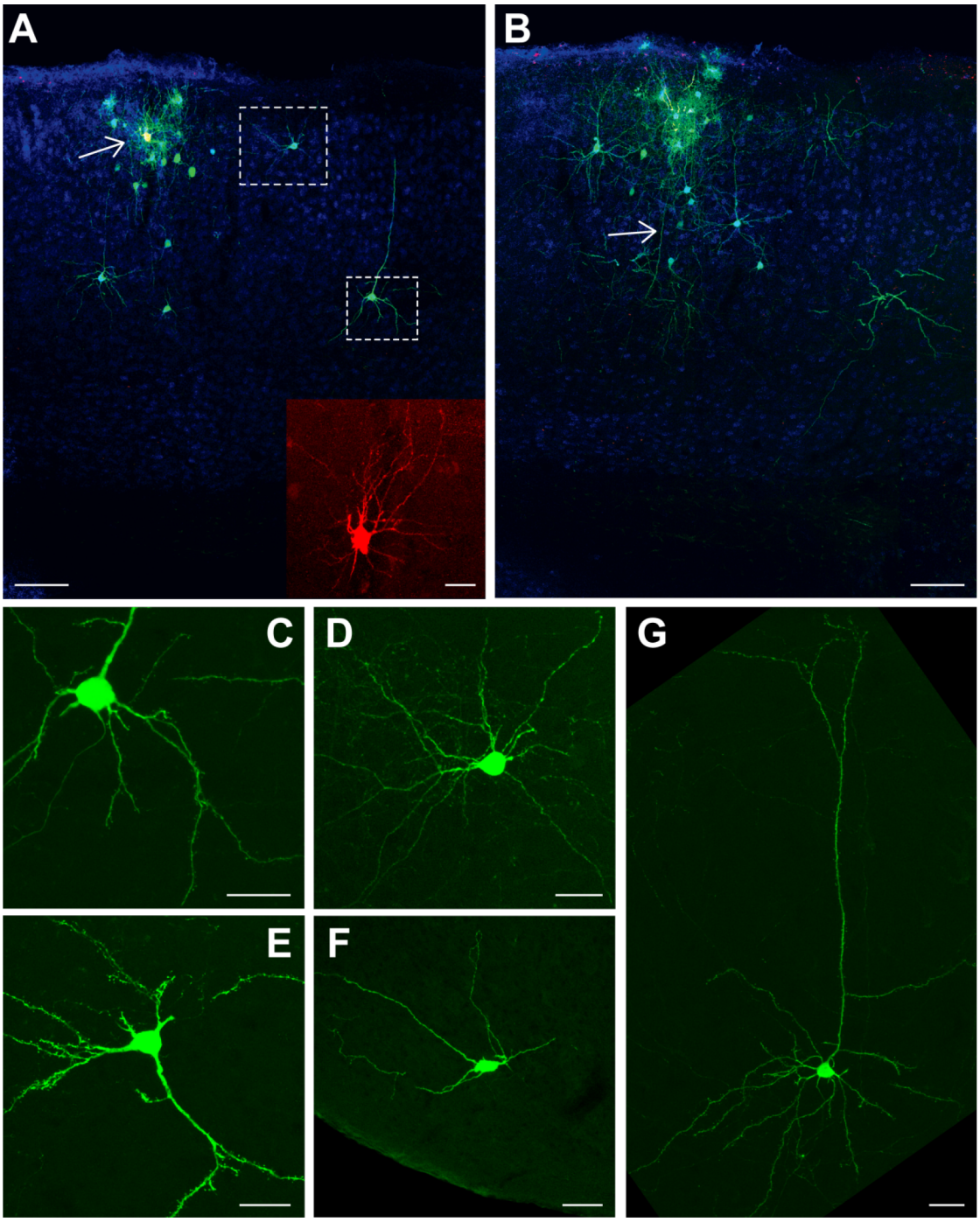
A
B
C
D
G
E
F

These results demonstrate the ability to reliably and intricately label monosynaptic inputs to a single neuron *in vivo*, and target a single postsynaptic neuron and its presynaptic neuronal network for independent gene expression.

Discussion

In the present study, we developed and implemented a novel technique for robust and reliable targeting of single neuronal networks *in vitro* and *in vivo*. In every case in which a neuron was electroporated and infected with pseudotyped rabies virus there was successful transsynaptic labeling of the direct inputs to that cell. This led to an overall success rate of more than one third of *in vivo* attempts. For the first time, it is possible to identify and probe a single microcircuit *in vivo*, differentiating it from the vast web of connections that comprise the intact brain. We demonstrated the utility of the technique by targeting single layer 2/3 pyramidal neurons in mouse neocortex for infection and monosynaptic, retrograde spread of a modified rabies virus in order to reveal direct proximal and distal inputs from throughout the intact brain, *in vivo.* Combining single cell electroporation with a genetically modifiable, monosynaptic tracing rabies virus targets a single neuron and its direct inputs for independent gene control, paving the way for functional and genetic dissection of circuit development and information processing with single cell resolution at the molecular-genetic level.

Comparison to *in vitro* methods

The results presented here demonstrate the ability to target at least dozens of inputs to a single neuron for gene expression and fluorescent labeling both *in vitro* and *in vivo*. This offers a far higher yield for determining connectivity of neurons than multiunit recordings in brain slices, even when correlation analyses are used to predict likely connections (Aaron and Yuste, 2006; Kozloski et al., 2001; Peterlin et al., 2000), and provides independent gene control of connected neurons. Furthermore, when applied *in vivo*, distal and potentially rare connections can be identified that would otherwise be severed or missed by slice recording experiments. Moreover, the *in vivo* single cell tracing strategy may provide a means to probe the function of single neuronal microcircuits with single cell resolution and genetic control in the intact animal. This should make it possible to probe single neuronal networks *in vivo* in relation to ongoing sensory information and behavior.

The single cell tracing strategy could also be used to improve the throughput of *in vitro* paired recording studies by labeling the inputs to a single neuron in slice culture to guide recordings of connected neurons, in a more precise way than what was shown previously (Wickersham et al., 2007b). A similar goal could be achieved by making acute slices from an animal in which the inputs to a single neuron were labeled *in vivo*. In this case, functional tuning properties of labeled neurons could be determined in the living animal and then related to functional connectivity information gained from paired recordings of the same neurons in acute slices made from the same animal. However, these studies would be limited to pairs that maintained their

connection during slicing, despite the fact that many of the connections between neurons would likely be severed during slicing (Stepanyants et al., 2009).

Application to fine scale circuit anatomy

Given high levels of fluorescent gene expression from single cell electroporation transfection and rabies infection, in addition to the ability to amplify labeling using specific antibodies, the detailed morphology of each neuron within a microcircuit is labeled by the single cell tracing technique. This makes it possible to determine the location and characterize the cell type of labeled neurons by morphological analysis in addition to other histological analyses, such as antibody stains to distinguish different interneuron types (Kawaguchi and Kondo, 2002). Determining the detailed cell morphology and cell-type specific connectivity pattern of single neuronal networks will add crucial details to realistic models of circuit computation and help reveal information processing mechanisms used by single neurons and microcircuits *in vivo*. To aid these analyses, the single cell tracing strategy could be applied in *Brainbow* transgenic mice (Livet et al., 2007) using a rabies virus expressing Cre recombinase (unpublished observations, T.M. and E.M.C.) so as to label each neuron in the circuit with a unique color. This may help distinguish the dendritic and axonal processes of each neuron in the circuit and provide a way to predict the precise subcellular location of synapses on the postsynaptic neuron from uniquely colored presynaptic neurons, yielding even greater fine scale details about the pattern of connectivity within a single neuronal network (also see Petreanu et al., 2009). Comparing detailed connectivity patterns revealed by the single cell tracing

strategy within and across neuronal classes will help determine whether a basic pattern of microcircuitry exists across different brain areas (Douglas et al., 2003; Douglas and Martin, 2004; Silberberg et al., 2005; Thomson and Bannister, 2003). In this way, it will help evaluate the extent to which the billions of neurons that comprise the brain can be meaningfully characterized into one of potentially thousands of neuronal cell types based on connectivity, and how well we can extrapolate knowledge gained from studying single neurons and microcircuits to understanding circuit organization and function throughout different brain regions.

These analyses will be improved by the ability to label a greater fraction of the inputs to a single neuron (Crick, 1979). It is likely that the data presented here are an underestimate of the number of neurons providing input to a single layer 2/3 pyramidal neuron. The total number of neurons that provide input to a single layer 2/3 pyramidal neuron could be estimated by dividing the total number of synapses a single layer 2/3 pyramidal neuron receives by the number of synapses formed between each pair of connected neurons. The literature provides estimates of these numbers for a limited set of neurons, cortical areas and species. Furthermore, several assumptions have been made in these studies, such as extrapolating across age, cell type, brain area, and/or species, and differences in methods of preparation and analysis lead to ambiguities, especially when comparing across studies. The estimates we perform below are guilty of these same caveats. We provide them here only to gain a sense of the potential range of the number of neurons that provide input to a single layer 2/3 pyramidal neuron in rodent visual cortex.

DeFelipe and Farinas, 1992 estimated that the total number of synapses a layer 2/3 pyramidal neuron in rat visual cortex receives is between 10,682 and 14,575, based primarily on spine count data, with corrections made for estimated proportions of synapses formed on dendritic shafts, and onto the same spine as another synapse. The primary data for this estimate are from Larkman, 1991, a study which used dye filling of neurons in acute slice preparations to label neurons for spine distribution analysis. As stated earlier, spine density has been shown to increase dramatically as a result of slice preparation compared to tissue fixed *in vivo* (Kirov et al., 1999). In hippocampal slices made from postnatal day 21 rats, an age likely to be similar to the age used in the Larkman study, this increase was 90%. Using this increase as an estimate for the increase in spine density induced in the Larkman, 1991 data results in 5,662 to 7,671 estimated synaptic contacts. Interestingly, this correction almost entirely accounts for the difference in spine density of layer 2/3 pyramidal neurons between the Larkman, 1991 study and an earlier study of layer 2/3 pyramidal neurons fixed *in vivo* (Peters and Kaiserman-Abramof, 1970). For further comparison, Schüz and Palm, 1989 estimated that the average number of synapses per neuron is between 6,700 and 7,000 in area 17 of the mouse based on electron microscopy data and volume estimates, although this study did not take into account differences based on cell type.

The above estimates do not account for the number of synapses a presynaptic neuron makes on a postsynaptic neuron. An explicit estimate of the number of neurons that provide input to a layer 2/3 pyramidal neuron in rodent visual cortex could be calculated by dividing the total number of synapses by the number provided

by each connected pair. The best estimates of cortico-cortical connection number are limited to select pairs of neurons, but consistently report approximately 4-5 synapses between a single pre and a single postsynaptic neuron by both anatomically and functionally constrained analyses (Feldmeyer et al., 2002; Markram et al., 1997; Silver et al., 2003; Stepanyants and Chklovskii, 2005; Tamás et al., 2004; Wang et al., 2006). Further studies are necessary to determine how these numbers compare to connections between different types of neurons. Using 4-5 synapses per connected pair results in an estimate of 1,132 to 1,918 neurons that provide input to a single layer 2/3 pyramidal neuron. With respect to age, spine elimination between the assumed time point used for the Larkman, 1991 study (roughly one month old), and the age range used in the current study (2-3 months old), has been shown to be approximately 25% in mouse visual cortex, of pyramidal dendrites in superficial layers (Grutzendler et al., 2002). Applying this factor to be directly proportional to the number of total inputs eliminated leads to an estimate of 849 to 1,439 neurons providing input to a single layer 2/3 pyramidal neuron. Thus, even with all the assumptions and caveats of these estimates used to predict the number of inputs to a single neuron, it is probable that the majority of inputs to the single neurons studied here were not transsynaptically labeled with rabies virus.

The present study is the first of its kind to evaluate the spread of rabies virus from a single neuron and thus no previous estimates exist to compare the efficiency of spread of rabies from single neurons in the single cell tracing strategy to the natural spread of wild-type rabies. The result that the most neurons were labeled transsynaptically by the virus in the experiments with the longest time interval

between electroporation and virus injection supports the hypothesis that the timing and expression levels of rabies glycoprotein are key factors in the efficiency of spread of the virus to presynaptic neurons. It is likely that the exogenous introduction of the rabies glycoprotein by electroporation of plasmid DNA does not reliably mimic the precise timing and expression levels of the gene from the wild-type rabies genome. The life-cycle of rabies virus is tightly self-regulated, as has been demonstrated by extremely low recovery rates of rabies virus from cDNA (Schnell et al., 1994). Rabies virus budding efficiency has also been shown to increase by up to 30 fold in culture in the presence versus absence of glycoprotein, indicating a role for the glycoprotein in virus budding efficiency (Mebatsion et al., 1996a). Furthermore, rabies virus particles are only infectious when they are studded with glycoprotein (Etessami et al., 2000; Wickersham et al., 2007b). More precisely controlling the expression of rabies glycoprotein in the targeted neuron may lead to more efficient viral budding and transsynaptic infection. Modulating endogenous regulatory gene expression mechanisms within the rabies virus (i.e., mutations of the M protein to facilitate increased mRNA nuclear export (Faria et al., 2005)), or utilizing conditional gene expression systems to more tightly control the expression pattern of glycoprotein (Banaszynski et al., 2008; Gossen and Bujard, 2002), in future studies may yield more efficient transsynaptic spread of the virus from the electroporated neuron. These approaches may be further facilitated once more is known about the precise pattern of expression of rabies virus proteins over fine time scales, and about the mechanisms underlying the glycoprotein-mediated transsynaptic spread of the virus. Additional studies investigating the distribution of inputs onto the postsynaptic neuron analyzed

by electron microscopy may yield fundamental details about the number of inputs labeled by the single cell tracing strategy as a function of cell type and dendritic target domain, as well as the fraction of total synapses labeled by the virus and additional details about the types of synapses labeled and at what rate of efficiency. A combination of improvements of the efficiency of spread of the virus, and additional analyses such as the electron microscopy studies suggested above, may yield an increasingly complete anatomical description of each single targeted neuronal network.

Targeting single neuronal networks for gene expression

To facilitate genetic studies of circuit development and function, the two mechanisms of genetic manipulation provided by the single cell tracing strategy can be utilized. Genes of interest can be included in either the single cell electroporation transfection or in the transsynaptic tracing rabies virus genome (Judkewitz et al., 2009; Wickersham et al., 2007a). In this way, independent gene control of the postsynaptic neuron alone or of the entire targeted microcircuit is possible. By adapting conditional gene expression systems, it should also be possible to target the presynaptic neuron population independently from the postsynaptic neuron. The ability to target a single microcircuit, or some combination of its circuit elements, for genetic manipulation opens the possibility to precisely probe and manipulate neuronal function using genetically encoded activity sensors and modulators (e.g., ChR2, genetically encoded calcium indicators (GECIs), and allatostatin receptor (AlstR), see Luo et al., 2008 for a review), and determine the role of specific genes in circuit development (e.g., specific

transcription factors) or information processing (e.g., specific ion channels). By simultaneously measuring the activity of the postsynaptic neuron, while precisely modulating spiking activity of specific presynaptic neurons, or expression of specific genes in the pre or postsynaptic neuron, it should be possible to determine cause-effect relationships between presynaptic activity and/or specific gene expression, and the output activity of the postsynaptic neuron.

Studying information processing by single neuronal networks *in vivo*

Perhaps the most significant contribution the single cell tracing strategy will make to neuroscience will be in its application to probing the function of single neuronal networks, with single cell resolution and molecular precision *in vivo*. Future studies will be necessary to combine the single cell tracing strategy with functional assays of neuronal activity. However, previous evidence suggests that these applications of the tracing technique will be possible and may provide unprecedented access to the function of single neuronal networks *in vivo*.

It has been shown that single neurons transfected by single cell electroporation, or infected by G-deleted rabies virus, *in vivo* can be recorded from using standard electrophysiology techniques several days or up to weeks later. Furthermore, these neurons show normal physiological properties (Judkewitz et al., 2009; Kitamura et al., 2008; Wickersham et al., 2007a; Wickersham et al., 2007b). In the single cell tracing strategy, since the postsynaptic neuron is labeled by a different fluorescent protein than its presynaptic inputs, it should be possible to target patch recordings to either a postsynaptic neuron or a presynaptic neuron, or potentially both simultaneously, using

targeted patch recordings *in vivo* (Judkewitz et al., 2009; Kitamura et al., 2008; Margrie et al., 2003; Poulet and Petersen, 2008). These recordings could be used to determine the functional influence (i.e., synaptic strength) of presynaptic neurons on the postsynaptic neuron, or to measure the tuning properties of connected neurons in relation to specific types of information. To achieve a similar goal, optical sensors of neuronal activity, such as calcium sensitive dyes (Ohki et al., 2005), could be used to simultaneously characterize the function of a large population of connected neurons labeled by the single cell tracing strategy, compared to unlabeled neighboring neurons *in vivo*. For example, this strategy could be used in the visual system to investigate whether neurons with similar visual tuning properties are connected. Comparing the activity of connected neurons may inform models of the integration a neuron performs on its specific inputs in time to generate its own unique firing pattern, and help answer many longstanding questions about how information is conveyed and processed throughout a neuronal network.

These applications of the single cell tracing strategy, in addition to the functional, anatomical and genetic applications discussed and validated in the above sections, provide a framework for direct analysis of the fine scale structure and function of single neuronal networks in the living brain. This level of identification, analysis and control of single neuronal networks has not been possible until now, especially *in vivo*, and may greatly improve our understanding of the mechanisms underlying microcircuit structure, development and computation throughout the intact, functioning brain.

Conclusion

A central hypothesis guiding neuroscience research is that the brain processes information through the combined computation of billions of single neurons organized into precisely connected neuronal networks. In this view, a single neuron is the brain's most basic computational unit; it transforms its specific inputs in time to generate its unique, discrete output, similarly influencing the output response of postsynaptic neurons. Surviving the lifetime of the organism, a neuron relies on adaptable protein expression patterns (e.g., ion channels), morphological features (e.g., shape of dendrites and dendritic spines) and other intrinsic properties to dynamically filter its specific inputs to determine its output firing pattern. This computation occurs continuously over time for every neuron, and it is through the combined information processing of single neurons organized into ever increasingly large and overlapping neuronal networks that the brain performs the diverse and complex computations that determine perception, cognition and behavior. Unraveling this inapproachably complex process requires a dramatic simplification of the problem. Here, we developed and implemented a robust and reliable method to target a single neuronal microcircuit *in vivo* for fine scale anatomical and genetic analyses. Applying the technique, we identified monosynaptic inputs to single neocortical pyramidal neurons from across the living mouse brain, isolating them from the millions of connections that surrounded them. We also demonstrated the ability to target cellular components of a single microcircuit for expression of genes of interest. Combining the power of anatomical tracing with genetic manipulation and existing assays of neuronal function, it should be possible to gain greater insights into the mechanisms supporting

information processing by single neuronal networks and determine the link between connectivity and function of single neurons throughout the brain.

Methods

Brain Slice Culture

All experiments involving living animals were approved by the Salk Institute's Institutional Animal Care and Use Committee. Cortical brain slices were prepared from 5-7 day old rats and incubated at 37º for 2 days before electroporation, as described previously for ferrets (Dantzker and Callaway, 1998). On the day of electroporation, slices were individually transferred from a CO_2 incubator to a slice physiology rig and submerged in culture medium. The experiment was limited in time so that each slice was transferred back to the incubator within ~30 minutes. In some experiments, multiple cells were electroporated per slice to test the reliability of the experiment. In other experiments, a single cell was electroporated in each slice. The electroporation parameters were -10 to -12 V square pulses, 0.5-1 ms duration at 100 Hz for 1 sec, with an increase in resistance of a 10-12 MΩ pipette of 20-30% during patching, based on previous studies of single cell electroporation (Kitamura et al., 2008; Rae and Levis, 2002; Rathenberg et al., 2003). The pipette contained the following plasmids in standard intracellular solution: pCMMP-TVA800 [75-150 ng/µl], pHCMV-RabiesG [50-100 ng/µl] and pCAG-venusYFP [50-100 ng/µl]. After 1-2 days, 200 µL/well of modified rabies virus supernatant (see below) was applied to

the surface of the slices. The slices were incubated another 24 hours, and the culture medium was changed. The slices were fixed in 4% paraformaldehyde after 2-5 additional days. The tissue was antibody stained using antibodies against GFP (Aves Labs) and DsRed (Clontech), and secondarily stained to increase signal (Cy2, Jackson Immuno and Alexa Fluor 568, Invitrogen). Images were acquired on an epifluorescence microscope (Olympus).

In vivo Two-Photon Microscopy, Surgery, and Imaging Chamber

These procedures are described as Supplemental Experimental Procedures.

In Vivo Single Cell Electroporation

The *in vivo* single-cell electroporation protocol was adapted from previous studies (Judkewitz et al., 2009; Kitamura et al., 2008). The most relevant parameters are described here, and a more detailed protocol is available online (See Supplemental Experimental Procedures). For tracing experiments, only one neuron was electroporated in each animal. The artificial cerebrospinal fluid (ACSF) was removed from the imaging chamber and a pipette containing intracellular solution, Alexa Fluor 488 or 594 dye (50 μM, Invitrogen), and plasmid DNA (450 ng/μl total concentration of either pCAG-YTB or 150 ng/μl of each of the following plasmids: pCMMP-TVA800, pHCMV-RabiesG, and either pCAG-mCherry or pCAG-venusYFP), and was placed over the craniotomy within the microscope's field of view. The pipette was advanced through the dura while positive pressure pulses (>100 mmHg) were applied to the back of the pipette with a syringe until the pipette reached a depth of

175-225 μm below the pial surface of primary visual cortex (V1). Positive pressure was applied to the back of the pipette to fill the extracellular space with dye. The pipette location was optimized to approach a single cell with pyramidal cell body morphology. Once the pipette was in close proximity of the cell, the pressure was lowered to approximately 20 mmHg. The pipette was advanced toward the cell until the resistance increased by 20-30% of the electrode. The patch was also observed under two-photon microscopy and a small dimple in the cell membrane filled with dye was sometimes observed forming around the pipette tip (Fig. 3.3B_2 and Movie S1). At this point, the pressure was released on the pipette and the electroporation pulses were delivered. Fifty or 100 square wave voltage pulses were delivered at 50 or 100 Hz respectively with an Axoporator 800A (Molecular Probes). The pulses were 500 μs in duration and -12V in amplitude (Judkewitz et al., 2009; Kitamura et al., 2008). Electroporation success was verified by immediate filling of the cell body with dye. The pipette was then immediately retracted slowly following a 30° diagonal trajectory, as was the case during entry. The craniotomy was covered in some cases with Kwik-Cast silicone elastomer (WPI) and the incision was sutured. The animal was recovered on a water recirculating heating pad and returned to its housing.

Virus Production and Injection

For slice culture experiments, EnvA pseudotyped rabies virus was produced as previously described (Wickersham et al., 2007b). The virus was further concentrated for *in vivo* injections by ultracentrifugation following a protocol for lenti virus production (Tiscornia et al., 2006). A recent protocol was published that also

describes the ultracentrifugation steps as well as further details for production of high-titer EnvA pseudotyped rabies virus (Wickersham et al., 2010). Biological titers on TVA expressing cells were 5.1 X 10^8/ml and 7.7 or 9.4 X 10^7/ml for SADΔG-EGFP(EnvA) and SADΔG-mCherry(EnvA) respectively for *in vivo* injections.

One to three days after electroporation the animal was anesthetized and prepared for surgery, and placed in a small stereotaxic device. The silicone covering was removed and the brain rinsed with ACSF. The location of the cell was estimated using a sketch of the blood vessel pattern and landmarks as a reference. In some experiments, the same region was imaged with two-photon microscopy and the cell location was confirmed based on fluorescent gene expression, but this step was not necessary. A pipette with a 25-30 μm outer diameter tip, cut to a sharp angle, was lowered to directly penetrate the dura perpendicular to the brain surface at least 200 μm lateral to the estimated cell location in an area void of blood vessels and lowered to 250 μm below the pial surface. 0.9-1μl of virus was injected over 10-20 minutes, the pipette was left in place for 5-10 minutes and then the pipette was withdrawn. During injection, 5-10 ms pulses at 1.5 s intervals at 20 PSI or continuous pressure of approximately 0.5-1 PSI was applied to the back of the pipette with a Picospritzer (General Valve) or a syringe respectively. The brain was rinsed with ACSF, Kwik-Cast silicone elastomer was applied directly to the brain in some cases and the skin incision was sutured. The animal was recovered and returned to its housing.

Histology

Five days after viral injection, or 15 days later in one case, the animal was perfused with phosphate buffered saline followed by 4% paraformaldehyde in phosphate buffer. The brain was post-fixed overnight in 4% paraformaldehyde in phosphate buffer and then transferred to 30% sucrose in phosphate buffered saline overnight. The brain was sectioned on a freezing microtome at 40 μm thickness sagittally. The tissue was incubated in blocker solution for 2 hours and then incubated overnight at 4°C with antibodies against GFP (Aves Labs), DsRed (Clontech) and NeuN (Millipore) to amplify endogenous fluorescent gene expression and label neuronal nuclei. The tissue was washed and then incubated in secondary antibodies (Cy2, Rhodamine Red-X, AMCA, Jackson Immuno) for 2-3 hours at room temperature. The tissue sections were washed and then mounted on glass slides and coverslipped with PVA-DABCO. The entire hemisphere in which the experiment took place was scanned on an epifluorescence microscope for fluorescently labeled cells in experimental and control animals and the number of fluorescent neurons was quantified. In some cases, the contralateral hemisphere was also examined. Glial cells were sometimes observed near the injection site (Fig. 3.S2A), but these cells were excluded from the analysis based on morphology. Images were acquired on a confocal microscope (Leica) for *in vivo* data and displayed as maximum z projections, and multiple fields of view were integrated to form the montage images in Fig. 3.4A and 4B. Images were acquired on an epifluorescence microscope (Olympus) for *in vitro* data.

Supplementary Material

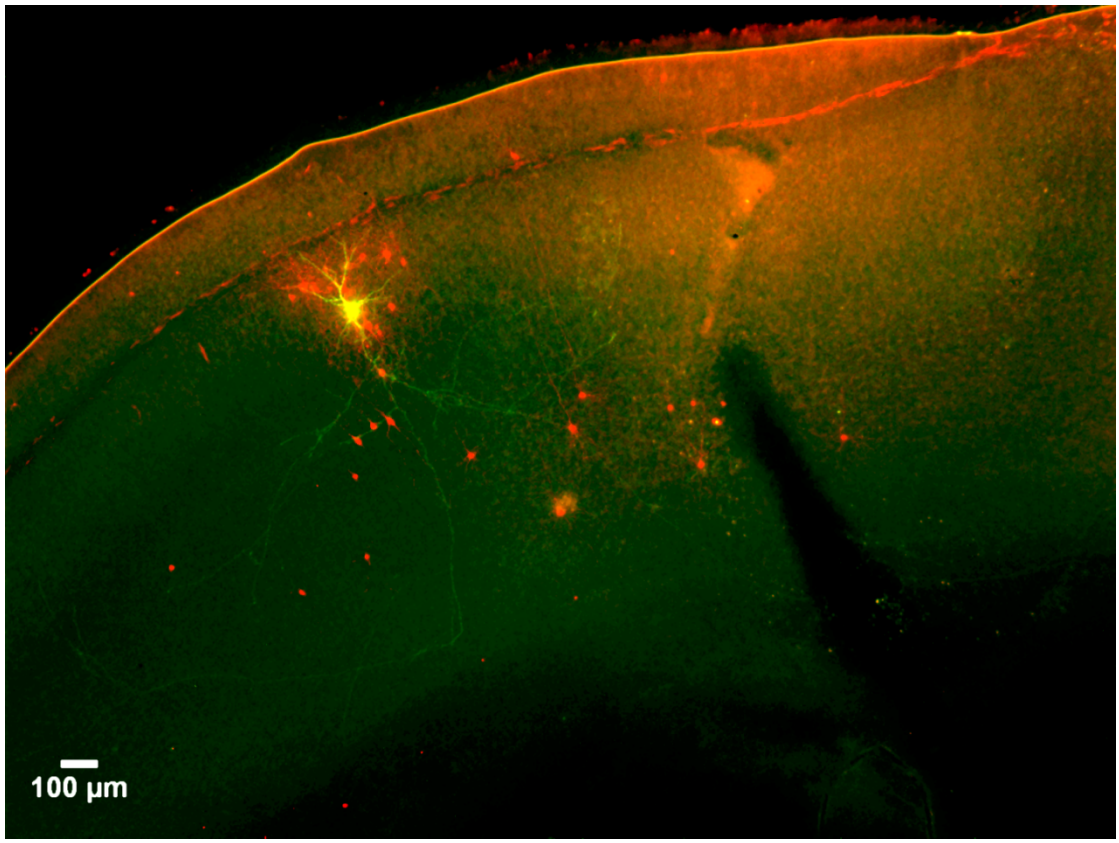

Figure S3.1. Single Cell Electroporation Labels the Fine Scale Structure of Axonal Projections
As described in Fig. 3.2C, a single neuron was electroporated with plasmids encoding TVA, rabies glycoprotein and venusYFP in a single cortical brain slice culture. Two days later, SADΔG-mCherry(EnvA) was applied to the slice and four days later the tissue was fixed in paraformaldehyde. Saturating the fluorescent signal from the cell body of the electroporated neuron (yellow) reveals the fine scale morphology of the neuron's axon, which extends for several hundred microns across the slice, and makes several branches throughout different cortical layers. This low magnification image also shows additional transsynaptically labeled, rabies infected neurons several hundred microns away from the host, electroporated neuron, located outside the field of view of Fig. 3.2C.

Figure S3.2. Tracing the Monosynaptic Inputs to a Single Cortical Pyramidal Neuron *In Vivo*, Using the pCAG-YTB Plasmid and SADΔG-mCherry(EnvA)

(A) A single layer 2/3 pyramidal neuron in mouse visual cortex was electroporated with pCAG-YTB. Three days later, SADΔG-mCherry(EnvA) was injected ~200 μm lateral to the location of the cell, and five days later the animal was perfused with paraformaldehyde and later the brain was sectioned at 40 μm thickness, in the sagittal plane. The electroporated neuron (indicated by white asterisk, green + red, merge yellow) was surrounded by several dozen transsynaptically labeled neurons (red) of varying cell type, from superficial and deep cortical layers (as well as subcortical structures as in (E)). Some of these neurons and the dendrites and axon (white arrows) extending from the electroporated neuron, can be seen on the adjacent 40 μm sections. From left to right, each panel is an adjacent 40 μm section in the medial direction. The detailed morphology of labeled neurons is clearly visible including the elaboration of the dendritic trees of each neuron and axonal projections (as further exemplified in (D)), revealing the presence of several distinct types of neurons including pyramidal neurons and a variety of interneurons from different cortical layers. A total of 83 neurons were labeled transsynaptically by the virus.

(B) Higher magnification of venusYFP expressed in electroporated neuron in A (indicated by white asterisk).

(C) A bipolar interneuron labeled with mCherry, transsynaptically by the virus.

(D) High magnification image of a visual cortical projection neuron transsynaptically labeled over 200 μm lateral to the host neuron. The extent of the labeling is comparable to the labeling of neurons more proximal to the electroporated, postsynaptic neuron (as shown in (A)). For example, dendritic spines are clearly visible, as well as the neuron's descending axon. Further elaboration of the neuron's dendrites and axon are visible on adjacent sections (not shown).

(E) A transsynaptically labeled mCherry-expressing neuron located in the lateral geniculate nucleus of the thalamus at two magnifications. Lower magnification image shows the neuron's location relative to landmarks such as the hippocampus (blue is NeuN staining). Inset shows a higher magnification image of the neuron, revealing the detailed morphology of its dendritic processes. Scale bars are 100 μm for all panels in (A) which are all at the same scale, 25 μm for (B), (C), (D) and inset in (E) and 200 μm for (E). All panels are from the same animal.

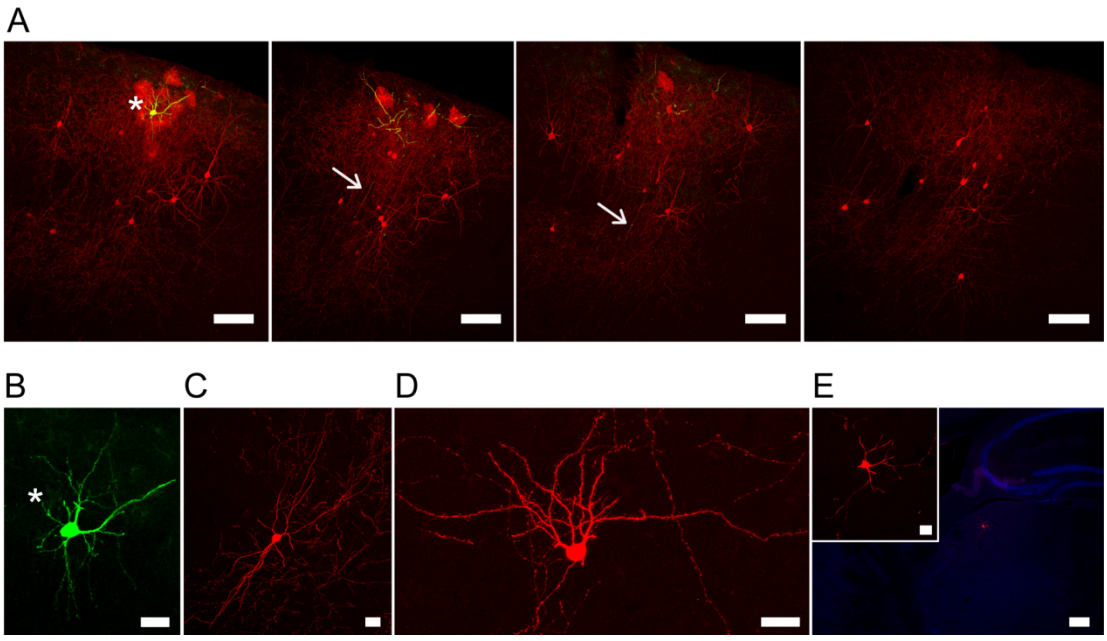
A
B
C
D
E

Movie S3.1. *In Vivo* Two-Photon Shadow Imaging and Single Cell Electroporation

A pipette containing intracellular solution, 50 μm of Alexa 594, and 450 ng/μL of pCAG-YTB was advanced toward the shadow of a single layer 2/3 neuron visualized under two-photon microscopy, as shown in Fig. 3.3B. As the pipette approached the cell, there was approximately 20 mmHg of pressure on the pipette. This pressure maintained the shadow imaging and kept the tip clear of debris. As the pipette touched the membrane of the neuron, a small dimple could be seen forming around the pipette tip as dye accumulated from the positive pressure on the pipette. At this moment, the resistance of the pipette electrode was approximately 30% above the initial resistance of the electrode before patching. The pressure was released on the pipette and the electroporation pulses were delivered, immediately filling the cell body with dye. Plasmid gene transfection was successful, as was confirmed 5 days later by expression of venusYFP in the same neuron (Fig. 3.3C). Available for download online.

Supplementary Experimental Procedures

In Vivo Two-Photon Microscopy

A Movable Objective Microscope (Sutter) coupled to a Chameleon Ultra II mode-locked Ti:Sapphire laser (Coherent) was used for two-photon imaging. Standard wavelengths for two-photon microscopy were 815 or 920 nm. A waveplate (Newport) was used in conjunction with a beamsplitter cube (Newport) to modulate the power of the excitation laser light. A 40X water-immersion objective was used during shadow-patching experiments (Olympus or Zeiss). Fluorescent light was detected by photomultiplier tubes (Hamamatsu), after being filtered by one of two emission filter sets: HQ535/50, and HQ610/75 (Chroma). ScanImage software (Pologruto et al., 2003) was used for image acquisition and images and time lapse videos were processed offline in Matlab (MathWorks) and ImageJ (http://rsbweb.nih.gov/ij/).

***In Vivo* Surgery**

All experiments involving living animals were approved by the Salk Institute's Institutional Animal Care and Use Committee. C57 BL/6J wild-type mice (age 2-3 months) were anesthetized with a ketamine and xylazine cocktail (100 mg/kg and 10 mg/kg respectively, IP), supplemented by ~1% isoflurane in oxygen to maintain surgical plane anesthesia. In some cases, carprofen and dexamethasone were administered subcutaneously (5 mg/kg and 2 mg/kg respectively), and ibuprofen (30 mg/kg) was administered post-operatively in the drinking water for the duration of the experiment. The mouse was placed in a stereotaxic device, ophthalmic ointment was applied to the eyes and a midline incision of the scalp was performed over the skull. A 1x1 mm square was drawn on the skull over primary visual cortex (V1) using known stereotaxic coordinates. In separate experiments, visual responsiveness of this brain area was confirmed by visual stimulation electrophysiology experiments (data not shown). A craniotomy was performed over this area using a dental drill by thinning the border of the marked area in a circular or rectangular fashion, leaving an 'island' of undrilled bone in the center. Great care was taken to prevent overheating of the brain or subdural bleeding by drill induced friction by stopping often and cooling the bone with chilled artificial cerebrospinal fluid (ACSF, in mM: 125 NaCl, 10 d-glucose, 10 HEPES, 3.1 $CaCl_2$, 1.3 $MgCl_2$; or 150 NaCl, 2.5 KCl, 10 HEPES, 2 $CaCl_2$, 1 $MgCl_2$). Once the drilled bone was thin enough that it was transparent and easily bent by applying a small amount of pressure to the undrilled bone the island of undrilled bone was removed slowly. The brain was rinsed with ACSF to remove any bleeding that occurred upon the removal of the bone. The dura was left intact. A

temporary water-tight imaging chamber was mounted around the area of the craniotomy and the stereotaxic stage was transferred to a custom-built two-photon microscope for imaging and single cell electroporation.

Imaging Chamber

A temporary water-tight imaging chamber was mounted around the craniotomy using a 1 mm thick cross section of a 3 ml syringe (11mm O.D., 10mm I.D.) filled with Kwik-Cast silicone elastomer (World Precision Instruments) in a bowl-like shape surrounding a ~3x4 mm rectangular opening around the craniotomy. The temporary chamber was made by first filling the plastic ring with 1.5% agarose (Type III-A, Sigma) in ACSF over the craniotomy. The ring was removed and the agar was cut with forceps to leave a ~3x4 mm rectangle of agar aligned to one side of the craniotomy leaving room on the other side for the pipette's trajectory, and the remnants were discarded and the skull was dried. The ring was replaced centered on the craniotomy and Kwik-Cast was applied to under-fill the volume between the agar rectangle and the plastic ring so that it created a bowl-like shape. Once the Kwik-Cast had set (~10 min) the agar rectangle was removed and the chamber was filled with ACSF. In some experiments, a custom metal frame was fixed to the skull with veterinary glue and dental cement before the craniotomy was performed, and was used to fix the head of the animal and act as a water immersion chamber. A ground wire was installed under the skin. The mouse stereotaxic stage was transferred to a custom-built two-photon microscope for imaging and single-cell electroporation.

In Vivo Single Cell Electroporation

The microscope's light path was switched from two-photon mode to an epifluorescence microscope mode with eyepieces. Using a 5x objective with a reticle scale in an eyepiece and an external light source, a pipette trajectory was calculated so that the pipette would enter the brain and reach its terminus in a blood-vessel void area following a 30 degree from horizontal trajectory to a depth of approximately 175 µm below the dura surface. The ACSF was removed from the imaging chamber and a pipette containing intracellular solution (in mM: 130 K-gluconate, 0.2 EGTA, 2 MgCl2, 6 KCl, 10 HEPES), Alexa Fluor 488 or 594 dye (50 µM, Invitrogen), and plasmid DNA (450 ng/µl total concentration of either pCAG-YTB or 150 ng/µl of each of the following plasmids: pCMMP-TVA800, pHCMV-RabiesG, and pCAG-mCherry or pCAG-venusYFP), and was placed over the craniotomy within the microscope's field of view. The pCAG-YTB plasmid coded for the genes for venusYFP, TVA950 and SAD-B19G in series, separated by 2A elements and GSG linkers to promote equal expression of all three genes (Szymczak et al., 2004), in the following order after a CAG enhanced CMV promoter: venusYFP-GSG-F2A-TVA-GSG-T2A-SAD-B19G. The pipette tip was aligned with the entry point on the reticle scale and the pipette was lowered slowly toward the brain. When the pipette was just above the dura, >100 mmHg of pressure was applied to the back of the pipette and the pipette was lowered until it just touched the dura. At this moment, the electrical circuit was completed so a resistance could be registered by the Axoporator and was typically 10-60 MΩ at this point. The micromanipulator was switched to diagonal

advance mode (ROE-200, Sutter), and the pipette was advanced while positive pressure pulses were applied to the back of the pipette with a syringe until the pipette reached a depth of 175-225 μm below the pial surface. The pipette was withdrawn several microns and the pressure was lowered to 50-90 mmHg. It was often possible to see a cloud of fluorescent dye surrounding the pipette in the brain under epifluorescence and this was a good indication that the pipette was not clogged. The pipette resistance was 10-12 MΩ in the brain, and had an approximately 0.5 μm inner diameter tip (Borosilicate glass with filament, 0.86 mm I.D., 1.5 mm O.D., Sutter). The imaging chamber was filled with ACSF and a 40x objective was installed on the microscope (Olympus or Zeiss). The pipette was found at its dura entry point using epifluorescence and the microscope was switched to two-photon mode.

The depth of the pipette tip relative to the dura was confirmed under two-photon microscopy and the pipette was adjusted, usually by retracting it diagonally so that the tip was between 150 and 175 μm deep. Positive pressure pulses were applied to clear the tip of debris and fill the extracellular space with dye. Given that the dye is not actively taken up by neurons but accumulates in the extracellular space, the cells appeared as dark shadows on a bright background in the thin optical slice (Kitamura et al., 2008; Nevian and Helmchen, 2007). The pipette location was optimized to approach a single cell with pyramidal cell body morphology (i.e., large round cell body relative to the other shadows of triangular shaped cells and smaller cell bodies and blood vessels which characteristically extended throughout the z-axis, Kitamura et

al., 2008), away from the pipette track. The pressure on the pipette while optimizing its position was typically 40-90 mmHg.

Once the pipette location had been optimized, the pressure was reduced to approximately 20 mmHg and the pipette was moved slowly toward the cell. The depth of the pipette was often adjusted while approaching the cell to remain in the same plane as the cell body. Small pulses of positive pressure were used to keep the pipette clear of debris and maintain the shadow imaging. Once the pipette was in close proximity of the cell, the resistance was monitored until a 20-30% increase in the resistance of the electrode was observed. The patch was also observed under two-photon microscopy and a small dimple in the cell membrane filled with dye was sometimes observed forming around the pipette tip (Fig. 3.3B_2 and Movie S1). At this point, the pressure was released on the pipette and the electroporation pulses were delivered. Upon release of pressure, there was often a slight increase in the resistance of the electrode. In cases when this increase doubled or tripled the electrode resistance, the membrane would often seal with the pipette following electroporation and the cell would be irrevocably damaged during pipette withdrawal, and this was avoided. 50 or 100 square wave voltage pulses were delivered at 50 or 100 Hz respectively with an Axoporator 800A (Molecular Probes). The pulses were 500 μs in duration and -12 V in amplitude (Judkewitz et al., 2009; Kitamura et al., 2008). Electroporation success was verified by immediate filling of the cell body with dye. The pipette was then immediately retracted slowly following a 30° diagonal trajectory. Only one neuron was electroporated in each animal, except for one experiment in which a second

neuron was electroporated. In this experiment, both neurons expressed the electroporated marker gene but neither was infected by the virus, nor were there any other neurons infected by the virus. They have been included here as examples of unsuccessful infection of transfected neurons. The microscope was switched to epifluorescence mode and the relative measurements of the ROE-200 manipulator were used to determine the location of the cell under the pattern of blood vessels using the microscope's eye pieces. The reticle was used to determine the relative location of the cell to the surrounding landmarks in the blood vessel pattern and a sketch was made to assist targeting for the virus injection.

Acknowledgments

We are grateful for support from the National Institutes of Health, the Kavli Institute for Brain and Mind, the Institute for Neural Computation, and the National Science Foundation Bridge to the Doctorate Program. We thank D. Lyon for helpful discussions, I. Wickersham and N. Wall for reagents, M. de la Parra, K. von Bochmann, M. Garrett and T. Lien for technical assistance, and members of the Callaway laboratory for discussions.

Publication Acknowledgements

Chapter 3, in full, is a reprint of the material as it appears in Neuron, 2010, Marshel, James H.; Mori, Takuma; Nielsen, Kristina; Callaway, Edward M., Cell Press, 2010. The dissertation author is the primary investigator and author of this material.

References

Aaron, G., and Yuste, R. (2006). Reverse optical probing (ROPING) of neocortical circuits. Synapse *60*, 437-440.

Astic, L., Saucier, D., Coulon, P., Lafay, F., and Flamand, A. (1993). The CVS strain of rabies virus as transneuronal tracer in the olfactory system of mice. Brain Res *619*, 146-156.

Banaszynski, L.A., Sellmyer, M.A., Contag, C.H., Wandless, T.J., and Thorne, S.H. (2008). Chemical control of protein stability and function in living mice. Nat Med *14*, 1123-1127.

Brown, S.P., and Hestrin, S. (2009a). Cell-type identity: a key to unlocking the function of neocortical circuits. Curr Opin Neurobiol *19*, 415-421.

Brown, S.P., and Hestrin, S. (2009b). Intracortical circuits of pyramidal neurons reflect their long-range axonal targets. Nature *457*, 1133-1136.

Crick, F.H. (1979). Thinking about the brain. Sci Am *241*, 219-232.

Dantzker, J.L., and Callaway, E.M. (1998). The development of local, layer-specific visual cortical axons in the absence of extrinsic influences and intrinsic activity. J Neurosci *18*, 4145-4154.

DeFelipe, J., and Farinas, I. (1992). The pyramidal neuron of the cerebral cortex: morphological and chemical characteristics of the synaptic inputs. Prog Neurobiol *39*, 563-607.

Douglas, R., Markram, H., and Martin, K. (2003). The Synaptic Organization of the Brain, 5 edn (Oxford: Oxford University Press).

Douglas, R.J., and Martin, K.A. (2004). Neuronal circuits of the neocortex. Annu Rev Neurosci *27*, 419-451.

Etessami, R., Conzelmann, K.K., Fadai-Ghotbi, B., Natelson, B., Tsiang, H., and Ceccaldi, P.E. (2000). Spread and pathogenic characteristics of a G-deficient

rabies virus recombinant: an in vitro and in vivo study. J Gen Virol *81*, 2147-2153.

Faria, P.A., Chakraborty, P., Levay, A., Barber, G.N., Ezelle, H.J., Enninga, J., Arana, C., van Deursen, J., and Fontoura, B.M. (2005). VSV disrupts the Rae1/mrnp41 mRNA nuclear export pathway. Mol Cell *17*, 93-102.

Feldmeyer, D., Lübke, J., Silver, R.A., and Sakmann, B. (2002). Synaptic connections between layer 4 spiny neurone-layer 2/3 pyramidal cell pairs in juvenile rat barrel cortex: physiology and anatomy of interlaminar signalling within a cortical column. J Physiol *538*, 803-822.

Gossen, M., and Bujard, H. (2002). Studying gene function in eukaryotes by conditional gene inactivation. Annu Rev Genet *36*, 153-173.

Haas, K., Sin, W.C., Javaherian, A., Li, Z., and Cline, H.T. (2001). Single-cell electroporation for gene transfer in vivo. Neuron *29*, 583-591.

Judkewitz, B., Rizzi, M., Kitamura, K., and Häusser, M. (2009). Targeted single-cell electroporation of mammalian neurons in vivo. Nat Protoc *4*, 862-869.

Kampa, B.M., Letzkus, J.J., and Stuart, G.J. (2006). Cortical feed-forward networks for binding different streams of sensory information. Nat Neurosci *9*, 1472-1473.

Kawaguchi, Y., and Kondo, S. (2002). Parvalbumin, somatostatin and cholecystokinin as chemical markers for specific GABAergic interneuron types in the rat frontal cortex. J Neurocytol *31*, 277-287.

Kelly, R.M., and Strick, P.L. (2000). Rabies as a transneuronal tracer of circuits in the central nervous system. J Neurosci Methods *103*, 63-71.

Kelly, R.M., and Strick, P.L. (2003). Cerebellar loops with motor cortex and prefrontal cortex of a nonhuman primate. J Neurosci *23*, 8432-8444.

Kirov, S.A., Sorra, K.E., and Harris, K.M. (1999). Slices have more synapses than perfusion-fixed hippocampus from both young and mature rats. J Neurosci *19*, 2876-2886.

Kitamura, K., Judkewitz, B., Kano, M., Denk, W., and Häusser, M. (2008). Targeted patch-clamp recordings and single-cell electroporation of unlabeled neurons in vivo. Nat Methods *5*, 61-67.

Kozloski, J., Hamzei-Sichani, F., and Yuste, R. (2001). Stereotyped position of local synaptic targets in neocortex. Science *293*, 868-872.

Larkman, A.U. (1991). Dendritic morphology of pyramidal neurones of the visual cortex of the rat: III. Spine distributions. J Comp Neurol *306*, 332-343.

Lefort, S., Tomm, C., Floyd Sarria, J.C., and Petersen, C.C. (2009). The excitatory neuronal network of the C2 barrel column in mouse primary somatosensory cortex. Neuron *61*, 301-316.

Lewis, B.C., Chinnasamy, N., Morgan, R.A., and Varmus, H.E. (2001). Development of an avian leukosis-sarcoma virus subgroup A pseudotyped lentiviral vector. J Virol *75*, 9339-9344.

Livet, J., Weissman, T.A., Kang, H., Draft, R.W., Lu, J., Bennis, R.A., Sanes, J.R., and Lichtman, J.W. (2007). Transgenic strategies for combinatorial expression of fluorescent proteins in the nervous system. Nature *450*, 56-62.

Luo, L., Callaway, E.M., and Svoboda, K. (2008). Genetic dissection of neural circuits. Neuron *57*, 634-660.

Margrie, T.W., Meyer, A.H., Caputi, A., Monyer, H., Hasan, M.T., Schaefer, A.T., Denk, W., and Brecht, M. (2003). Targeted whole-cell recordings in the mammalian brain in vivo. Neuron *39*, 911-918.

Markram, H., Lübke, J., Frotscher, M., Roth, A., and Sakmann, B. (1997). Physiology and anatomy of synaptic connections between thick tufted pyramidal neurones in the developing rat neocortex. J Physiol *500 (Pt 2)*, 409-440.

Mebatsion, T., König, M., and Conzelmann, K.K. (1996a). Budding of rabies virus particles in the absence of the spike glycoprotein. Cell *84*, 941-951.

Mebatsion, T., Schnell, M.J., Cox, J.H., Finke, S., Conzelmann, K.K. (1996b). Highly stable expression of a foreign gene from rabies virus vectors. Proc Natl Acad Sci U S A *93*, 7310-7314.

Nassi, J.J., and Callaway, E.M. (2006). Multiple circuits relaying primate parallel visual pathways to the middle temporal area. J Neurosci *26*, 12789-12798.

Nevian, T., and Helmchen, F. (2007). Calcium indicator loading of neurons using single-cell electroporation. Pflugers Arch *454*, 675-688.

Ohki, K., Chung, S., Ch'ng, Y.H., Kara, P., and Reid, R.C. (2005). Functional imaging with cellular resolution reveals precise micro-architecture in visual cortex. Nature *433*, 597-603.

Peterlin, Z.A., Kozloski, J., Mao, B.Q., Tsiola, A., and Yuste, R. (2000). Optical probing of neuronal circuits with calcium indicators. Proc Natl Acad Sci U S A *97*, 3619-3624.

Peters, A., and Kaiserman-Abramof, I.R. (1970). The small pyramidal neuron of the rat cerebral cortex. The perikaryon, dendrites and spines. Am J Anat *127*, 321-355.

Petreanu, L., Huber, D., Sobczyk, A., and Svoboda, K. (2007). Channelrhodopsin-2-assisted circuit mapping of long-range callosal projections. Nat Neurosci *10*, 663-668.

Petreanu, L., Mao, T., Sternson, S.M., and Svoboda, K. (2009). The subcellular organization of neocortical excitatory connections. Nature *457*, 1142-1145.

Poulet, J.F., and Petersen, C.C. (2008). Internal brain state regulates membrane potential synchrony in barrel cortex of behaving mice. Nature *454*, 881-885.

Rae, J.L., and Levis, R.A. (2002). Single-cell electroporation. Pflugers Arch *443*, 664-670.

Rathenberg, J., Nevian, T., and Witzemann, V. (2003). High-efficiency transfection of individual neurons using modified electrophysiology techniques. J Neurosci Methods *126*, 91-98.

Schnell, M.J., Mebatsion, T., and Conzelmann, K.K. (1994). Infectious rabies viruses from cloned cDNA. EMBO J *13*, 4195-4203.

Schüz, A., and Palm, G. (1989). Density of neurons and synapses in the cerebral cortex of the mouse. J Comp Neurol *286*, 442-455.

Silberberg, G., Grillner, S., LeBeau, F.E., Maex, R., and Markram, H. (2005). Synaptic pathways in neural microcircuits. Trends Neurosci *28*, 541-551.

Silver, R.A., Lübke, J., Sakmann, B., and Feldmeyer, D. (2003). High-probability uniquantal transmission at excitatory synapses in barrel cortex. Science *302*, 1981-1984.

Somogyi, P., Tamás, G., Lujan, R., and Buhl, E.H. (1998). Salient features of synaptic organisation in the cerebral cortex. Brain Res Brain Res Rev *26*, 113-135.

Song, S., Sjöström, P.J., Reigl, M., Nelson, S., and Chklovskii, D.B. (2005). Highly nonrandom features of synaptic connectivity in local cortical circuits. PLoS Biol *3*, e68.

Stepanyants, A., and Chklovskii, D.B. (2005). Neurogeometry and potential synaptic connectivity. Trends Neurosci *28*, 387-394.

Stepanyants, A., Martinez, L.M., Ferecskó, A.S., and Kisvárday, Z.F. (2009). The fractions of short- and long-range connections in the visual cortex. Proc Natl Acad Sci U S A *106*, 3555-3560.

Tamás, G., Szabadics, J., Lörincz, A., and Somogyi, P. (2004). Input and frequency-specific entrainment of postsynaptic firing by IPSPs of perisomatic or dendritic origin. Eur J Neurosci *20*, 2681-2690.

Thomson, A.M., and Bannister, A.P. (2003). Interlaminar connections in the neocortex. Cereb Cortex *13*, 5-14.

Thomson, A.M., Deuchars, J., and West, D.C. (1993). Large, deep layer pyramid-pyramid single axon EPSPs in slices of rat motor cortex display paired pulse and frequency-dependent depression, mediated presynaptically and self-facilitation, mediated postsynaptically. J Neurophysiol *70*, 2354-2369.

Thomson, A.M., and Lamy, C. (2007). Functional maps of neocortical local circuitry. Front Neurosci *1*, 19-42.

Thomson, A.M., West, D.C., Wang, Y., and Bannister, A.P. (2002). Synaptic connections and small circuits involving excitatory and inhibitory neurons in layers 2-5 of adult rat and cat neocortex: triple intracellular recordings and biocytin labelling in vitro. Cereb Cortex *12*, 936-953.

Tiscornia, G., Singer, O., and Verma, I.M. (2006). Production and purification of lentiviral vectors. Nat Protoc *1*, 241-245.

Ugolini, G. (1995). Specificity of rabies virus as a transneuronal tracer of motor networks: transfer from hypoglossal motoneurons to connected second-order and higher order central nervous system cell groups. J Comp Neurol *356*, 457-480.

Wang, Y., Markram, H., Goodman, P.H., Berger, T.K., Ma, J., and Goldman-Rakic, P.S. (2006). Heterogeneity in the pyramidal network of the medial prefrontal cortex. Nat Neurosci *9*, 534-542.

Wickersham, I.R., Finke, S., Conzelmann, K.K., and Callaway, E.M. (2007a). Retrograde neuronal tracing with a deletion-mutant rabies virus. Nat Methods *4*, 47-49.

Wickersham, I.R., Lyon, D.C., Barnard, R.J., Mori, T., Finke, S., Conzelmann, K.K., Young, J.A., and Callaway, E.M. (2007b). Monosynaptic restriction of transsynaptic tracing from single, genetically targeted neurons. Neuron *53*, 639-647.

Wickersham, I.R., Sullivan, H.A., and Seung, H.S. (2010). Production of glycoprotein-deleted rabies viruses for monosynaptic tracing and high-level gene expression in neurons. Nat Protoc *5*, 595-606.

Yoshimura, Y., and Callaway, E.M. (2005). Fine-scale specificity of cortical networks depends on inhibitory cell type and connectivity. Nat Neurosci *8*, 1552-1559.

Yoshimura, Y., Dantzker, J.L., and Callaway, E.M. (2005). Excitatory cortical neurons form fine-scale functional networks. Nature *433*, 868-873.

Young, J.A., Bates, P., and Varmus, H.E. (1993). Isolation of a chicken gene that confers susceptibility to infection by subgroup A avian leukosis and sarcoma viruses. J Virol *67*, 1811-1816.

CHAPTER IV

RETINOTOPIC AND RECEPTIVE FIELD CHARACTERIZATION OF MOUSE STRIATE AND EXTRASTRIATE VISUAL CORTEX

Summary

The brain processes information in specialized circuits, and often segregates functions into distinct brain regions. In the primate visual system, several cortical visual areas each process unique features of an image. This segregation likely affords advantages for building selective receptive fields designed to encode specific features. Understanding these computations requires teasing apart the circuit elements involved in each unique computation. Recent technological advances in microcircuit analysis of the mouse brain promise to make these studies possible in this organism. However, very little is known about the function of higher visual areas in the mouse. To provide a framework for functional microcircuit analysis of visual information processing across visual areas, we characterized the mouse extrastriate visual system along several dimensions. First, we mapped the retinotopic organization of visual cortex with intrinsic imaging to delineate each visual area. We found at least 8 visual areas surrounding V1, largely consistent with the organization predicted from anterograde tracer injections into V1. Next, we characterized large populations of neurons within each of these areas using two-photon calcium imaging of visual responses to drifting grating stimuli varying across several directions (orientations), temporal and spatial frequencies. These results provide a catalog of basic feature selectivity across visual areas. We found that all extrastriate areas investigated (LM, LI, AL, RL, AM, PM) preferred gratings drifting at much higher temporal frequencies than eccentricity-matched neurons in V1. Furthermore, neurons in extrastriate areas were more selective for orientation and direction. A subset of areas had similar spatial frequency tuning as

V1, despite having larger receptive fields, and another subset of areas preferred lower spatial frequencies than V1. We explored the interactions between the responses to these stimulus features, and further grouped extrastriate areas based on response characteristics. Our results demonstrate that the mouse visual system, like other species, organizes visual information into visual areas that are selective for distinct visual features.

Introduction

The visual systems of several species have been intensely investigated, revealing distinct patterns of organization believed to subserve efficient visual information processing and perception. For example, one of the hallmarks of the visual system of mammals is a complete and orderly representation of the visual field repeated several times over the visual cortex (Sereno et al., 1994). Many of these visuotopic representations of the visual field have been considered to be specialized processing units for different features of a visual stimulus, evidenced by the selective responses of neurons in a visual area to specific features such as motion, color or higher level feature integration (Orban, 2008; Maunsell and Newsome, 1987).

A multitude of anatomical and physiological studies have revealed that in many species, parallel streams of information that begin at the retina and segregate through the thalamus, provide structured input to visual cortex in an often orderly fashion by targeting specific cortical sublamina or even specific visual areas (Nassi and Callaway, 2009). The web of selective feedforward and feedback connections

between these areas forms an integrated, multilevel hierarchy of information flow through cortex (Felleman and Van Essen, 1991; Callaway, 2004). The specialized pattern of input to several visual cortical areas has been shown to correlate with the response properties of neurons in those areas (Movshon and Newsome, 1996) and numerous models have been proposed for how neurons in those areas integrate those specific inputs at the microcircuit level to generate their stereotyped spiking patterns.

However, techniques available to investigate visual cortex in traditionally studied mammals such as cats, ferrets and nonhuman primates are currently insufficient to discern many of the microcircuit level patterns of connectivity and cellular mechanisms responsible for the selective response properties of neurons in each area. Furthermore, while engineered viruses and increasingly sophisticated electrophysiological and imaging techniques may begin to close this gap, they seem farther from systematic genetic studies. For these reasons, interest has increased recently in exploring many long-held questions about behaviorally relevant visual system development, organization and information processing using the genetically tractable mouse model, in which it has been shown that neurons in mouse primary visual cortex (V1) have highly selective receptive fields similar to other mammals (Niell and Stryker, 2008).

Mouse transgenic technologies permit the study of the role of specific genes during development and in the adult, and have been used to target specific neuronal cell types and circuits for gene expression (Luo et al., 2008). This has aided wide application of optogenetics in the mouse (e.g., Petreanu et al., 2007; Chow et al., 2010). Furthermore, transsynaptic tracing methods have been recently developed to

trace the monosynaptic inputs to specific neuronal cell types in several Cre mouse lines (Wall et al., 2010), and to a single neuron in mouse visual cortex permitting the study of the specific inputs to a single neuron (Marshel et al., 2010). Furthermore, electron microscopy circuit tracing methods have recently been applied in the mouse (Bock et al., 2011; Briggman et al., 2011). The application of these powerful technologies, many of which are exclusively available in the mouse, in addition to the experimental accessibility of the mouse model system, notably to large scale studies, suggests that studies of the mouse visual system may illuminate many of the genetic, circuit and cellular mechanisms responsible for the development, organization and function of the visual system and how those properties relate to behavior. For example, it has been possible to differentiate unambiguously the response properties of pyramidal neurons and interneurons, including several specific subtypes, by imaging transgenic mouse lines labeling interneurons *in vivo* (Sohya et al., 2007; Liu et al., 2009; Kerlin et al., 2010; Runyan et al., 2010).

Despite the general interest and increasing literature on mouse visual cortex, almost all studies to date have focused on mouse V1, with very little known about the visuotopic structure or function of extrastriate visual cortex. A detailed tracing study of the V1 projections to extrastriate visual cortex, and some electrophysiological data, predict several orderly representations of the visual field in mouse extrastriate cortex suggesting that up to 10 visual cortical areas may exist in the mouse (V1, LM, AL, LI, RL, A, AM, PM, P, POR) (Wang and Burkhalter, 2007; Olavarria et al., 1982). This intriguing possibility was in contrast to previous estimates of the retinotopic organization analyzed from electrophysiology and intrinsic imaging data which

predicted far fewer areas (~3-4: V1, V2, Vm-r, Vm-c; Wagor et al., 1980; ~4-5: Kalatsky and Stryker, 2003).

Adequate functional data to confirm the retinotopic areal organization of mouse visual cortex is lacking in the literature. Furthermore, very limited electrophysiological data exist examining the function of mouse extrastriate cortex (Van den Bergh et al., 2010). However, depending on the extent to which the mouse visual system resembles that of other mammals, some mouse extrastriate visual areas may process specific types of sensory information, such as motion, and others may process higher order visual features, such as object feature integration or interactions between sensory modalities. Studying these phenomena in the mouse would open the possibility of applying the many genetic techniques available to probe the development, circuit and cellular mechanisms responsible for the generation of stereotyped receptive field structure and response properties in different visual areas. In order to understand the organization and basic function of mouse extrastriate visual cortex we targeted neurons in distinct visual areas, retinotopically identified using intrinsic signal imaging, for receptive field characterization with in vivo two-photon calcium imaging.

In the current study, our first objective was to establish the functionally-defined borders of mouse extrastriate visual areas by performing fine-scale functional analyses of the retinotopic structure of mouse striate and extrastriate cortex using a novel visual stimulation method for stimulating the entire visual hemi-field of the mouse while simultaneously recording cortical intrinsic optical signals from the entire contralateral visual cortex (Fig 4.1). In addition, we used a novel application of two-

photon calcium dye imaging to map the structure of the retinotopic maps at up to single-cell resolution, often over several millimeters in the same mouse (Fig. 4.2-4.4). These experiments allowed us to draw precise borders around complete and orderly representations of the visual hemi-field—the most straightforward definition of a visual area. Furthermore, this approach revealed regions of visual cortex which appear to be unique, orderly representations of a large region of space, but fail to show a complete visual field representation, as has been observed in other species (Sereno et al., 1994). We identified distinguishing retinotopic map features of up to 9 visual areas.

Once we defined these areal boundaries, we next targeted 7 visual areas for *in vivo* calcium dye imaging of the responses of large populations of layer 2/3 neurons (Fig 4.5), representing known eccentricities of space, to visual stimuli varying across several stimulus dimensions including orientation, direction, temporal frequency and spatial frequency. It was possible to perform all of the retinotopic and receptive field characterization experiments of several visual areas in the same mouse over a single day, facilitating high-throughput analyses of mouse visual areas. Comparing the response properties of these populations of neurons across different visual areas revealed specialized functional properties of all extrastriate visual areas we studied compared to V1. Furthermore, these areas showed different population responses when compared to each other. Interestingly, we found that essentially all extrastriate areas process higher temporal frequency information than V1. Some of the areas maintain the same spatial frequency tuning of V1, despite having larger receptive

fields. Almost all extrastriate areas had improved orientation selectivity, while direction selectivity was the same or slightly higher than V1 in extrastriate areas.

To our knowledge, the results we present here are the first retinotopic and receptive field characterization of the majority of extrastriate visual areas in the mouse. The findings that essentially all extrastriate areas are specialized to process high temporal frequency information makes them strong candidates for motion processing roles in the visual system. The maintenance of relatively high spatial frequency tuning in some areas suggests that these areas form complex receptive fields. The refinement of orientation selectivity suggests either a role of local inhibitory circuitry, or selective inputs from V1. These findings, in addition to the development and application of novel methods in this study for the high throughput investigation of mouse visual areas, may lay the foundation for future studies taking further advantage of the mouse model, especially in terms of genetic manipulations and microcircuit mapping, to study the development and function of the mouse visual system at the level of cellular and circuit mechanisms.

Results

Mouse visual cortex contains several retinotopically organized visual areas

Multiple representations of visual space were found repeated across mouse visual cortex using intrinsic signal imaging to map retinotopy. Using retinotopic map landmarks predicted previously (Wang and Burkhalter, 2007), we evaluated the cortical locations of each predicted visual area. We defined borders between areas based on flips in the map at the visual field peripheries. At each border, the retinotopic

map reversed in visual field sign representation, a classic definition of area border (Sereno et al., 1994). Ultimately, we focused neuronal population analyses on representations of the center of space within these borders, where retinotopic maps were most orthogonal between the azimuth and altitude visual field axes and where we had the greatest confidence in our areal definitions.

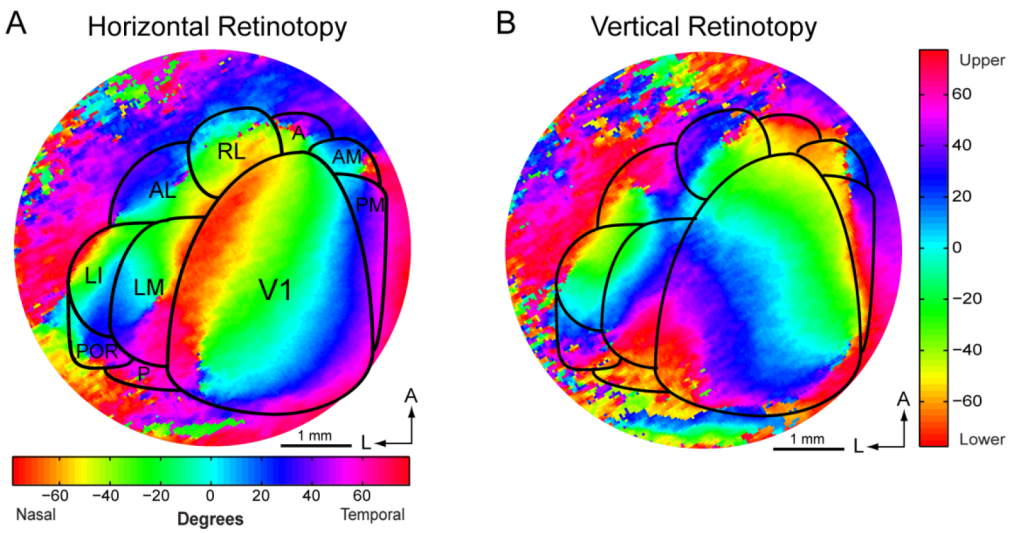

Figure 4.1 | Intrinsic signal imaging of the retinotopic structure of mouse visual cortex. A, Horizontal retinotopy representing azimuth eccentricity in terms of color coding. B, Vertical retinotopy representing altitude eccentricity in terms of color coding. Continuous maps are seen in area V1 and the extrastriate cortex. Borders are drawn around areas based on predictions from Wang and Burkhalter, 2007. Higher resolution imaging using two-photon calcium imaging was used to help draw these borders (Fig. 4.2-4.4).

Retinotopic organization of primary visual cortex (V1)

V1 represents visual space from temporal visual field to nasal visual field along the medial-lateral axis on the cortical surface, and lower to upper visual field along the anterior-posterior axis. The visual field coordinates represented by V1

extend ~140° in the nasal-temporal dimension, and ~100° in the lower-upper dimension. The lateral and medial borders of V1 were easily identified. Most prominent was the lateral border of V1, which represents the nasal periphery. The temporal periphery defined the medial border. Upper visual field representations extended to the posterior edge of our imaging window. The lower visual field representation defined the anterior border of V1, coming to a point on the cortical surface at the lowest eccentricities (Fig. 4.1).

Retinotopic organization of lateral extrastriate areas (P, POR, LM, LI and AL)

The most easily identifiable lateral extrastriate areas were LM and AL. Each of these areas had retinotopic representations which mirrored the V1 representation reflected across V1's lateral border. The border between LM and AL was identified by a reversal at the representation of the lower periphery. A reversal at the temporal periphery was observed at the border between LM and LI, which continue its representation out to the nasal periphery at the far lateral extent of visual cortex (Fig. 4.2). Areas P and POR were more difficult to identify given their anatomical location, but we were able to identify map features of these areas, including their horizontal meridian, although separating these areas based on a border at the nasal periphery was not possible.

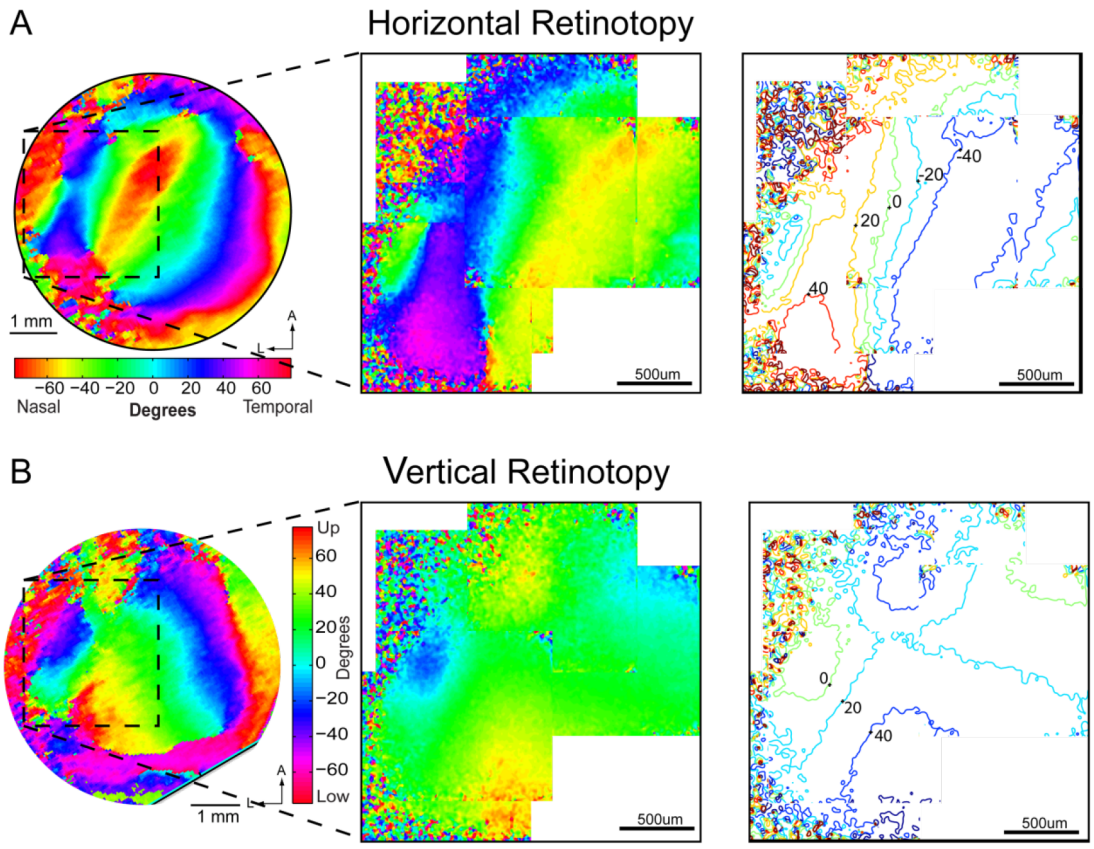

Figure 4.2 | Retinotopic organization of lateral extrastriate cortex. A, Horizonal Retinotopy (Azimuth). B, Vertical Retinotopy (Altitude). A, B, Color coding reflects eccentricity in left two plots corresponding to the colorbar next to the leftmost plots. A, B, Left plot is intrinsic imaging map. Middle plot is montage of multiple two-photon calcium imaging maps stitched together using vasculature pattern (not shown). Right plot is same retinotopy data shown in the middle plot shown in terms of contour lines. Contour lines are labeled with eccentricity. Any line of the same color in the plot has that same eccentricity. A, A clear border can be seen at the nasal periphery between V1 and extrastriate cortex. At the lateral most edge, another representation of the nasal periphery defines the edge of area LI. B, A flip in the map is visible approaching the lower fields and then reflecting back to the upper fields. This transition defines the border between AL and LM.

Retinotopic organization of medial extrastriate areas (PM and AM)

The temporal periphery defined the border between V1 and medial extrastriate areas. Area PM was located just medial to V1, with a representation of horizontal

retinotopy (Azimuth) which mirrored V1's. Interestingly, the vertical retinotopy map continued from temporal to nasal visual fields by rotating 90° on the cortical surface from the lateral-medial axis to the posterior-anterior axis. A representation of the nasal periphery defined the border between PM and AM, with horizontal retinotopy reflected across the anterior posterior axis (Fig. 4.3).

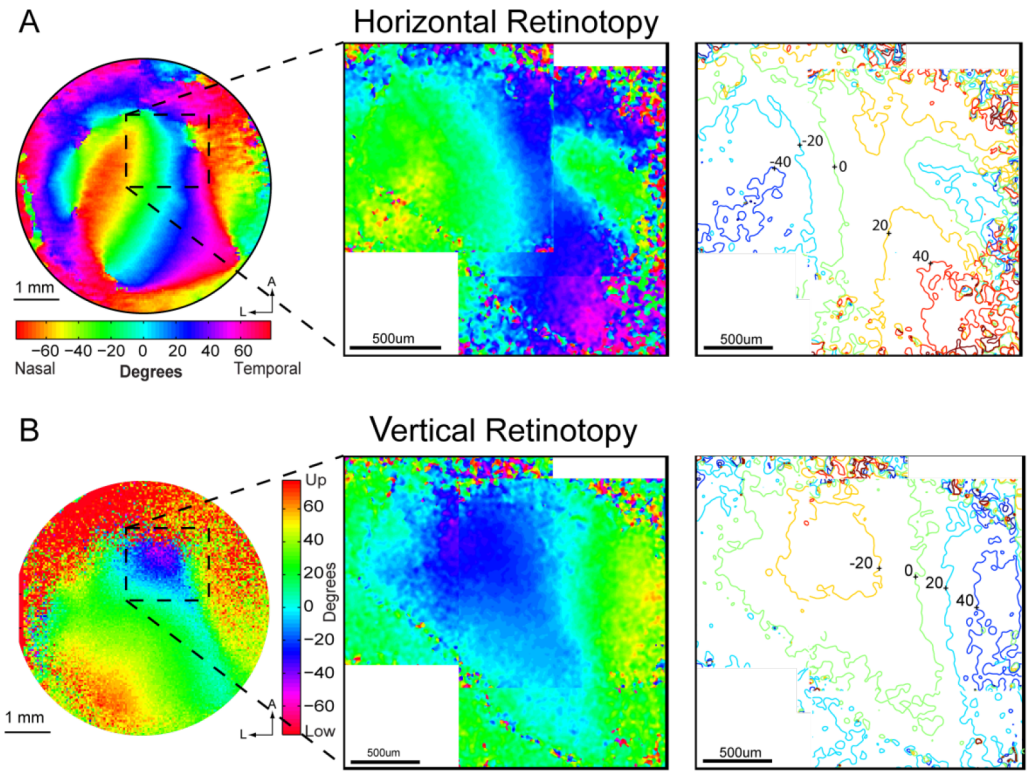

Figure 4.3 | Retinotopic organization of medial extrastriate cortex. A, Horizonal Retinotopy (Azimuth). B, Vertical Retinotopy (Altitude). A, B, Color coding reflects eccentricity in left two plots corresponding to the colorbar next to the leftmost plots. A, B, Left plot is intrinsic imaging map. Middle plot is montage of multiple two-photon calcium imaging maps stitched together using vasculature pattern (not shown). Right plot is same retinotopy data shown in the middle plot shown in terms of contour lines. Contour lines are labeled with eccentricity. Any line of the same color in the plot has that same eccentricity.

Retinotopic organization of anterior extrastriate cortex (RL and A)

Anterior extrastriate cortex had a structure which was more difficult to resolve. However, hallmarks of area RL were clearly visible, including a nearly perpendicular extenstion of the nasal periphery representation from V1's, marking the border between AL and RL. Interestingly, in a few cases, this representation of the nasal periphery appeared to extend anteriorly to form a ring-like structure that surrounded RL's central visual field representation, suggesting that this area may overrepresent this region of space (Fig. 4.4). It was more difficult to define the borders of area A. While this region of cortex was visually responsive, and appeared to have an orderly representation of visual space continuous with the surrounding representations, we did not observe the key feature of a representation of the nasal periphery extending posterior to anterior on the medial side (Wang and Burkhalter, 2007), and thus we did not define an area A.

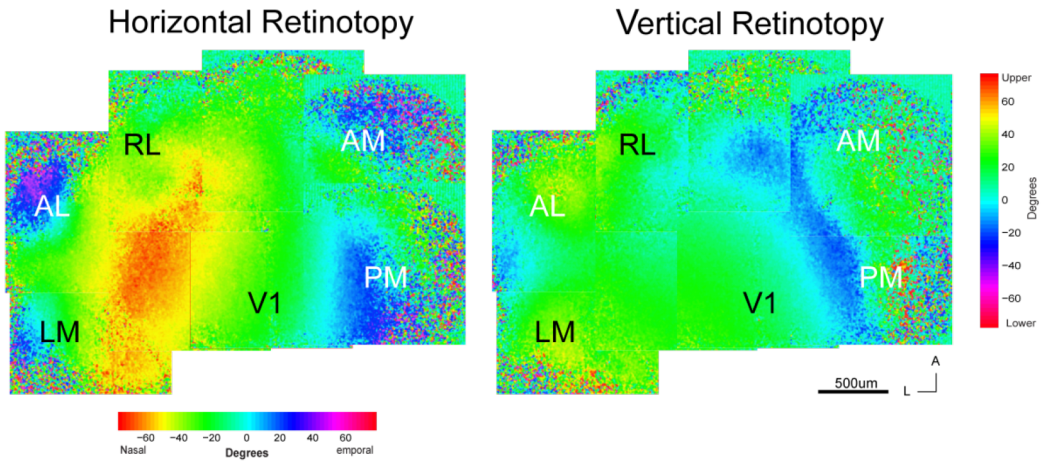

Figure 4.4 | Retinotopic organization of anterior extrastriate cortex. Horizontal and vertical retinotopy from two-photon imaging, with color coding for eccentricity. Area markers are made using retinotopic landmarks described in the text.

High resolution retinotopic mapping with two-photon calcium imaging

In each animal, once we had defined the areal borders as described above using intrinsic imaging, we targeted several visual areas for calcium dye loading. Under two-photon microscopy and low power magnification (16X) we confirmed the retinotopic map from intrinsic imaging at much higher resolution using the calcium signal. This method yielded smooth maps of retinotopy reflecting the neuropil signal and single cell responses. We would often focus on a particular subregion of cortex which we had targeted for dye loading, creating a mosaic of maps with approximately 1 mm square fields of view each, altogether spanning several millimeters (Fig. 4.2-4.4). We stitched these maps together online, and then used the composite map to precisely target the center of space representation of a defined visual area. We performed this process for several visual areas in each animal, using blood vessel landmarks to aid further targeting. Then we switched to a higher power objective (40X), and found each of these targeted locations using the same landmarks. We again confirmed the retinotopic organization of the field of view (approximately 150-300 μm square), allowing measurement of the retinotopic representations of the individual cells within the field of view. Once we had confirmed we were imaging the center-of-space representation of the visual area we proceeded to characterize the response properties of the population of neurons, at single-cell resolution across several stimulus dimensions.

Table 4.1: N's for the experiments and analysis

Area	Total Neurons		Responsive Neurons		Reliable Neurons		Responsive & Reliable		Included Neurons*		N animals	
	SF	TF	SF	TF	SF	TF	SF	TF	SF	TF	SF	TF
	N	*N*	*N (N/Total)*	*N (N/Total)*	*N (N/Total)*	*N (N/Total)*	*N (N/Total)*	*N (N/Total)*	*N (N/Total)*	*N (N/Total)*	*N*	*N*
V1	1419	1382	826 (58%)	718 (52%)	1063 (75%)	984 (71%)	728 (51%)	586 (42%)	728 (51%)	584 (42%)	13	13
LM	590	584	328 (56%)	198 (34%)	495 (84%)	404 (69%)	300 (51%)	171 (29%)	295 (50%)	171 (29%)	8	8
LI	182	193	51 (28%)	35 (18%)	85 (47%)	56 (29%)	42 (23%)	23 (12%)	40 (22%)	23 (12%)	2	2
AL	890	918	418 (47%)	343 (37%)	541 (61%)	542 (59%)	330 (37%)	257 (28%)	323 (36%)	253 (28%)	7	7
RL	616	555	232 (38%)	124 (22%)	382 (62%)	295 (53%)	201 (33%)	96 (17%)	194 (31%)	95 (17%)	8	8
AM	404	311	80 (20%)	25 (8%)	203 (50%)	70 (23%)	63 (16%)	12 (4%)	63 (16%)	11 (4%)	6	6
PM	508	506	172 (34%)	78 (15%)	332 (65%)	230 (45%)	147 (29%)	50 (10%)	147 (29%)	50 (10%)	3	3
Total	4609	4449	2107 (46%)	1521 (34%)	3101 (67%)	2581 (58%)	1811 (39%)	1195 (27%)	1790 (39%)	1187 (27%)	47	47

* Included Neurons are Responsive & Reliable Neurons that were within the central 100° of retinotopic space. These were the neurons included in population analyses.

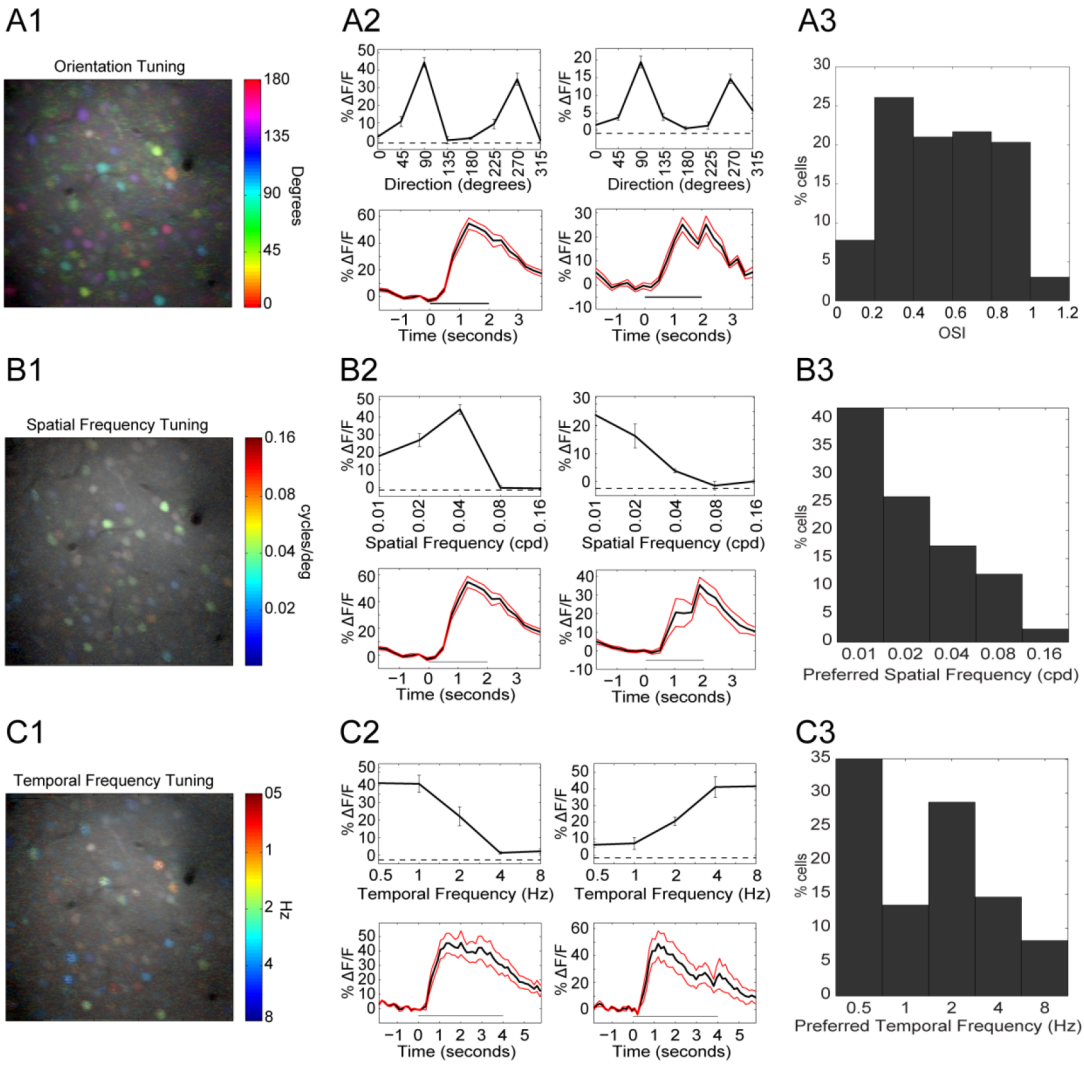

Figure 4.5 | Calcium imaging of population neuronal responses in identified visual area (LM). A, Single cell and population orientation tuning. B, Single cell and population spatial frequency tuning. C, Single cell and population temporal frequency tuning. Left panels (A1,B1,Cl, same field of view) are structural two-photon images overlaid by color corresponding to the stimulus which drove the maximum response (ΔF/F) of each pixel, with the stimulus parameter indicator by the colorbar. A1, A salt-and-pepper organization of orientation selectivity is observed. B1, A diverse set of preferred spatial frequencies are visible in the population, with no apparent spatial relationship. C1, An assortment of responses are found without clear spatial relationship. Middle panels (A2,B2,C2), show 2 example cells from each experiment. A2, Top plots show orientation tuning curves, bottom plots show timecourse response of the neuron. Bar under curves is the stimulus duration. B2, Top plots shows spatial frequency tuning curves. Bottom plots are timecourses. C2, Top plots show temporal frequency tuning curves. Bottom plots are timecourses. Right plots show the population histograms for area LM in terms of orientation selectivity index (OSI, A3), preferred spatial frequency (B3) and preferred temporal frequency (C3).

Population analysis of mouse cortical visual areas

Within the same field of view as the high-resolution retinotopy experiment, we recorded the calcium signals of the population of neurons in response to sine-wave gratings varying across temporal and spatial frequencies, which drifted in 8-12 directions (Fig. 4.5). Three gratings experiments were run for each field of view. A temporal frequency experiment held the spatial frequency constant (a single value between 0.02 and 0.04 cpd) and varied both temporal frequency (0.5, 1, 2, 4 and 8 Hz) and direction (8 equally spaced directions). A spatial frequency experiment held temporal frequency constant (typically 1 Hz) and varied spatial frequency (0.01, 0.02, 0.04, 0.08, 0.16 cpd) and direction (8 equally spaced directions). Finally, a direction experiment held temporal frequency (typically 1 Hz) and spatial frequency (typically 0.04 cpd) constant while varying direction (12 equally spaced directions).

We analyzed each of these experiments independently to determine the scores of each neuron on several parameters (preferred temporal frequency, preferred spatial frequency, orientation selectivity, direction selectivity, tuning bandwidth and trial-to-trial reliability). Where necessary depending on scientific question (e.g., to determine the correlation between spatial and temporal frequencies tunings for a given neuron, and in the multivariate statistics described below) we combined across these experiments by aligning and using the same cell ROIs across experiments in order to keep track of the same neuron identities across experiments. Since all experiments were in the same field of view, the majority of neurons were detected across experiments, and these overlapping neuron ROIs were included in combined-

experiment analyses (e.g., for multivariate analyses). Neurons which were both responsive (response > 6%ΔF/F) and reliable (maximum response > sum of standard deviations of max response condition and blank conditions) were used for all analyses of response metrics, and as the denominator in analyses of fraction of neurons expressing a given parameter score. Table 4.1 summarizes the number of neurons in each category.

Mouse cortical visual areas encode different visual features

As described above, we scored each neuron along several parameters in order to quantify their tuning. Each of these parameters was considered a dependent variable, and area grouping was considered the independent variable. We found that overall, there was a main effect of area on our dependent variables meaning that at least one visual area could be distinguished from another statistically (one-way MANOVA, independent variable: Area, dependent variables: Preferred Temporal Frequency, Preferred Spatial Frequency, OSI, and DSI, $F_{(24, 2537)} = 18.021$, $p < 0.0005$, Wilk's $\lambda = 0.577$, $\varepsilon^2 = 0.128$). We followed up this multivariate test with both parametric and non-parametric univariate tests (both one-way ANOVA and Kruskal-Wallis) comparing the scores on each dependent variable as a function of area to determine whether the mean and/or medians could be distinguished statistically in each comparison. Both parametric and non-parametric one-way tests gave comparable results in all instances. We followed up any significant one-way test with the appropriate post-hoc test (Tukey-Kramer HSD) in order to determine which pairs of areas differed significantly on each parameter. This statistical design accounted for the

familywise error rate in the MANOVA test and for multiple comparisons in each one-way ANOVA or Kruskal-Wallis test and for post-hoc tests.

Mouse extrastriate areas encode high temporal frequency information

We compared the mean preferred temporal frequency of each population of neurons from each visual area. We found a main effect of visual area on preferred temporal frequency (one-way ANOVA $F_{(6,1180)} = 49.958$, $p < 0.0005$, one-way Kruskal-Wallis $p < 0.0005$). We followed up with post-hoc multiple comparisons tests to determine which areas were different from each in terms of preferred temporal frequency. All extrastriate visual areas investigated except area PM had higher preferred temporal frequency tuning than V1 (LM, LI, AL, RL, AM; $p < 0.05$, Tukey-Kramer HSD). We also found differences between several extrastriate areas, and these results are summarized in Fig. 4.6. The mean preferred temporal frequency tuning for area PM was slightly higher than V1, and this difference was significant when we performed a simple t-test between the two distributions ($p < 0.01$, two-tailed, not correcting for multiple comparisons), suggesting that while the difference was small, we may not have detected a significant difference in our multiple comparisons tests given our corrections to account for multiple comparisons.

Figure 4.6 | Temporal frequency tuning across visual areas. A, Preferred temporal frequency tuning. Geometric mean (A1) and post-hoc statistical comparisons from ANOVA (A2) and Kruskal-Wallis tests (A3). All extrastriate visual areas had higher preferred temporal frequency tuning than V1, and this difference was significant for all areas except PM. The ANOVA and Kruskal-Wallis post-hoc tests are in close agreement and reveal additional distinctions between extrastriate visual areas in terms of preferred temporal frequency. B, Temporal frequency bandwidth. Mean in octaves (B1), and post-hoc statistics (B2,B3). Areas LM, AL and RL are significantly higher in temporal frequency bandwidth tuning than V1. C1, Mean high cutoff temporal frequency across areas. C2,C3, post-hoc statistical comparisons between the areas. Areas LM, AL and RL had higher high cutoff spatial frequency than V1. Additonal comparisons were significant between the extrastriate areas. D1, Mean low cutoff temporal frequency. D2,D3, post-hoc statistical comparisons between the areas. Depending on the statistical univariate test, the post-hoc comparisons were significant for only LM or for LM, LI, AL and AM compared to V1 (all higher low cutoff values). Left panels (A1,B1,C1,D1) black lines are S.E.M., and numbers above bars are mean values. Middle panels (A2,B2,C2,D2) post-hoc pairwise comparisons following the highly significant one-way ANOVA. Right panels (A3,B3,C3,D3) post-hoc pairwise comparisons following the highly significant one-way Kruskal-Wallis test. Middle and right panels, blue dots represent significance at least at $p < 0.05$ after correcting for multiple comparisons using the Tukey-Kramer Honestly Significant Difference (HSD) correction.

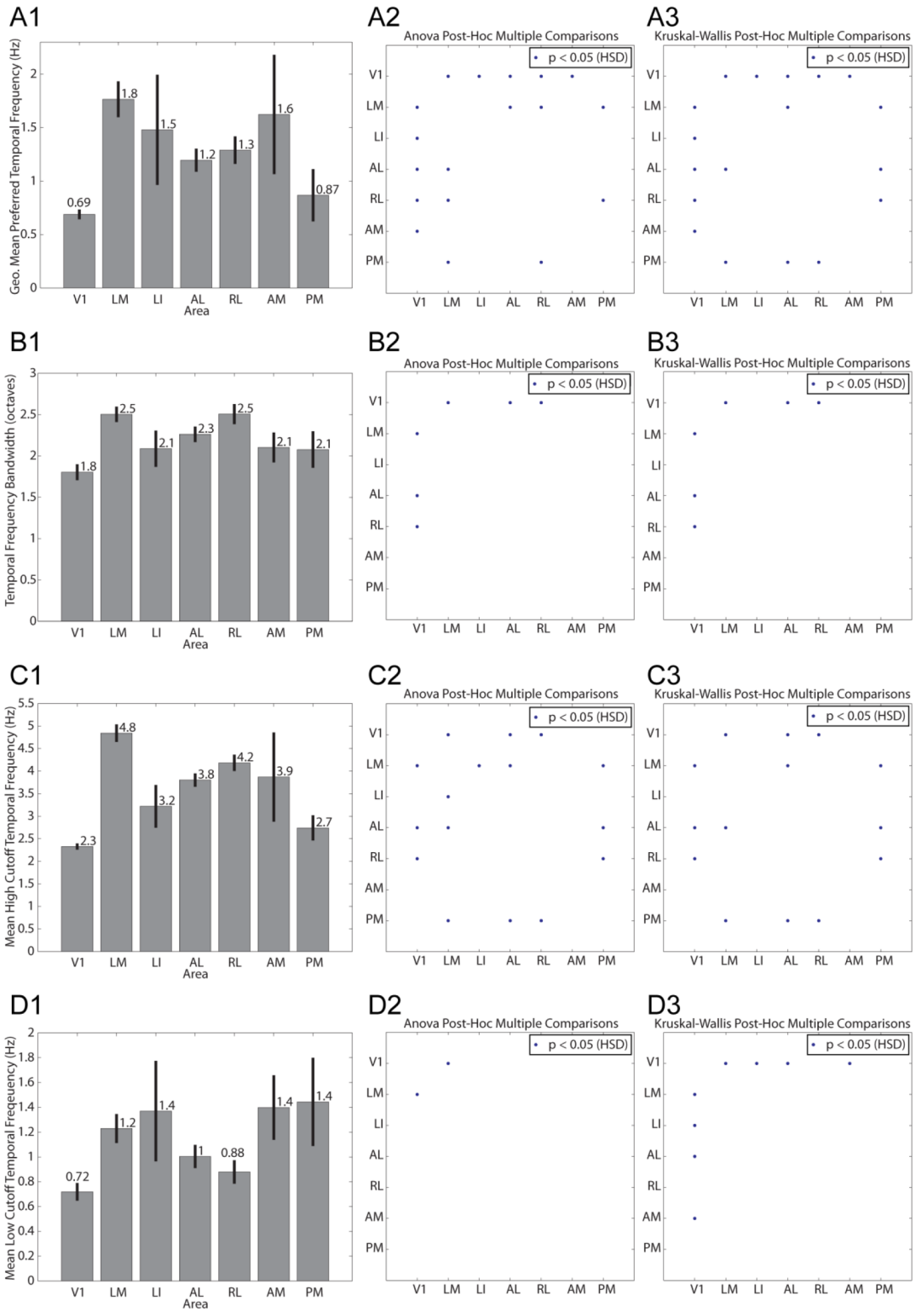
A1
Geo. Mean Preferred Temporal Frequency (Hz)
0.69
1.8
1.5
1.2
1.3
1.6
0.87
V1 LM LI AL RL AM PM
Area
A2
Anova Post-Hoc Multiple Comparisons
p < 0.05 (HSD)
A3
Kruskal-Wallis Post-Hoc Multiple Comparisons
p < 0.05 (HSD)
B1
Temporal Frequency Bandwidth (octaves)
1.8
2.5
2.1
2.3
2.5
2.1
2.1
B2
Anova Post-Hoc Multiple Comparisons
B3
Kruskal-Wallis Post-Hoc Multiple Comparisons
C1
Mean High Cutoff Temporal Frequency (Hz)
2.3
4.8
3.2
3.8
4.2
3.9
2.7
C2
Anova Post-Hoc Multiple Comparisons
C3
Kruskal-Wallis Post-Hoc Multiple Comparisons
D1
Mean Low Cutoff Temporal Freqeuency (Hz)
0.72
1.2
1.4
1
0.88
1.4
1.4
D2
Anova Post-Hoc Multiple Comparisons
D3
Kruskal-Wallis Post-Hoc Multiple Comparisons

Figure 4.7 | Spatial frequency tuning across visual areas. A, Preferred spatial frequency tuning. Geometric mean (A1) and post-hoc statistical comparisons from ANOVA (A2) and Kruskal-Wallis tests (A3). Areas LM, AL, RL and AM had lower preferred spatial frequency tuning than V1. The ANOVA and Kruskal-Wallis post-hoc tests are in close agreement and reveal additional distinctions between extrastriate visual areas in terms of preferred spatial frequency. B, Spatial frequency bandwidth. Mean in octaves (B1), and post-hoc statistics (B2,B3). Areas LM, AL, RL, AM and PM are significantly lower in spatial frequency bandwidth tuning than V1. C1, Mean high cutoff spatial frequency across areas. C2,C3, post-hoc statistical comparisons between the areas. Areas LM, AL, RL, AM and PM had lower high cutoff spatial frequency than V1. AL and LM showed differences from each other, with LM having a higher high cutoff than AL. D1, mean low cutoff spatial frequency. D2,D3, post-hoc statistical comparisons between the areas. The post-hoc comparisons were significant for LM, LI, and AL, and depending on the statistical univariate test, PM compared to V1. LM and AL both had lower low cutoff values than V1, while LI and PM had higher values. Several differences were found between extrastriate areas. Left panels (A1,B1,C1,D1) black lines are S.E.M., and numbers above bars are mean values. Middle panels (A2,B2,C2,D2) post-hoc pairwise comparisons following the highly significant one-way ANOVA. Right panels (A3,B3,C3,D3) post-hoc pairwise comparisons following the highly significant one-way Kruskal-Wallis test. Middle and right panels, blue dots represent significance at least at $p < 0.05$ after correcting for multiple comparisons using the Tukey-Kramer Honestly Significant Difference (HSD) correction.

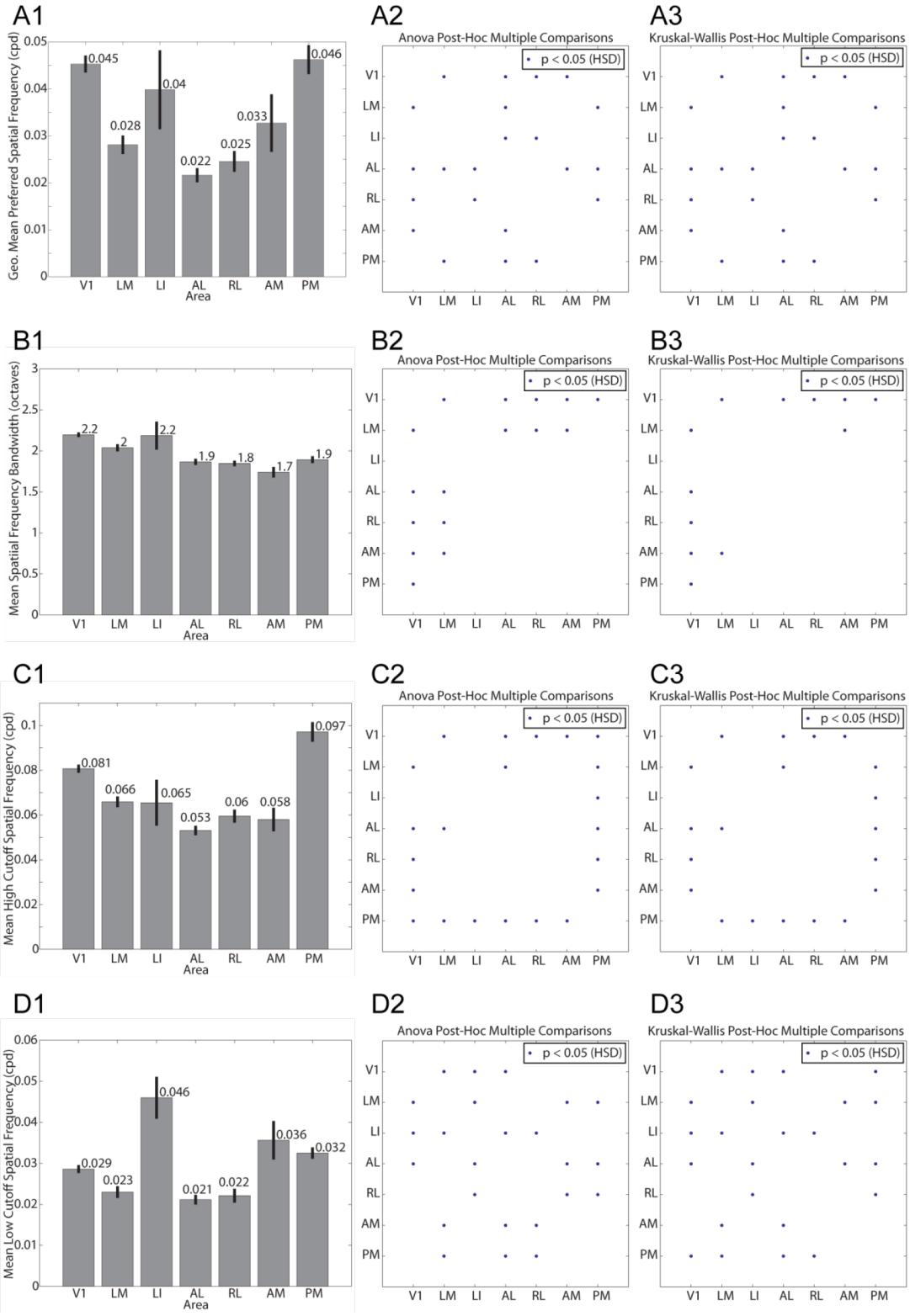
A1
Geo. Mean Preferred Spatial Frequency (cpd)
0.045
0.028
0.04
0.022
0.025
0.033
0.046
V1 LM LI AL RL AM PM
Area
A2
Anova Post-Hoc Multiple Comparisons
p < 0.05 (HSD)
A3
Kruskal-Wallis Post-Hoc Multiple Comparisons
p < 0.05 (HSD)
B1
Mean Spatial Frequency Bandwidth (octaves)
2.2
2
2.2
1.9
1.8
1.7
1.9
B2
Anova Post-Hoc Multiple Comparisons
p < 0.05 (HSD)
B3
Kruskal-Wallis Post-Hoc Multiple Comparisons
p < 0.05 (HSD)
C1
Mean High Cutoff Spatial Frequency (cpd)
0.081
0.066
0.065
0.053
0.06
0.058
0.097
C2
Anova Post-Hoc Multiple Comparisons
p < 0.05 (HSD)
C3
Kruskal-Wallis Post-Hoc Multiple Comparisons
p < 0.05 (HSD)
D1
Mean Low Cutoff Spatial Frequency (cpd)
0.029
0.023
0.046
0.021
0.022
0.036
0.032
D2
Anova Post-Hoc Multiple Comparisons
p < 0.05 (HSD)
D3
Kruskal-Wallis Post-Hoc Multiple Comparisons
p < 0.05 (HSD)

Some extrastriate areas encode low spatial frequency information

We compared the mean preferred spatial frequency of each population of neurons from each area. We found a main effect of visual area on preferred spatial frequency (one-way ANOVA $F_{(6,1783)} = 59.7576$, $p < 0.0005$, one-way Kruskal-Wallis $p < 0.0005$). We followed up with post-hoc multiple comparisons tests to determine which areas were different from each in terms of preferred spatial frequency. Areas LM, AL, RL and AM all preferred spatial frequencies below the tuning of V1, whereas areas LI and PM could not be distinguished from V1 based on preferred spatial frequency ($p < 0.05$, Tukey-Kramer HSD). We also found differences between several extrastriate areas, and these results are summarized in Fig. 4.7.

Preferred spatial and temporal frequency tunings across areas are summarized in Fig. 4.9. A spectrum of combinations across the two dimensions is apparent, with area PM most similar to area V1 across both dimensions.

Extrastriate areas are more highly tuned for orientation

We compared the orientation selectivity index (OSI) of each population of neurons from each area. We found a main effect of visual area on orientation selectivity (one-way ANOVA $F_{(6,1783)} = 41.74$, $p < 0.0005$, one-way Kruskal-Wallis $p < 0.0005$). We followed up with post-hoc multiple comparisons tests to determine which areas were different from each in terms of orientation selectivity. All extrastriate visual areas investigated except area LI had significantly higher orientation tuning indices than V1 (LM, LI, AL, RL, AM; $p < 0.05$, Tukey-Kramer HSD). We

also found differences between several extrastriate areas, and these results are summarized in Fig. 4.8A.

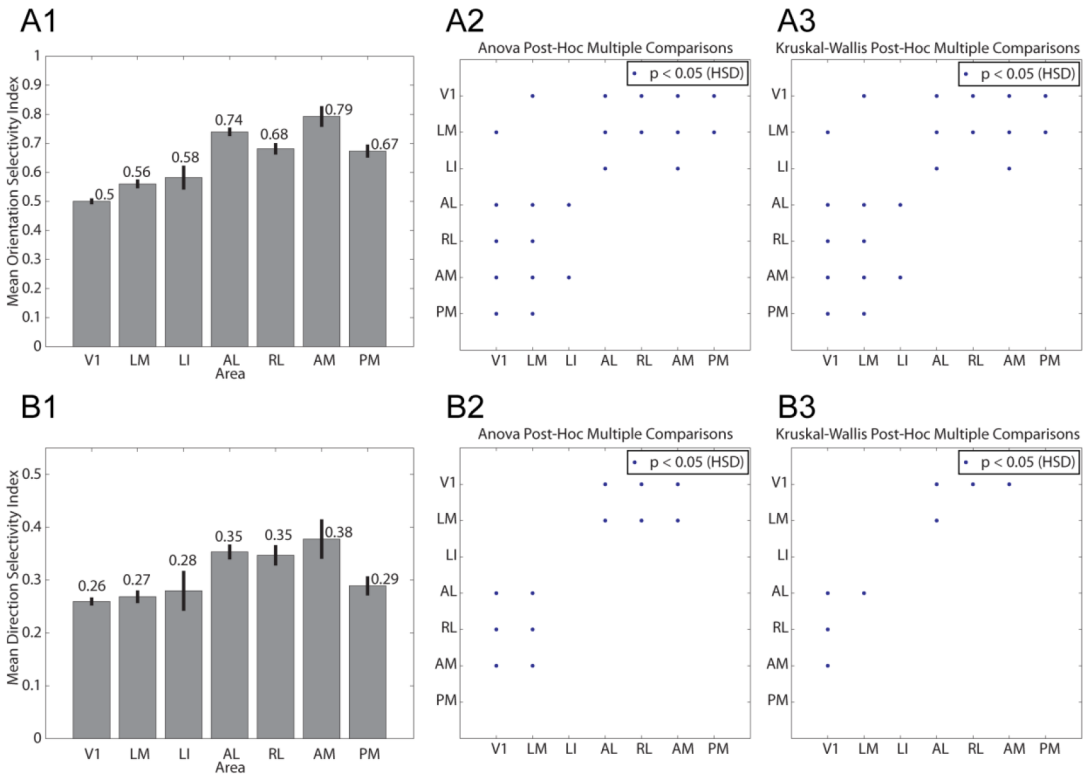

Figure 4.8 | Orientation and direction tuning across visual areas. A, Orientation tuning. Mean (A1) and post-hoc statistical comparisons from ANOVA (A2) and Kruskal-Wallis tests (A3). Areas LM, AL, RL, AM and PM had higher mean orientation selecivity indices (OSI) than V1. The ANOVA and Kruskal-Wallis post-hoc tests are in agreement and reveal additional distinctions between extrastriate visual areas in terms of mean OSI. B, Direction selectivity. Mean in direction selectivity index (DSI) for each area (B1), and post-hoc statistics (B2,B3). Areas AL, RL and AM are significantly higher in DSI than V1 and LM according to the ANOVA post-hoc comparisons (B2). Left panels (A1,B1) black lines are S.E.M., and numbers above bars are mean values. Middle panels (A2,B2) post-hoc pairwise comparisons following the highly significant one-way ANOVA. Right panels (A3,B3) post-hoc pairwise comparisons following the highly significant one-way Kruskal-Wallis test. Middle and right panels, blue dots represent significance at least at $p < 0.05$ after correcting for multiple comparisons using the Tukey-Kramer Honestly Significant Difference (HSD) correction.

Some extrastriate areas are more highly tuned for direction

We compared the direction selectivity index (DSI) of each population of neurons from each area. We found a main effect of visual area on direction selectivity (one-way ANOVA $F_{(6,1783)} = 10.45$, $p < 0.0005$, one-way Kruskal-Wallis $p < 0.0005$). We followed up with post-hoc multiple comparisons tests to determine which areas were different from each in terms of direction selectivity. Areas AL, RL and AM were all more highly tuned for direction than V1, whereas areas LM, LI and PM could not be distinguished from V1 based on direction tuning ($p < 0.05$, Tukey-Kramer HSD). Most extrastriate areas could not be distinguished from each other based on direction tuning. Only area LM was found to be significantly lower in DSI than areas AL, RL and PM following post-hoc comparisons from the ANOVA test ($p < 0.05$, Tukey-Kramer HSD) and only significantly lower than area AL following post-hoc comparisons from the Kruskal-Wallis test ($p < 0.05$, Tukey-Kramer HSD). These results are summarized in Fig. 4.8B.

Comparison of visual areas based on tuning bandwidth

We compared the bandwidths for temporal and spatial frequency for neurons which were bandpass for each parameter. Our sampling of the direction domain was insufficient to detect a difference in sharpness of tuning for orientation or direction between areas (data not shown), suggesting that all areas investigated have mean direction/orientation tuning width (half-width at half-maximum) of approximately equal to or less than 30°. For spatial frequency, we found a main effect of area on bandwidth (one-way ANOVA $F(6,903) = 15.23$, $p < 0.0005$, one-way Kruskal-Wallis

$p < 0.005$). All areas had sharper spatial frequency bandwidth tuning than V1, except for area LI ($p < 0.05$, Tukey-Kramer HSD). Areas AL, RL and AM had sharper spatial frequency bandwidth tuning than area LM by post-hoc comparisons following the ANOVA, while only area AM was found to be significantly lower in spatial frequency bandwidth than area LM by post-hoc comparisons following the Kruskal-Wallis test (Fig. 4.7B). We also found a main effect for area on temporal frequency bandwidth (one-way ANOVA $F(6,191) = 5.2$, $p < 0.005$, one-way Kruskal-Wallis, $p < 0.005$). Areas LM, AL and RL were found to have broader temporal frequency bandwidth than area V1 ($p < 0.05$, Tukey-Kramer HSD). We could not otherwise differentiate between extrastriate visual areas based on temporal frequency bandwidth (Fig. 4.6B).

We next compared the high and low cutoff frequencies for temporal frequency for each area. This included cells which were bandpass, or low or high pass depending on the parameter being tested (e.g., high cutoff measurements included bandpass cells and lowpass cells). We found a main effect of area on high cutoff temporal frequency (one-way ANOVA, $F_{(6,1013)} = 45.36$, $p < 0.0005$, one-way Kruskal-Wallis $p < 0.0005$). Mean high cutoff temporal frequencies of all extrastriate areas were higher than V1. Post-hoc comparisons between the areas revealed that LM, AL and RL had high-cutoff values which were significantly higher than V1 ($p < 0.05$, Tukey-Kramer HSD). Additional comparisons between extrastriate areas are summarized in Fig. 4.6C. We found a main effect of area on low cutoff temporal frequency (one-way ANOVA, $F_{(6,251)} = 2.89$, $p < 0.01$, one-way Kruskal-Wallis $p < 0.0005$). All extrastriate areas had higher mean low cutoff temporal frequencies than V1. Post-hoc comparisons from the one-way ANOVA revealed that only area LM had a significantly higher low cutoff

than V1 ($p < 0.05$, Tukey-Kramer HSD). However, post-hoc comparisons following from the one-way Kruskal-Wallis test revealed that areas LM, LI, AL and AM all had significantly higher low cutoff temporal frequencies. We could not otherwise differentiate the extrastriate areas from each other based on low cutoff temporal frequency (Fig. 4.6D).

Finally, we compared high and low cutoff spatial frequencies across visual areas. We found a main effect of area on high cutoff spatial frequency (one-way ANOVA, $F_{(6,1445)} = 27.55$, $p < 0.0005$, Kruskal-Wallis $p < 0.0005$). All extrastriate visual areas except area LI were found to have significantly different high cutoff spatial frequencies compared to V1 ($p < 0.05$, Tukey-Kramer HSD). Areas LM, AL, RL and AM had lower high cutoff spatial frequencies than V1, while area PM had significantly higher spatial frequency high cutoff than V1 and all other visual areas tested. However, area PM failed to show a significant difference compared to V1 in the post-hoc comparisons following the Kruskal-Wallis test, while maintaining its difference from all the other extrastriate visual areas. We found other significant differences between extrastriate visual areas in terms spatial frequency high cutoff, and they are summarized in Fig. 4.7C. We found a main effect of area on low cutoff spatial frequency (one-way ANOVA, $F_{(6,1205)} = 9.91$, $p < 0.0005$, Kruskal-Wallis $p < 0.0005$). Post-hoc comparisons between the areas revealed differences between pairs of the visual areas. Areas LM and AL were found to have significantly lower low cutoff spatial frequency than V1, while area LI had a significantly higher low cutoff ($p < 0.05$, Tukey-Kramer HSD). The post-hoc comparisons following the Kruskal-Wallis test were consistent, and also found that area PM had a significantly higher low spatial

frequency cutoff than area V1. Additional differences between extrastriate areas are summarized in Fig. 4.7D.

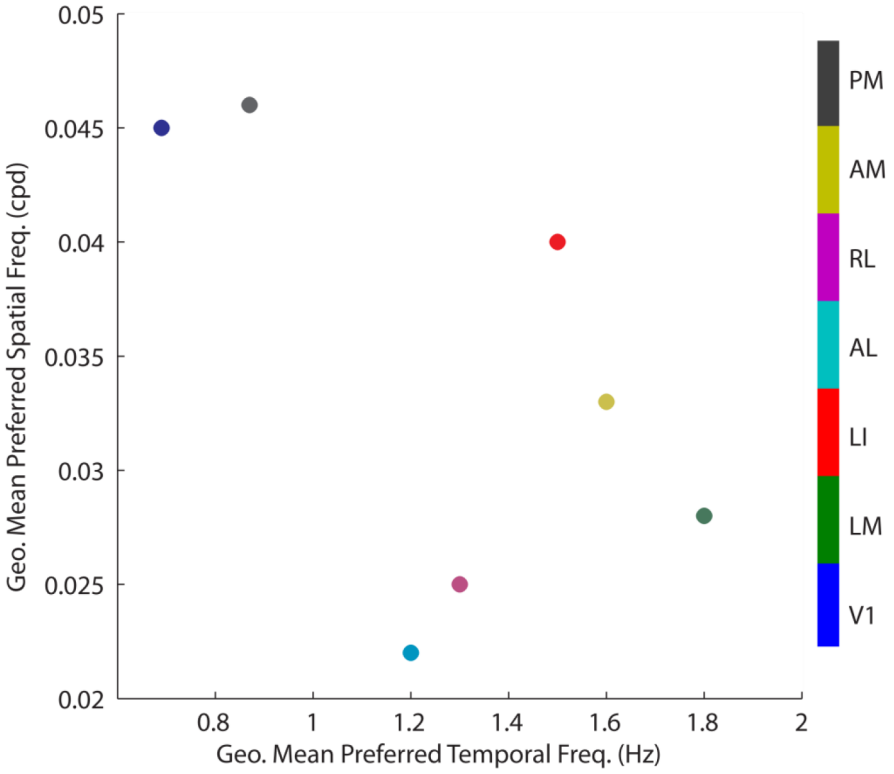

Figure 4.9 | Preferred spatial and temporal frequency tuning combinations by area. Visual areas represent a spectrum of mean preferred spatial and temporal frequency combinations. Area PM is generally most similar to area V1 along both dimensions.

Discussion

In the present study, we found that mouse cortex contains several orderly representations of visual space. By systematically stimulating the entire visual hemifield and measuring the brain's response using intrinsic optical and two-photon calcium imaging, we determined the retinotopic organization of mouse visual cortex at high resolution. This level of resolution revealed fine-scale details of the retinotopic map previously unknown based on electrophysiological techniques (Wagor et al., 1980; Wang and Burkhalter, 2007). We used the maps generated from our analysis, in combination with information from previous studies (Wang and Burkhalter, 2007; Kalatsky and Stryker, 2003) to attempt to draw borders around each visual area. While some areas were easily outlined based on complete and orderly visual field representations other cortical regions contained orderly representations of space, but not a complete representation. This effect has been shown in other species and visual areas with large receptive fields and with response properties preferring high-order features tend to increasingly represent the center of space, and not the periphery. Furthermore, visual areas have been shown to in rare cases, split their representation of space, such as along the horizontal meridian in the case of V2 in humans (Sereno et al., 1995).

Overall, the retinotopic map of mouse visual cortex we observed closely resembled the map predicted from V1 afferents (Wang and Burkhalter, 2007), and generally matched the coarse structure outlined using electrophysiology (Wagor et al., 1980). We confirmed several retinotopic map features (such as locations of vertical

and horizontal meridians, and peripheral representations) to outline as many as 9 of the 10 visual areas suggested by (Wang and Burkhalter, 2007). We found an orderly representation of visual space in the cortical location designated as A, however we did not observe key retinotopic features of the predicted map. Contrary to the prediction, we did not observe a vertical meridian extending from posterior to anterior along the medial side of the this cortical region, nor did we find a progression from upper to lower back to upper visual field running lateral to medial between area RL and the theoretical medial border of A. Interestingly, this cortical region was shown to have a markedly disorderly spatial pattern of V1 afferents (Wang and Burkhalter, 2007), and this may help explain the map discrepancy.

Aside from this distinction, the maps were strikingly similar, and for the sake of consistency in the literature, we chose to base our area border analysis on the map predicted previously (Wang and Burkhalter, 2007). This map is also easily related to other species such as the rat and squirrel, for which similar anatomical area names and structure have been described in the literature (Coogan and Burkhalter, 1993; Montero, 1993; Espinoza and Thomas, 1983; Wong and Kaas, 2008). It is important to point out that alternative valid interpretations of the retinotopic mapping data are likely, and future analyses incorporating additional functional and anatomical information may help reveal more accurate designations of mouse visual cortical areas. For example, in cases where a visual area is shown here to represent only a subregion of visual space, it is possible that its representation of the missing portion of visual space is miscategorized within another visual area. To help protect against this possibility, and to compare populations matched for eccentricity, we evaluated the

response properties of neuron populations from each area that represented the central 50% of retinotopic space (within the central 100°).

We recorded the response properties of dozens to over a thousand neurons in each of 7 visual areas. Each of these areas contained neurons which responded preferentially to at least one of the visual stimuli which we presented to the animal. Interestingly, the proportion of responsive neurons varied considerably between areas. This difference between areas may arise in part from the ability of the stimuli we used to drive responses in each area. For example, neurons in higher visual areas in the primate can be extremely selective for a specific stimulus containing higher-order features, and it is likely that the stimuli we used, while well-suited to drive responses in V1, may not be fully optimized to drive responses in many neurons in higher visual areas. Furthermore, it has also been shown that higher visual areas in other species are more susceptible to brain state fluctuations and influenced to a greater extent by anesthesia than lower visual areas. For the sake of comparison between areas, we limited our further analyses to neurons that responded reliably to at least one of the visual stimuli.

Overall, we found that the 6 extrastriate areas we investigated could be distinguished from V1 based on their population response characteristics along several dimensions. Furthermore, extrastriate areas had response characteristics which were different from each other.

All extrastriate areas had higher mean preferred temporal frequencies than V1, in some cases preferring up to almost 3 times the temporal frequency than V1. This difference was significant for all areas except area PM. Area PM was found to have

lower preferred temporal frequency tuning than areas LM, AL and RL. LM had the highest preferred temporal frequency tuning, and this difference was significant compared to extrastriate areas AL and PM. Larger sample sizes for areas LI and AM may have improved our ability to detect significant differences for other comparisons. Despite this, it appears that extrastriate visual cortex is much better suited to compute high temporal frequency motion information than V1. It is striking that extrastriate areas can respond to such high temporal frequency information, when neurons in V1 are so rare to respond at these frequencies. The high cutoff temporal frequency for the population of V1 barely overlaps with the mean preferred temporal frequency of many of the extrastriate areas. Furthermore, the high cutoff temporal frequencies for several extrastriate areas far exceed frequencies encoded in V1. In fact, some extrastriate areas have low cutoff values that are higher than the mean preferred temporal frequency for V1. Tuning for temporal frequency was in general broader in extrastriate areas, reflecting responses to additional high frequencies which V1 rarely responded to.

Results were more mixed for spatial frequency tuning. It appeared that at least two groups of areas could be distinguished based on preferred spatial frequency tuning: those which preferred spatial frequencies comparable to V1 (LM, AL, RL and AM), and those with spatial frequency tuning of about half the acuity of V1 (LI and PM). This grouping of areas was also supported by significant differences between these areas in pairwise comparisons. Following from these results it was also possible to characterize areas LM and AM as having higher preferred spatial frequency tuning than area AL. Thus area AL appeared to have the lowest spatial frequency tuning of all of the areas. These results are particularly interesting considering the fact that

receptive field size increases in extrastriate areas compared to V1 (Wang and Burkhalter, 2007), and yet some of the areas with relatively large receptive fields are still able to maintain comparably high spatial frequency tuning, perhaps by integrating to form complex receptive fields. All areas except LI had sharper spatial frequency tuning than V1, and some extrastriate areas had sharper tuning than others. In this case, this result is opposite to the temporal frequency tuning bandwidth between extrastriate cortex and V1, and likely reflects a smaller range of spatial frequencies encoded in the extrastriate areas which had lower preferred spatial frequency and lower high cutoff spatial frequencies.

Orientation selectivity and to a lesser extent direction selectivity increased in extrastriate cortex compared to V1. This result likely reflects local circuit inhibitory mechanisms, or selective wiring between V1 and extrastriate areas. The differences between extrastriate areas along these dimensions may provide insight into where these inhibitory influences may be more pronounced, and/or which areas are higher in the hierarchy than other areas, since at each stage in the hierarchy, orientation tuning may be sharpened further by local mechanisms.

Conclusion

We found unique and orderly representations of visual space in the mouse visual cortex. Furthermore, we were able to distinguish between visual areas based on their response properties along several stimulus dimensions including temporal frequency, spatial frequency and orientation and direction tuning. Areas also showed differences in the sharpness in tuning of some of these parameters. These results

demonstrate that the mouse visual cortex, like other species, processes distinct types of visual information in different visual areas. The application of genetic technologies to unravel the microcircuits underlying these selective computations may provide further insight into fundamental circuit mechanisms for visual information processing. The results presented here functionally characterizing mouse extrastriate areas, as well as the methods developed and demonstrated here to efficiently and systematically evaluate mouse cortical visual areas, may greatly help direct and accomplish these future studies.

Methods

Animal Preparation and Surgery

All experiments involving living animals were approved by the Salk Institute's Institutional Animal Care and Use Committee. All experiments were performed using C57BL/6 mice (n = 47) between 2 and 3 months of age. Surgical plane anesthesia was induced and maintained by isoflurane (2-2.5% induction, 1-1.25% surgery). Dexamethasone and carprofen were administered subcutaneously (2 mg/kg and 5 mg/kg respectively), and ibuprofen (30 mg/kg) was administered post-operatively in the drinking water for the duration of the experiment (typically 1-2 days). A custom made metal frame was mounted to the skull, centered on the visual cortex of the left hemisphere using stereotaxic coordinates. The frame was mounted so that it was as close the skull as possible, tilted to be tangent to the brain surface. The angle of tilt was recorded using a digital protractor by measuring the tilt of the stereotaxic frame

(Narishige) used to parallelize the frame relative to the table. The skull overlying visual cortex was carefully thinned with a dental drill, stopping often and rinsing with chilled artificial cerebral spinal fluid (ACSF, in mM: 125 NaCl, 10 d-glucose, 10 HEPES, 3.1 $CaCl_2$, 1.3 $MgCl_2$; or 150 NaCl, 2.5 KCl, 10 HEPES, 2 $CaCl_2$, 1 $MgCl_2$). Great care was taken to prevent overheating of the brain or subdural bleeding. The bone was thinned just passed the spongy middle layer which often contained blood vessels. The resultant preparation was a thin layer of semi-flexible bone free of blood vessels. This was especially relevant for alignment of cortical blood vessel landmarks and functional retinotopic maps. After the surgery, chloprothixene (2.5 mg/kg) was administered intramuscularly and isoflurane was reduced to 0.25-0.8%, for visual stimulation and recording experiments. The most robust visual responses coincided with higher respiration rates when the animal appeared to be lightly anesthetized.

Intrinsic Signal Optical Imaging

The intrinsic signal imaging protocol was adapted from a previous study (Kalatsky and Stryker, 2003). All other relevant modifications are described elsewhere in the text.

Dye Loading and Two-Photon Imaging

The retinotopic map from the intrinsic signal imaging experiment aligned and overlayed on an image of the cortical blood vessels was used as a reference for targeting the locations of calcium-sensitive dye loading. The dye solution contained 1mM Oregon Green Bapta-1 AM (OGB, Invitrogen) with 10% DMSO and Pluronic

F-127 in ACSF (Stosiek et al., 2003; Ohki et al., 2005). The solution also included 50 μM sulforhodamine-101 to selectively label astrocytes (Nimmerjahn et al., 2004). The pipette (3-5 μm outer diameter tip) was lowered diagonally (30° from horizontal) to 225 μm below the dura surface (layer 2/3) while short pulses of pressure were applied to the back of the pipette to keep the tip clear of debris. Then, a single pulse of 1 min duration and 10 PSI was applied for the loading protocol. This typically resulted in approximately 0.5-1 mm of OGB loading. The loading was observed under epifluorescence to confirm sufficient dye injection. In most cases, several locations were injected in the same animal often using the same pipette multiple times, resulting in an area of OGB loading spanning up to several millimeters. Each loading site was separated by approximately 0.5-1mm. At least one hour after the last loading the two-photon imaging began.

A custom-built Movable Objective Microscope (Sutter) coupled to a Chameleon Ultra II mode-locked Ti:Sapphire laser (Coherent) was used for two-photon imaging. Standard wavelength for two-photon microscopy was 920-950 nm. A waveplate (Newport) was used in conjunction with a beamsplitter cube (Newport) to modulate the power of the excitation laser light. A 16X water-immersion objective (Nikon) was used for large-field retinotopy experiments, and a 40X water-immersion objective (Olympus) was used to measure cellular responses. Fluorescent light was detected by photomultiplier tubes (Hamamatsu), after being filtered by one of two emission filter sets: HQ535/50, and HQ610/75 (Chroma). A third acquisition channel was used to record the precise stimulus timing relative to image acquisition using a photodiode to detect a brief pulse of light at each cycle of the periodic visual stimulus

(e.g., drifting bar retinotopy stimulus), in addition to the stimulus beginning and end. ScanImage software (Pologruto et al., 2003) was used for image acquisition and images and time lapse videos were processed offline in Matlab (MathWorks) and ImageJ (http://rsbweb.nih.gov/ij/). Imaging experiments were performed at ~130-180 μm below the dura surface (layer 2/3). For retinotopy experiments, images were typically acquired at approximately 2 Hz (256 x 256 pixel frames, unidirectional scanning, ~800 x 800 μm field of view for wide-field imaging). For image cellular responses, images were typically acquired at approximately 8 Hz (256 x 256 pixel frames, bidirectional scanning, either ~150 x 150 μm or ~300 x 300 μm field of view). After each experiment in a given location, a stack of images (5 μm z step) was taken starting at the experiment image plane and ending above the dura in order to determine the precise depth of the experiment offline. Images were taken of the aligned overlying surface blood vessel pattern in order to register images taken during experiments with the 40X objective with those with the 16X objective, and with the intrinsic imaging experiments. High-resolution images (1024 x 1024 pixel frames) were often taken of the experiment imaging plane as an anatomical reference of the cells recorded.

Visual Stimulation

Drifting bar and drifting grating stimuli were displayed on a gamma-corrected, large LCD display (68 x 121 cm, 120 Hz monitor, stimulus presented at 60Hz), rotated in 'portrait' mode such that monitor was taller than it was wide. The screen was placed so as to stimulate the entire known visual hemi-field of the mouse (at most -40°

to 70° lower to upper and -70° to 70° nasal to temporal (Wagor et al., 1980), when defining the horizontal meridian (0° altitude) as a plane passing through the center of the eyes parallel to the ground, and defining 0° azimuth as the coronal plane passing through the center of the eye). The screen was tilted to match the tilt of the animal relative to its normal position around its anteroposterior axis. The screen was placed at an angle of 25° relative to the animal around its dorsoventral axis such that the screen was pointed in slightly toward animal's nose (i.e., to stimulate the nasal periphery). A perpendicular bisector was defined as the origin of the line perpendicular to the screen that intersected with the center of the animal's eye. This point on the screen defined the center of the stimulus and was slightly anterior to the 0° azimuth plane. The screen was raised so that the perpendicular bisector was 28 centimeters from the bottom of the screen, centered on the screen left to right, and 10 cm from the animal. This positioning of the monitor, in conjunction with the spherical stimulus correction described below, accurately simulated a hemispherical display around the mouse (the screen covered >140° of the nasal to temporal field and >110° lower to upper field). Furthermore, it was beyond the theoretical point of 'infinite focus' of the mouse eye (Remtulla and Hallett, 1985; Green et al., 1980; de la Cera et al., 2006) leading to similar focus at all points on the screen. Absolute eccentricity coordinates were rotated relative to stimulus coordinates as described in the Data Analysis section in order to follow the convention for the mouse visual hemifield described above (i.e., the 0° azimuth plane was rotated slightly from the plane through the perpendicular bisector that defined the center of the stimulus).

For retinotopy experiments, a periodic drifting bar stimulus was used (Kalatsky and Stryker, 2003). The bar was 20° wide and subtended the whole visual hemifield along either the vertical or horizontal axis. The bar was drifted 10 times in each of the four cardinal directions. Azimuth correction was used for the bar drifting along the horizontal axis and altitude correction was used for the bar drifting along the vertical axis (see below), in order to define eccentricity using standard spherical coordinates. By drifting the bar in both directions along an axis it was possible to subtract the delay in the intrinsic signal relative to neural activity (Kalatsky and Stryker, 2003); see Data Analysis). The bar drifted at 8.5-9.5°/s for intrinsic imaging experiments and at 12-14°/s for two-photon imaging experiments. The stimulus was generated to be larger than the display (155° wide x 173° tall), preventing the periodic drifting bar stimulus from stimulating two points in space simultaneously.

For drifting grating experiments, sinusoidal drifting gratings were used. For each population of neurons imaged (a single 40X imaging plane), we presented with rare exceptions four sets of stimuli: a temporal frequency varying experiment (0.5, 1, 2, 4 and 8 Hz, 8 directions plus blank, ~0.04 cpd, 5 repeats pseudorandomized for each parameter combination), a spatial frequency varying experiment (0.01, 0.02, 0.04, .08 and 0.16 cpd, 8 directions plus blank, ~1 Hz, 5 repeats pseudorandomized for each parameter combination), a 12 direction orientation tuning experiment (~1 Hz, ~0.04 cpd, 5 repeats pseudorandomized for each parameter combination and a blank condition), and a drifting bar retinotopy experiment (same as for the large-field 16X retinotopy experiments) to map the precise eccentricity of each neuron in the field of view. Stimulus durations were 4 sec for the temporal frequency experiment and 2 sec

for the spatial frequency and 12 direction experiments. Population data from previous experiments in each area and from published data from V1 (e.g., Niell and Stryker, 2008) were used to determine the value for the parameters held constant in each experiment in an effort to strongly stimulate as large a population as possible, and keep parameters consistent across visual areas. An altitude correction was used to account for the spherical distortion of the flat monitor. This correction held the spatial frequency and temporal frequency constant throughout the visual field.

Spherical corrections were applied to all stimuli in order to account for the distortions created by displaying stimuli to the animal on a flat monitor. Without correction, the spatial frequency and temporal frequency of a drifting grating varies exponentially with eccentricity—a problem present in any study using a flat screen, but especially pronounced in a our study which used a very large screen. Drifting bar and grating stimuli were generated through custom routines in Psychtoolbox and Matlab and then transformed with spherical projection.

Data Analysis

Intrinsic optical imaging retinotopy data were analyzed as previously described (Kalatsky and Stryker, 2003). Briefly, data were acquired in a continuous block during stimulus presentation of a bar drifting in one direction periodically. A Fourier transform was taken of the entire data block and the amplitude was recorded for the frequency present in the cortical intrinsic signal that matched the frequency of the periodic drifting bar stimulus. The phase difference between the signal measured at this frequency at a single pixel and the phase of the stimulus was used to determine the

position of the stimulus in space that drove the largest amplitude response in the intrinsic signal. Contrasting this phase difference with the data from the bar drifting in the opposite direction along the same axis made it possible to estimate the center point between them, accounting for the hemodynamic delay, and thus determining the best estimate of the position in space that the cortical location responded to. A comparable approach was used to analyze Ca^{2+} imaging retinotopy experiments. Data in terms of phase were converted to eccentricity by dividing the known angle covered by the stimulus by the total degrees of phase.

Eccentricity values were rotated to follow the convention described in Visual Stimulation by first transforming the data into Cartesian coordinates, rotating the data using standard matrix rotation, and then converting the data back to spherical coordinates. This transformation does not warp the data in any way, and any arbitrary transformation/rotation can be accomplished using this method.

For population analyses of cellular responses to drifting gratings, data were preprocessed in the following ways. The first image of each trial of the first and all subsequent experiments was registered with the mean image of the first trial of the first experiment in a given field of view by determining the least squares error of the crosscorrelation between the images, and then the same transformation was applied to the remaining images in each trial. Then regions of interest (ROIs) around each cell in the image were created using a semi-automated procedure, separately for the OGB channel (neurons and glia) and the sulfarhodamine-101 channel (glia). Candidate ROIs were determined by thresholding the z-scored image of the mean image of the first trial of the first experiment in a field of view. Then ROIs were carefully edited

manually for both channels. Glia cells were removed from the analysis of the OGB channel by removing any ROIs in the OGB channel that overlapped with ROIs marked in the glia channel. The remaining ROIs in the OGB channel were neurons, and each ROI was given a unique number corresponding to each unique neuron. This ROI and unique identifier referenced the same neuron throughout the entire imaging session of the same field of view (spanning several experiments) and allowed us to compare data for the same neuron across several experimental manipulations.

The baseline calcium fluorescence signal was averaged within each cell ROI for each trial during a prestimulus period (1 sec). Then, the entire time course was converted from absolute fluorescence values to baseline subtracted values by the following equation: $\Delta\mathbf{F/F} = \mathbf{F_I\text{-}F/F}$, where $\Delta F/F$ is the change in fluorescence relative to baseline, F_I is the instantaneous fluorescence signal and F is the baseline fluorescence. The $\Delta F/F$ response for each was averaged during the stimulus time window (2 sec) for each trial, and the mean and standard deviation across trials for each stimulus and blank condition were computed for each neuron. We applied several criteria for included neurons in further population analyses. Neurons were deemed visually responsive if they gave a mean response above 6% $\Delta F/F$ to any of the stimuli. Neurons were deemed reliable if they met the following criteria: mean response to stimulus - standard deviation of response to stimulus > mean response to blank stimulus + standard deviation of response to blank stimulus. Finally, neuron eccentricity mapped with the retinotopy stimulus was used to restrict our population analyses to eccentricity-matched neurons within the central 100° of space. The number of neurons which met all of these criteria were used as the denominator in all

subsequent analyses of fraction of neurons exhibiting a particular score on a given parameter.

Tuning Metrics

Temporal and spatial frequency tuning curves were taken at the optimal orientation and direction for each neuron, using the average ΔF/F response for each condition across trials. These tuning curves were fit with a Difference of Gaussians function (as in Wong and Kaas, 2008). A $\log_2$ transform was performed on the curve, converting it to the octave ($\log_2$) scale. The preferred frequency was taken as the peak (maximum) of this function. For bandwidth and low and high cutoff measurements, each cell was characterized as either bandpass, highpass or lowpass for temporal and spatial frequency based on whether its minimum and/or maximum frequency response passed below the half max for the tuning curve. The high cutoff was computed for bandpass and lowpass cells as the highest frequency which drove a half-max response. Low cutoff was computed for bandpass and highpass cells as the lowest frequency which drove a half-max response. Bandwidth was measured for bandpass cells as the difference between high cutoff and low cutoff.

The orientation and direction tuning curves were taken at the optimal spatial frequency for each neuron, using the average ΔF/F response for each condition across trials. The orientation selectivity index (OSI) was computed as the maximum response of the neuron – the response to the orthogonal orientation/maximum response of neuron + the response to the orthogonal orientation. The direction selectivity index was computed as the maximum response of the neuron – the response to the opposite

direction/maximum response of neuron + response to opposite direction. The half-width at half-maximum (HWHM) was computed for each neuron orientation and direction tuning curves but our results suggested that we did not adequately sample the direction domain to make comparisons based on these measurements.

Statistics

We started with the most basic question: are mouse cortical visual areas distinguishable based on population tuning metrics? We asked this question statistically using a multivariate analysis of variance (MANOVA) on the four values we computed for every neuron in our sample from each area: preferred temporal frequency, preferred spatial frequency, orientation selectivity index and direction selectivity index. We also computed bandwidth and high and low cutoff metrics for each population, however not every neuron received a value for all of these metrics and thus we excluded these metrics from the multivariate analysis. We followed up this analysis with individual univariate analyses to confirm whether there was a main effect of area on each of our dependent variables (both one-way ANOVA and one-way Kruskal-Wallis tests). Finally, for each significant one-way test, we performed post-hoc pairwise comparisons to determine which areas were different from each other in terms of each metric, correcting the p value for multiple comparisons using the Tukey-Kramer Honestly Significant Difference (HSD).

Acknowledgements

We thank members of the Callaway lab for useful discussions and support. We acknowledge support from NIH grants EY01742 (EMC) and EY019821 (IN), and from a training grant from the Institute for Neural Computations at UCSD (MEG).

Publication Acknowledgements

Chapter 4, in full, is being prepared for submission for publication of the material. Marshel, J.H., Garrett, M.E., Nauhaus, I., & Callaway, E.M. (In Preparation). Retinotopic and receptive field characterization of mouse striate and extrastriate visual cortex. The dissertation author was the co-primary investigator and co-author of this paper.

Van den Bergh, G., Zhang, B., Arckens, L., and Chino, Y. M. (2010). Receptive-field properties of V1 and V2 neurons in mice and macaque monkeys. J. Comp. Neurol *518*, 2051-2070.

Bock, D. D., Lee, W.-C. A., Kerlin, A. M., Andermann, M. L., Hood, G., Wetzel, A. W., Yurgenson, S., Soucy, E. R., Kim, H. S., and Reid, R. C. (2011). Network anatomy and in vivo physiology of visual cortical neurons. Nature *471*, 177-182.

Briggman, K. L., Helmstaedter, M., and Denk, W. (2011). Wiring specificity in the direction-selectivity circuit of the retina. Nature *471*, 183-188.

Callaway, E. M. (2004). Feedforward, feedback and inhibitory connections in primate visual cortex. Neural Netw *17*, 625-632.

de la Cera, E. G., Rodríguez, G., Llorente, L., Schaeffel, F., and Marcos, S. (2006). Optical aberrations in the mouse eye. Vision Res *46*, 2546-2553.

Chow, B. Y., Han, X., Dobry, A. S., Qian, X., Chuong, A. S., Li, M., Henninger, M. A., Belfort, G. M., Lin, Y., Monahan, P. E., et al. (2010). High-performance genetically targetable optical neural silencing by light-driven proton pumps. Nature *463*, 98-102.

Coogan, T. A., and Burkhalter, A. (1993). Hierarchical organization of areas in rat visual cortex. J. Neurosci *13*, 3749-3772.

Espinoza, S. G., and Thomas, H. C. (1983). Retinotopic organization of striate and extrastriate visual cortex in the hooded rat. Brain Res *272*, 137-144.

Felleman, D. J., and Van Essen, D. C. (1991). Distributed hierarchical processing in the primate cerebral cortex. Cereb. Cortex *1*, 1-47.

Green, D. G., Powers, M. K., and Banks, M. S. (1980). Depth of focus, eye size and visual acuity. Vision Res *20*, 827-835.

Kalatsky, V. A., and Stryker, M. P. (2003). New paradigm for optical imaging: temporally encoded maps of intrinsic signal. Neuron *38*, 529-545.

Kerlin, A. M., Andermann, M. L., Berezovskii, V. K., and Reid, R. C. (2010). Broadly tuned response properties of diverse inhibitory neuron subtypes in mouse visual cortex. Neuron *67*, 858-871.

Liu, B.-hua, Li, P., Li, Y.-tang, Sun, Y. J., Yanagawa, Y., Obata, K., Zhang, L. I., and Tao, H. W. (2009). Visual receptive field structure of cortical inhibitory neurons revealed by two-photon imaging guided recording. J. Neurosci *29*, 10520-10532.

Luo, L., Callaway, E. M., and Svoboda, K. (2008). Genetic dissection of neural circuits. Neuron *57*, 634-660.

Marshel, J. H., Mori, T., Nielsen, K. J., and Callaway, E. M. (2010). Targeting single neuronal networks for gene expression and cell labeling in vivo. Neuron *67*, 562-574.

Maunsell, J. H., and Newsome, W. T. (1987). Visual processing in monkey extrastriate cortex. Annu. Rev. Neurosci *10*, 363-401.

Montero, V. M. (1993). Retinotopy of cortical connections between the striate cortex and extrastriate visual areas in the rat. Exp Brain Res *94*, 1-15.

Movshon, J. A., and Newsome, W. T. (1996). Visual response properties of striate cortical neurons projecting to area MT in macaque monkeys. J. Neurosci *16*, 7733-7741.

Nassi, J. J., and Callaway, E. M. (2009). Parallel processing strategies of the primate visual system. Nat. Rev. Neurosci *10*, 360-372.

Niell, C. M., and Stryker, M. P. (2008). Highly selective receptive fields in mouse visual cortex. J. Neurosci *28*, 7520-7536.

Nimmerjahn, A., Kirchhoff, F., Kerr, J. N. D., and Helmchen, F. (2004). Sulforhodamine 101 as a specific marker of astroglia in the neocortex in vivo. Nat. Methods *1*, 31-37.

Ohki, K., Chung, S., Ch'ng, Y. H., Kara, P., and Reid, R. C. (2005). Functional imaging with cellular resolution reveals precise micro-architecture in visual cortex. Nature *433*, 597-603.

Olavarria, J., Mignano, L. R., and Van Sluyters, R. C. (1982). Pattern of extrastriate visual areas connecting reciprocally with striate cortex in the mouse. Exp. Neurol *78*, 775-779.

Orban, G. A. (2008). Higher order visual processing in macaque extrastriate cortex. Physiol. Rev *88*, 59-89.

Petreanu, L., Huber, D., Sobczyk, A., and Svoboda, K. (2007). Channelrhodopsin-2-assisted circuit mapping of long-range callosal projections. Nat. Neurosci *10*, 663-668.

Pologruto, T. A., Sabatini, B. L., and Svoboda, K. (2003). ScanImage: flexible software for operating laser scanning microscopes. Biomed Eng Online *2*, 13.

Remtulla, S., and Hallett, P. E. (1985). A schematic eye for the mouse, and comparisons with the rat. Vision Res *25*, 21-31.

Runyan, C. A., Schummers, J., Van Wart, A., Kuhlman, S. J., Wilson, N. R., Huang, Z. J., and Sur, M. (2010). Response features of parvalbumin-expressing interneurons suggest precise roles for subtypes of inhibition in visual cortex. Neuron *67*, 847-857.

Sereno, M. I., Dale, A. M., Reppas, J. B., Kwong, K. K., Belliveau, J. W., Brady, T. J., Rosen, B. R., and Tootell, R. B. (1995). Borders of multiple visual areas in humans revealed by functional magnetic resonance imaging. Science *268*, 889-893.

Sereno, M. I., McDonald, C. T., and Allman, J. M. (1994). Analysis of retinotopic maps in extrastriate cortex. Cereb. Cortex *4*, 601-620.

Sohya, K., Kameyama, K., Yanagawa, Y., Obata, K., and Tsumoto, T. (2007). GABAergic neurons are less selective to stimulus orientation than excitatory neurons in layer II/III of visual cortex, as revealed by in vivo functional Ca2+ imaging in transgenic mice. J. Neurosci *27*, 2145-2149.

Stosiek, C., Garaschuk, O., Holthoff, K., and Konnerth, A. (2003). In vivo two-photon calcium imaging of neuronal networks. Proc. Natl. Acad. Sci. U.S.A *100*, 7319-7324.

Wagor, E., Mangini, N. J., and Pearlman, A. L. (1980). Retinotopic organization of striate and extrastriate visual cortex in the mouse. J. Comp. Neurol *193*, 187-202.

Wall, N. R., Wickersham, I. R., Cetin, A., De La Parra, M., and Callaway, E. M. (2010). Monosynaptic circuit tracing in vivo through Cre-dependent targeting and complementation of modified rabies virus. Proc. Natl. Acad. Sci. U.S.A *107*, 21848-21853.

Wang, Q., and Burkhalter, A. (2007). Area map of mouse visual cortex. J. Comp. Neurol *502*, 339-357.

Wong, P., and Kaas, J. H. (2008). Architectonic subdivisions of neocortex in the gray squirrel (Sciurus carolinensis). Anat Rec (Hoboken) *291*, 1301-1333.

APPENDIX

FUNCTIONAL AND STRUCTURAL ANALYSIS OF THE MONOSYNAPTIC INPUTS FROM AREA V1 TO AREA AL IN MOUSE VISUAL CORTEX USING A MODIFIED RABIES VIRUS ENCODING GCAMP3

Summary

In order to study the structure and function of inputs to specific brain areas, we developed and applied a method for anatomically mapping and measuring the response properties of the monosynaptic inputs to a given extrastriate visual area in the mouse (area AL). We found a collection of neurons in area V1 corresponding to the same retinotopic location as where we injected a novel monosynaptic, retrograde tracing rabies virus in area AL. The virus was modified to encode the genes for GCaMP3, a genetically-encoded calcium indicator, and DsRedX, a red fluorescent marker protein. Using *in vivo* two-photon imaging, we imaged the labeled neurons up to well over 1 mm deep in V1, including deep layer pyramidal cells. We characterized the orientation and direction tuning of these imaged neurons, and of several of their dendrites up to over 500 μm below the pia surface, by presenting visual stimuli to the animal (drifting square-wave gratings) and recording the calcium dynamics within neurons related to neuronal spiking using the fluorescent signal from the GCaMP3. Input neurons to AL found in V1 were highly selective for direction and orientation. This method may be used to characterize the fine-scale structure and function of neurons providing monosynaptic input to virtually any starting brain area. This may help shed light on the patterns of functional-connectivity subserving specialized information processing by diverse brain areas. Furthermore, extensions of this novel technology could make it compatible with genetic targeting strategies to label and record the activity of inputs to specific cell types and single neurons.

Results

Monitoring of neural activity with genetically-encoded calcium indicators

Genetically-encoded calcium indicators enable neuroscientists to examine the function of genetically-defined neuronal populations (Luo et al., 2008; Miyawaki, 2005; Tian et al., 2009). To facilitate studies linking circuit structure and function, we produced G-deleted rabies viruses expressing the genetically-encoded calcium sensor GCaMP3 (Tian et al., 2009). As described above for viruses expressing fluorescent proteins, we produced two new rabies virus variants encoding GCaMP3. The first of these viruses expresses only GCaMP3 in place of B19G (SADΔG-GCaMP3), while the second expresses both GCaMP3 and DsRedX (SADΔG-GCaMP3-DsRedX). We recovered and amplified both SADΔG-GCaMP3 and SADΔG-GCaMP3-DsRedX in B7GG cells under 35°C, 3% CO_2 conditions, and concentrated the viruses for *in vivo* injection. Again, titers of these viruses were indistinguishable from viruses encoding GFP only. To test whether SADΔG-GCaMP3 is functional, we stereotaxically injected concentrated SADΔG-GCaMP3 into the V1 of mice and later analyzed visual responses of GCaMP3-expressing V1 neurons *in vivo* using two-photon imaging. **Supplementary Figure A.1A** shows an anatomical reconstruction of a selected V1 neuron imaged *in vivo* 11 days after infection. Drifting gratings were presented in 8 directions in 45 degree orientation steps in random order. Fluorescence changes in the same cell were monitored during presentation of visual stimuli. As illustrated in **Supplementary Figures A.1B and A.1C**, visual stimulation resulted in robust increases in fluorescence, the strength of which depended on the grating orientation.

(A movie of the response to the preferred orientation is available as **Supplementary Movie A.1**). These results are similar to those described in mouse V1 using the calcium indicator dye Oregon Green BAPTA (OGB), but the percent changes in fluorescence are much greater than are typically observed with indicator dyes (Kerlin et al., 2010; Runyan et al., 2010).

Although SADΔG-GCaMP3 proved to be effective for monitoring activity of infected neurons, the numbers of infected neurons that could be identified during *in vivo* 2-photon imaging was lower than expected from subsequent post-mortem examination (data not shown). We suspected that the difficulty in identifying infected neurons *in vivo* resulted from relatively dim baseline fluorescence, as expected from the dependence of fluorescent intensity on baseline calcium levels (Kerlin et al., 2010; Kerr et al., 2005; Ohki et al., 2005; Runyan et al., 2010). Therefore, to facilitate *in vivo* identification of infected neurons, we used SADΔG-GCaMP3-DsRedX in subsequent studies, and first searched for expression of DsRedX before subsequent characterization of functional responses based on the co-expression of GCaMP3. Furthermore, to allow functional characterization of an identified subset of V1 neurons making connections to another visual cortical area, we injected the SADΔG-GCaMP3-DsRedX into the lateral extrastriate cortical area AL of mice and assessed visual responses of retrogradely infected neurons in V1.

Injection of rabies virus into AL, subsequent identification of V1 and alignment of 2-photon imaging with the expected location of retrogradely-infected neurons was facilitated by intrinsic signal imaging to map retinotopy in V1 (**Figure A.1A**) ((Kalatsky and Stryker, 2003), see Methods for further details.). Nine days after

virus infection, blood vessel patterns were used to select a location in V1 expected to provide input to the virus injection location in AL (**Figure A.1A**). Two-photon imaging at wavelengths sensitive to detection of DsRedX revealed a large field of infected neurons in V1. Remarkably, infected neurons could be clearly visualized to depths of more than a millimeter below the pial surface of the cortex (**Figure A.1B**; The stack movie of SADΔG-GCaMP3-DsRedX-infected neurons in the V1 is available as **Supplementary Movie A.3**.), far deeper than is typically possible with imaging using OGB (Kerlin et al., 2010; Kerr et al., 2005; Ohki et al., 2005; Runyan et al., 2010). GCaMP3 was also visualized in all DsRedX-positive cells and processes (**Figure A.1B**).

We next selected planes of interest in the Z-axis for imaging of visually evoked functional changes in GCaMP3 fluorescence. **Figure A.1C** shows anatomical images at a depth of 370 μm from the pial surface, while **Figures A.1D and A.1E** illustrate fluorescence changes of GCaMP3 in selected cell bodies or dendrites in response to visual stimuli. For visual stimulation, square-wave gratings were drifted at 12 directions in 30 degree orientation steps in random order. Infected V1 neurons exhibited significant increases in the GCaMP3 fluorescence at particular grating orientations. The two neuronal somata illustrated had direction selective visual responses (**Figures A.1D1 and A.1D2;** A movie of the response to the preferred orientation in **Figure A.1D1** is available as **Supplementary Movie A.3**). Interestingly, orientation selective responses were also detected from GCaMP3-labeled dendrites (**Figures A.1D3 and A.1D4**). It is likely that the combination of high expression levels and sparse labeling with GCaMP3 (compared to dense OGB

labeling), contribute importantly to the ability to determine visual responses of distinct neuronal processes.

The surprisingly clear label that could be observed in neurons deep in the cortex suggested that these reagents might make it possible to also measure their visual responses. We therefore selected additional imaging planes at 520-535 μm below the pial surface and assayed orientation selectivity of fluorescence changes from labeled neurons in deeper cortical layers (**Supplementary Figure A.2A-A.2F**). We obtained clear changes in the GCaMP3 fluorescence in response to the preferred directions, comparable to those typically observed in more superficial layers. However, unlike in superficial layers, fluorescence changes could be observed in identified neuronal cell bodies but not in dendritic processes. This likely reflects weaker fluorescence in the dendrites versus cell bodies and poorer imaging signal at greater depths.

To demonstrate the prolonged viability and visual responsiveness of rabies-infected neurons, the same animal was imaged again 2 days later, 11 days after the initial rabies injection into AL. Although we did not attempt to identify the same neurons that were imaged at 9 days, we again identified a field of DsRedX-expressing neurons and monitored their visual responses based on changes in GCaMP3 fluorescence. We performed the same set of experiments as described above to obtain orientation selectivity tuning curves on day 9 (**Supplementary Figure A.2G-A.2L**). The infected cells in the V1 showed robust orientation selective fluorescence changes on day 11 from both GCaMP3-labeled soma and GCaMP3-labeled dendrites at a depth of 370 μm.

From these results, we conclude that rabies virus-mediated expression of GCaMP3 can be used to monitor activity of neurons targeted based on their connections to more distant neurons. Fluorescence changes can be monitored *in vivo* at either the soma or the dendrites, at depths greater than 500 μm, and virus infection does not prevent functional characterization even 11 days post-infection.

Figure A.1 | Monitoring of neural activity with GCaMP3-expressing ΔG rabies virus

(A) Retinotopic organization of the striate and extrastriate cortical regions. The retinotopic map from intrinsic imaging was overlaid on the image of surface blood vessels. Location of the border between V1 and AL was identified based on the representation of the vertical meridien (nasalmost visual fields) to allow targetting of viral injections to AL (red X). SADΔG-GCaMP3-DsRedX was injected into the lateral extrastriate cortical area AL of the mice and the corresponding retinotopic location in V1 was noted as the expected location of retrogradely infected neurons (red square). (B) Z-stack of SADΔG-GCaMP3-DsRedX-infected neurons visualized *in vivo* with two-photon imaging of V1, 9 days after rabies injection. AL-projecting V1 neuronal cell bodies and processes could seen in imaging planes extending from the cortical surface to a depth of 1.5 mm (C) Top view of two-photon laser-scanning images of SADΔG-GCaMP3-DsRedX-infected neurons at depth of 370 μm from the cortical surface. V1 neurons were retrogradely labeled with SADΔG-GCaMP3-DsRedX and co-expressed GCaMP3 (green) and DsRedX (red). Note that GCaMP3 could be seen in dendrites and axons, as well as cell bodies. Scale bar, 25 μm. (D) Orientation selectivity of SADΔG-GCaMP3-DsRedX-infected V1 neurons. Panels in D1-D4 correspond to neuronal cell bodies (D1-D2) or dendrites (D3-D4) labeled 1-4 in panel C. Orientation tuning curves are plotted as the mean change in fluorescence of the cell body (D1 and D2) or dendritic segments (D3 and D4) during the entire stimulus period, in response to square-wave gratings presented at various orientations in a random order. (E) Changes in fluorescence over time, in response to drifting gratings at the preferred orientation. Time 0 indicates the onset of the visual stimulus, which lasted for 4 seconds, as indicated by the black bar. Note that fluorescence was modulated at temporal frequencies that correspond to the temporal frequencies of the drifting gratings. These temporal modulations in phase with the visual stimuli can also be seen in supplemental movies. Values in D and E represent means ± S.E.M. of ΔF/F values across 5 repetitions of the visual stimulus.

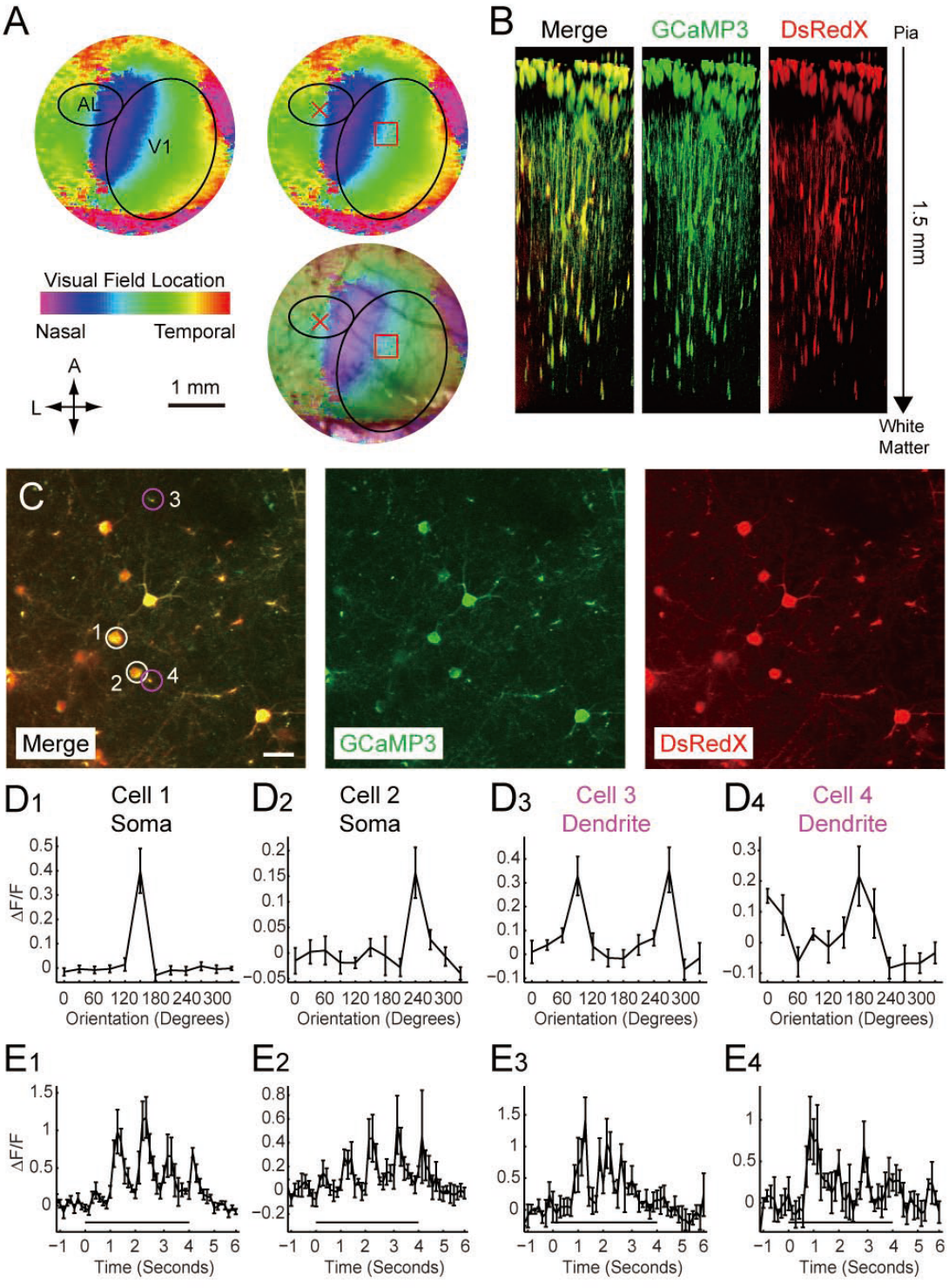
A
AL
V1
Visual Field Location
Nasal
Temporal
A
L
1 mm
B
Merge
GCaMP3
DsRedX
Pia
1.5 mm
White Matter
C
1
2
3
4
Merge
GCaMP3
DsRedX
D1
Cell 1 Soma
D2
Cell 2 Soma
D3
Cell 3 Dendrite
D4
Cell 4 Dendrite
ΔF/F
Orientation (Degrees)
E1
E2
E3
E4
Time (Seconds)

Methods

Two-photon imaging in SADΔG-GCaMP3- or SADΔG-GCaMP3-DsRedX-injected mice

C57BL/6J mice (5-10 weeks) were anesthetized with 1.0-1.5% isoflurane. An incision was made and the skin retracted over the stereotaxic location of V1 or V2. A metal frame was attached to the skull and the retinotopic organization of visual cortex was measured with intrinsic signal imaging through the intact skull using continuous stimulus presentation and data acquisition (Kalatsky and Stryker, 2003). Retinotopic maps from intrinsic imaging were overlaid on images of cortical surface vasculature, which allowed indentified cortical areas to be targeted for virus injection and two-photon calcium imaging. A small craniotomy was made and SADΔG-GCaMP3 was injected into the V1 of the mice at a 45 degree angle and a depth of 0.5 mm. SADΔG-GCaMP3-DsRedX was injected into the lateral extrastriate cortex (area AL; (Wang and Burkhalter, 2007)) of the mice according to the retinotopic organization, at an angle perpendicular to the brain surface, to a depth of ~0.4 mm. Nine-eleven days after virus injection, mice were again anesthetized with isoflurane, a craniotomy was made over visual cortex, covered with 1.5% agarose and a cover glass, and then sealed with Kwik-Cast. Chlorprothixene (0.5-1 mg/kg, i.m.) was administered and isoflurane was lowered to ~0.3-0.5% for visual stimulation. For visual stimulation to SADΔG-GCaMP3-injected mice, a visual stimulus consisting of drifting square-wave gratings at 8 directions in 45 degree steps (Psychtoolbox) was presented on a computer screen (100 Hz, calibrated 16” CRT) placed 10-15 cm from the animal, with 5 presentations

of each grating direction in random order and a blank condition in random order. For visual stimulation to SADΔG-GCaMP3-DsRedX-injected mice, a visual stimulus consisting of drifting square-wave gratings at 12 directions in 30 degree steps was presented on a computer screen (60 Hz, calibrated 55" LCD) placed 10-15 cm from the animal, with 5 presentations of each grating direction and a blank condition in random order. The spatial frequency of the grating was 0.04 cycles per degree (cpd) and the temporal frequency was 1 Hz. Two-photon imaging was performed using a custom-built version of the movable objective microscope (Sutter) based on a Ultrafast Ti:sapphire mode-locked laser (Chameleon Ultra, Coherent) and a laser-scanning system coupled to an upright microscope. Images were acquired using ScanImage (Pologruto et al., 2003). Time-lapse videos were processed in Matlab and ImageJ. Orientation tuning curves were generated by taking the mean response for each orientation during the entire stimulus period. Response amplitudes are presented as the relative change in fluorescence during the stimulus period compared to the prestimulus baseline (ΔF/F).

Supplementary Material

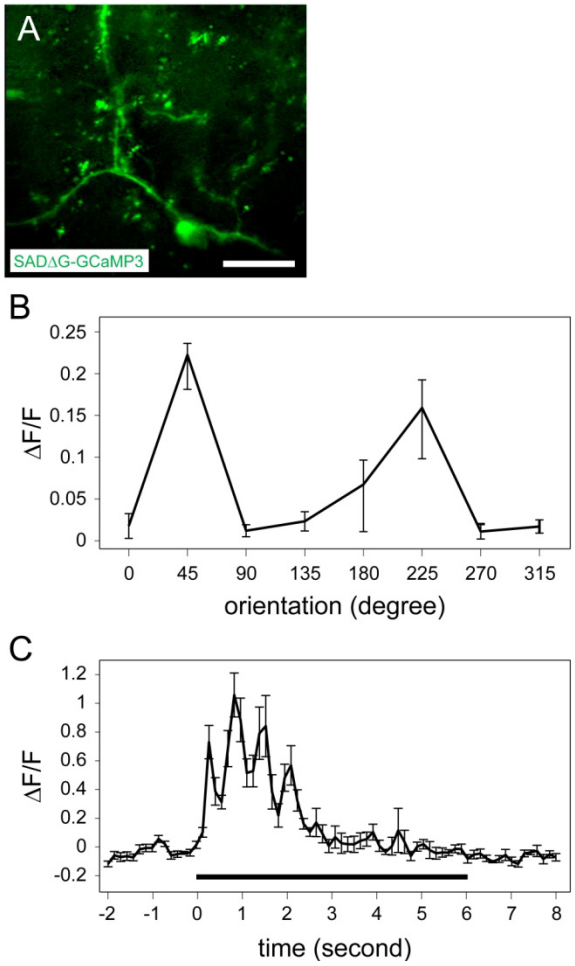

Figure AS.1 | Monitoring of neural activity with GCaMP3-expressing ΔG rabies virus

(A) Morphology of a mouse V1 cortex neuron infected by nearby injection of SADΔG-GCaMP3. The illustration is a Z-stack of two-photon images taken at multiple depths. Fluorescent GCaMP3 can be seen through the neuron's cell body, dendrites, and dendritic spines. Scale bar, 30 μm. (B) Orientation selectivity in SADΔG-GCaMP3 rabies-infected neuron. The orientation tuning curve is plotted as the mean change in fluorescence of the cell body during the entire stimulus period, in response to square-wave gratings (0.04 cpd) presented at various orientations, and directions, drifting at 1.67 Hz. (C) Changes in fluorescence over time, in response to drifting gratings at the preferred orientation of 45 degrees. Time 0 indicates the onset of the visual stimulus, which lasted for 6 seconds, as indicated by the black bar. Values in C and D represent means ± S.E.M. of ΔF/F values across 5 repetitions of the visual stimulus.

Figure AS.2 | Orientation selectivity in GCaMP3-DsRedX-expressing neurons in the V1.

(A, D) Two-photon laser-scanning images of SADΔG-GCaMP3-DsRedX-infected neurons at a depth of 520-535 μm 9 days after injection. SADΔG-GCaMP3-DsRedX was injected into the lateral extrastriate cortical area AL of the mice according to the retinotopic map. V1 neurons were retrogradely labeled with SADΔG-GCaMP3-DsRedX and coexpressed GCaMP3 (green) and DsRedX (red) in deep layers. Scale bar, 25 μm. (B, E) Examples of orientation selectivity recorded from 6 SADΔG-GCaMP3-DxRedX-infected V1 neurons labeled by number in A (B1-B3) and D (E1-E3), respectively. The orientation tuning curve is plotted as the mean change in the GCaMP3 fluorescence of the soma in response to each direction of the square-wave gratings. (C, F) Changes in fluorescence over time, reflecting visual responses to drifting gratings at the preferred direction of each neuron. Stimulus duration for 4 seconds is represented by the black bar under the curve. Time 0 indicates the onset of the visual stimulus. Values in B, C, D and E represent means ± S.E.M. of ΔF/F values across 5 repetitions of the visual stimulus. (G, J) SADΔG-GCaMP3-DsRedX-infected neurons in the V1 coexpressed GCaMP3 (green) and DsRedX (red) in the same mouse imaged again on day 11. Images are at the depth of 350 μm (G, J). Scale bars, 25 μm. (H, K) Examples of orientation selectivity in SADΔG-GCaMP3-DxRedX-infected V1 neurons illustrated in G and J. GCaMP3 signals were optically recorded from 3 different neurons in each field of view shown in G (H1-H3) and J (K1-K3). Changes in the fluorescence were observed at either the soma (H1, K1: Cell 1) or the dendrites (H2, K2: Cell 2 and H3, K3: Cell 3) in response to drifting gratings. (I, L) Temporal changes in GCaMP3 fluorescence in response to drifting gratings at the preferred direction. Note that orientation and direction selectivity were detected from GCaMP3-labeled dendrites and that infected neurons clearly showed robust visual responses and orientation selectivity even 11 days after injection.

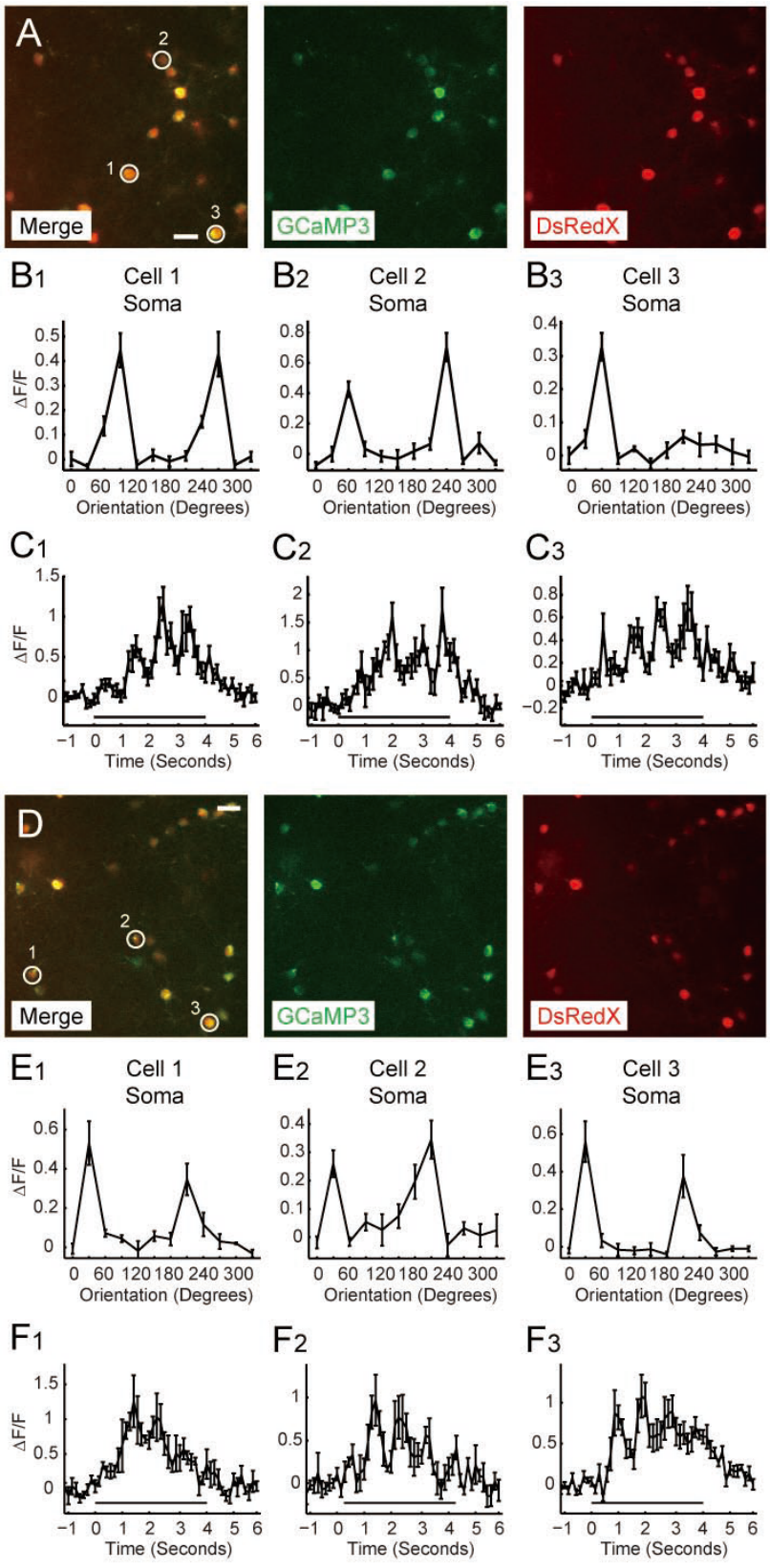
A
Merge
GCaMP3
DsRedX
B1 Cell 1 Soma
B2 Cell 2 Soma
B3 Cell 3 Soma
ΔF/F
Orientation (Degrees)
C1
C2
C3
Time (Seconds)
D
E1 Cell 1 Soma
E2 Cell 2 Soma
E3 Cell 3 Soma
F1
F2
F3

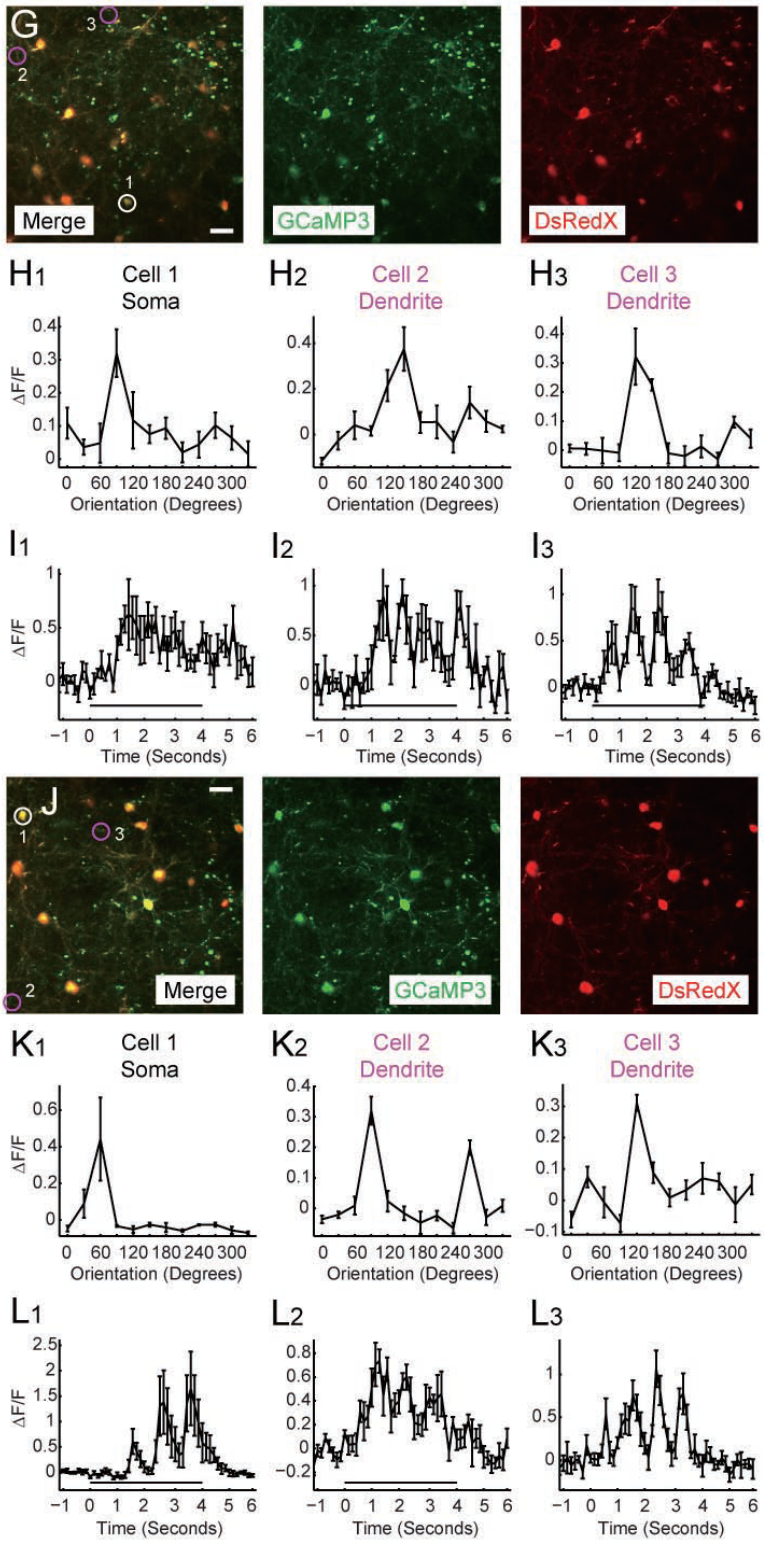

Figure AS.1: Orientation selectivity in GCaMP3-DsRedX-expressing neurons in the V1, Continued

Supplementary Movie A.1.

This movie illustrates changes in fluorescence of the same neuron for which data are illustrated in **Supplementary Figure A.1**. SADΔG-GCaMP3 was injected into the V1 of mice and two-photon imaging at an optical plane including the cell body was used to monitor fluorescence changes in response to visual stimuli. The 10 second duration of the movie corresponds to the same 10 second period illustrated in **Supplementary Figure A.1**. In response to a drifting grating at the preferred orientation of 45 degrees, there are several clear "flashes" at the position of the cell body in the center of the image, corresponding to the times when the preferred phase of the grating is optimally positioned within the cell's receptive field.

Supplementary Movie A.2.

This movie illustrates the Z-stack of images of SADΔG-GCaMP3-DsRedX-infected neurons in the V1, which correspond to **Figure A.1B**. Note that the SADΔG-GCaMP3-DsRedX-labeled apical dendrites are visible from the superficial cortical layers to the point where they meet with their cell bodies in deep layers, and that neurons are visible at the deepest imaging plane at a depth of 1.5 mm from the pial surface.

Supplementary Movie A.3.

This movie illustrates changes in the fluorescence of the SADΔG-GCaMP3-DsRedX-infected V1 neuron from **Figure A.1C1**. GCaMP3 signals in the soma were analyzed 9 days after injection. Increase in the GCaMP3 signal (ΔF/F) is the response to the preferred direction stimulus. There are several clear "flashes" at the position of the cell body in the center of the image, corresponding to the times when the preferred phase of the grating is optimally positioned within the cell's receptive field. The time course in the movie corresponds to **Figure A.1E1**.

Note: Supplementary movies are available for download online.

Acknowledgements

We thank I. Wickersham and J. Choi for helpful discussions, K. Roby, M. De La Parra, and K. von Bochmann for technical assistance, members of the Callaway laboratory for stimulating discussions, K. Conzelmann for the BSR T7/5 cell line, O. Britz and M. Goulding for the HeLa cells expressing frt-STOP-frt-nLacZ, I. Verma for HIV lentivirus packaging plasmids, X. Wu for the pNLST7, R. Tsien for the mCherry plasmid, K. Deisseroth for the ChR2-mCherry plasmid, L. Looger for the GCaMP3 plasmid, and C. Cepko for the pCAG-ER^{T2}CreER^{T2} and pCALNL-DsRed. F.O. is thankful to Noriko Osakada for constant encouragement and support. We are grateful for support from the National Institutes of Health (MH063912, NS069464, and EY010742: E.M.C.), the Kavli Institute for Brain and Mind at UC San Diego (E.M.C.), the Japan Society for the Promotion of Science (F.O.), the Kanae Foundation for the Promotion of Medical Science (F.O.), the Uehara Memorial Foundation (F.O.), and the Naito Foundation (F.O.).

Publication Acknowledgements

The Appendix, in part, is a reprint of the material as it appears in Neuron, 2011, Osakada, Fumitaka; Mori, Takuma; Cetin, Ali H.; Marshel, James H.; Virgen, Beatriz; Callaway, Edward M., Cell Press, 2011 (in press). The dissertation author is the co-investigator and co-author of this material.

References

Kalatsky, V. A., and Stryker, M. P. (2003). New paradigm for optical imaging: temporally encoded maps of intrinsic signal. Neuron *38*, 529-545.

Kerlin, A. M., Andermann, M. L., Berezovskii, V. K., and Reid, R. C. (2010). Broadly tuned response properties of diverse inhibitory neuron subtypes in mouse visual cortex. Neuron *67*, 858-871.

Kerr, J. N. D., Greenberg, D., and Helmchen, F. (2005). Imaging input and output of neocortical networks in vivo. Proc. Natl. Acad. Sci. U.S.A *102*, 14063-14068.

Luo, L., Callaway, E. M., and Svoboda, K. (2008). Genetic dissection of neural circuits. Neuron *57*, 634-660.

Miyawaki, A. (2005). Innovations in the imaging of brain functions using fluorescent proteins. Neuron *48*, 189-199.

Ohki, K., Chung, S., Ch'ng, Y. H., Kara, P., and Reid, R. C. (2005). Functional imaging with cellular resolution reveals precise micro-architecture in visual cortex. Nature *433*, 597-603.

Pologruto, T. A., Sabatini, B. L., and Svoboda, K. (2003). ScanImage: flexible software for operating laser scanning microscopes. Biomed Eng Online *2*, 13.

Runyan, C. A., Schummers, J., Van Wart, A., Kuhlman, S. J., Wilson, N. R., Huang, Z. J., and Sur, M. (2010). Response features of parvalbumin-expressing interneurons suggest precise roles for subtypes of inhibition in visual cortex. Neuron *67*, 847-857.

Tian, L., Hires, S. A., Mao, T., Huber, D., Chiappe, M. E., Chalasani, S. H., Petreanu, L., Akerboom, J., McKinney, S. A., Schreiter, E. R., et al. (2009). Imaging neural activity in worms, flies and mice with improved GCaMP calcium indicators. Nat. Methods *6*, 875-881.

Wang, Q., and Burkhalter, A. (2007). Area map of mouse visual cortex. J. Comp. Neurol *502*, 339-357.